
IJOER
ENGINEERING JOURNAL
Engineering Journal IJOER
VOLUME-12, ISSUE-5
MAY 2025
DOWNLOAD NOW
Contact us
+91-7665235235
www.ijoear.com
info@ijoear.com

Preface

We would like to present, with great pleasure, the volume-12, Issue-5, May 2026, of a scholarly journal, *International Journal of Engineering Research & Science*. This journal is part of the AD Publications series *in the field of Engineering, Mathematics, Physics, Chemistry and science Research Development*, and is devoted to the gamut of Engineering and Science issues, from theoretical aspects to application-dependent studies and the validation of emerging technologies.

This journal was envisioned and founded to represent the growing needs of Engineering and Science as an emerging and increasingly vital field, now widely recognized as an integral part of scientific and technical investigations. Its mission is to become a voice of the Engineering and Science community, addressing researchers and practitioners in below areas:

Chemical Engineering	
Biomolecular Engineering	Materials Engineering
Molecular Engineering	Process Engineering
Corrosion Engineering	
Civil Engineering	
Environmental Engineering	Geotechnical Engineering
Structural Engineering	Mining Engineering
Transport Engineering	Water resources Engineering
Electrical Engineering	
Power System Engineering	Optical Engineering
Mechanical Engineering	
Acoustical Engineering	Manufacturing Engineering
Optomechanical Engineering	Thermal Engineering
Power plant Engineering	Energy Engineering
Sports Engineering	Vehicle Engineering
Software Engineering	
Computer-aided Engineering	Cryptographic Engineering
Teletraffic Engineering	Web Engineering
System Engineering	
Mathematics	
Arithmetic	Algebra
Number theory	Field theory and polynomials
Analysis	Combinatorics
Geometry and topology	Topology
Probability and Statistics	Computational Science
Physical Science	Operational Research
Physics	
Nuclear and particle physics	Atomic, molecular, and optical physics
Condensed matter physics	Astrophysics
Applied Physics	Modern physics
Philosophy	Core theories

Chemistry	
Analytical chemistry	Biochemistry
Inorganic chemistry	Materials chemistry
Neurochemistry	Nuclear chemistry
Organic chemistry	Physical chemistry
Other Engineering Areas	
Aerospace Engineering	Agricultural Engineering
Applied Engineering	Biomedical Engineering
Biological Engineering	Building services Engineering
Energy Engineering	Railway Engineering
Industrial Engineering	Mechatronics Engineering
Management Engineering	Military Engineering
Petroleum Engineering	Nuclear Engineering
Textile Engineering	Nano Engineering
Algorithm and Computational Complexity	Artificial Intelligence
Electronics & Communication Engineering	Image Processing
Information Retrieval	Low Power VLSI Design
Neural Networks	Plastic Engineering

Each article in this issue provides an example of a concrete industrial application or a case study of the presented methodology to amplify the impact of the contribution. We are very thankful to everybody within that community who supported the idea of creating a new Research with IJOER. We are certain that this issue will be followed by many others, reporting new developments in the Engineering and Science field. This issue would not have been possible without the great support of the Reviewer, Editorial Board members and also with our Advisory Board Members, and we would like to express our sincere thanks to all of them. We would also like to express our gratitude to the editorial staff of AD Publications, who supported us at every stage of the project. It is our hope that this fine collection of articles will be a valuable resource for *IJOER* readers and will stimulate further research into the vibrant area of Engineering and Science Research.

Mukesh Arora

(Chief Editor)

Board Members

Dr. M. Varatha Vijayan

Annauniversity Rank Holder, Commissioned Officer Indian Navy, Ncc Navy Officer (Ex-Serviceman Navy), Best Researcher Awardee, Best Publication Awardee, Tamilnadu Best Innovation & Social Service Awardee From Lions Club.

Dr. Mohamed Abdel Fatah Ashabrawy Moustafa

PhD. in Computer Science - Faculty of Science - Suez Canal University University, 2010, Egypt.

Assistant Professor Computer Science, Prince Sattam bin AbdulAziz University ALkharj, KSA.

Prof.S.Balamurugan

Dr S. Balamurugan is the Head of Research and Development, Quants IS & CS, India. He has authored/co-authored 35 books, 200+ publications in various international journals and conferences and 6 patents to his credit. He was awarded with Three Post-Doctoral Degrees - Doctor of Science (D.Sc.) degree and Two Doctor of Letters (D.Litt) degrees for his significant contribution to research and development in Engineering.

Dr. Mahdi Hosseini

Dr. Mahdi did his Pre-University (12^{th}) in Mathematical Science. Later he received his Bachelor of Engineering with Distinction in Civil Engineering and later he Received both M.Tech. and Ph.D. Degree in Structural Engineering with Grade "A" First Class with Distinction.

Dr. Anil Lamba

Practice Head – Cyber Security, EXL Services Inc., New Jersey USA.

Dr. Anil Lamba is a researcher, an innovator, and an influencer with proven success in spearheading Strategic Information Security Initiatives and Large-scale IT Infrastructure projects across industry verticals. He has helped bring about a profound shift in cybersecurity defense. Throughout his career, he has parlayed his extensive background in security and a deep knowledge to help organizations build and implement strategic cybersecurity solutions. His published researches and conference papers has led to many thought provoking examples for augmenting better security.

Dr. Ali İhsan KAYA

Currently working as Associate Professor in Mehmet Akif Ersoy University, Turkey.

Research Area: Civil Engineering - Building Material - Insulation Materials Applications, Chemistry - Physical Chemistry – Composites.

Dr. Parsa Heydarpour

Ph.D. in Structural Engineering from George Washington University (Jan 2018), GPA=4.00.

Dr. Heba Mahmoud Mohamed Afify

Ph.D degree of philosophy in Biomedical Engineering, Cairo University, Egypt worked as Assistant Professor at MTI University.

Dr. Kalpesh Sunil Kamble (Ph.D., P.Eng., M.Tech, B.E. (Mechanical))

A distinguished academic with a Ph.D. in Mechanical Engineering and 13 Years of extensive teaching and research experience. He is currently a Assistant professor at the SSPM's COE, Kankavli and contributes to several undergraduate and masters programs across Mahrashtra, India.

Dr. Aurora Angela Pisano

Ph.D. in Civil Engineering, Currently Serving as Associate Professor of Solid and Structural Mechanics (scientific discipline area nationally denoted as ICAR/08"–"Scienza delle Costruzioni"), University Mediterranea of Reggio Calabria, Italy.

Dr. Faizullah Mahar

Associate Professor in Department of Electrical Engineering, Balochistan University Engineering & Technology Khuzdar. He is PhD (Electronic Engineering) from IQRA University, Defense View, Karachi, Pakistan.

Prof. Viviane Barrozo da Silva

Graduated in Physics from the Federal University of Paraná (1997), graduated in Electrical Engineering from the Federal University of Rio Grande do Sul - UFRGS (2008), and master's degree in Physics from the Federal University of Rio Grande do Sul (2001).

Dr. S. Kannadhasan

Ph.D (Smart Antennas), M.E (Communication Systems), M.B.A (Human Resources).

Dr. Christo Ananth

Ph.D. Co-operative Networks, M.E. Applied Electronics, B.E Electronics & Communication Engineering Working as Associate Professor, Lecturer and Faculty Advisor/ Department of Electronics & Communication Engineering in Francis Xavier Engineering College, Tirunelveli.

Dr. S.R.Boselin Prabhu

Ph.D, Wireless Sensor Networks, M.E. Network Engineering, Excellent Professional Achievement Award Winner from Society of Professional Engineers Biography Included in Marquis Who's Who in the World (Academic Year 2015 and 2016). Currently Serving as Assistant Professor in the department of ECE in SVS College of Engineering, Coimbatore.

Dr. Balasubramanyam, N

Dr.Balasubramanyam, N working as Faculty in the Department of Mechanical Engineering at S.V.University College of Engineering Tirupati, Andhra Pradesh.

Dr. PAUL P MATHAI

Dr. Paul P Mathai received his Bachelor's degree in Computer Science and Engineering from University of Madras, India. Then he obtained his Master's degree in Computer and Information Technology from Manonmanium Sundaranar University, India. In 2018, he received his Doctor of Philosophy in Computer Science and Engineering from Noorul Islam Centre for Higher Education, Kanyakumari, India.

Dr. M. Ramesh Kumar

Ph.D (Computer Science and Engineering), M.E (Computer Science and Engineering).

Currently working as Associate Professor in VSB College of Engineering Technical Campus, Coimbatore.

Dr. Maheshwar Shrestha

Postdoctoral Research Fellow in DEPT. OF ELE ENGG & COMP SCI, SDSU, Brookings, SD Ph.D, M.Sc. in Electrical Engineering from SOUTH DAKOTA STATE UNIVERSITY, Brookings, SD.

Dr. D. Amaranatha Reddy

Ph.D. (Postdocteral Fellow, Pusan National University, South Korea), M.Sc., B.Sc. : Physics.

Dr. Dibya Prakash Rai

Post Doctoral Fellow (PDF), M.Sc., B.Sc., Working as Assistant Professor in Department of Physics in Pachhuncga University College, Mizoram, India.

Dr. Pankaj Kumar Pal

Ph.D R/S, ECE Deptt., IIT-Roorkee.

Dr. P. Thangam

PhD in Information & Communication Engineering, ME (CSE), BE (Computer Hardware & Software), currently serving as Associate Professor in the Department of Computer Science and Engineering of Coimbatore Institute of Engineering and Technology.

Dr. Pradeep K. Sharma

PhD., M.Phil, M.Sc, B.Sc, in Physics, MBA in System Management, Presently working as Provost and Associate Professor & Head of Department for Physics in University of Engineering & Management, Jaipur.

Dr. R. Devi Priya

Ph.D (CSE), Anna University Chennai in 2013, M.E, B.E (CSE) from Kongu Engineering College, currently working in the Department of Computer Science and Engineering in Kongu Engineering College, Tamil Nadu, India.

Dr. Sandeep

Post-doctoral fellow, Principal Investigator, Young Scientist Scheme Project (DST-SERB), Department of Physics, Mizoram University, Aizawl Mizoram, India- 796001.

Dr. Roberto Volpe

Faculty of Engineering and Architecture, Università degli Studi di Enna "Kore", Cittadella Universitaria, 94100 – Enna (IT).

Dr. S. Kannadhasan

Ph.D (Smart Antennas), M.E (Communication Systems), M.B.A (Human Resources).

Research Area: Engineering Physics, Electromagnetic Field Theory, Electronic Material and Processes, Wireless Communications.

Mr. Bhavinbhai G. Lakhani

An expert in Environmental Technology and Sustainability, with an M.S. from NYIT. Their specialization includes Construction Project Management and Green Building. Currently a Project Controls Specialist Lead at DACK Consulting Solutions, they manage project schedules, resolve delays, and handle claim negotiations. Prior roles as Senior Project Manager at FCS Group and Senior Project Engineer at KUNJ Construction Corp highlight their extensive experience in project estimation, resource management, and on-site supervision.

Mr. Omar Muhammed Neda

Department of Electrical Power Engineering, Sunni Diwan Endowment, Iraq.

Mr. Amit Kumar

Amit Kumar is associated as a Researcher with the Department of Computer Science, College of Information Science and Technology, Nanjing Forestry University, Nanjing, China since 2009. He is working as a State Representative (HP), Spoken Tutorial Project, IIT Bombay promoting and integrating ICT in Literacy through Free and Open Source Software under National Mission on Education through ICT (NMEICT) of MHRD, Govt. of India; in the state of Himachal Pradesh, India.

Mr. Tanvir Singh

Tanvir Singh is acting as Outreach Officer (Punjab and J&K) for MHRD Govt. of India Project: Spoken Tutorial - IIT Bombay fostering IT Literacy through Open Source Technology under National Mission on Education through ICT (NMEICT). He is also acting as Research Associate since 2010 with Nanjing Forestry University, Nanjing, Jiangsu, China in the field of Social and Environmental Sustainability.

Mr. Abilash

MTech in VLSI, BTech in Electronics & Telecommunication engineering through A.M.I.E.T.E from Central Electronics Engineering Research Institute (C.E.E.R.I) Pilani, Industrial Electronics from ATI-EPI Hyderabad, IEEE course in Mechatronics, CSHAM from Birla Institute Of Professional Studies.

Mr. Varun Shukla

M.Tech in ECE from RGPV (Awarded with silver Medal By President of India), Assistant Professor, Dept. of ECE, PSIT, Kanpur.

Mr. Shrikant Harle

Presently working as a Assistant Professor in Civil Engineering field of Prof. Ram Meghe College of Engineering and Management, Amravati. He was Senior Design Engineer (Larsen & Toubro Limited, India).

Mr. Zairi Ismael Rizman

Senior Lecturer, Faculty of Electrical Engineering, Universiti Teknologi MARA (UiTM) (Terengganu) Malaysia Master (Science) in Microelectronics (2005), Universiti Kebangsaan Malaysia (UKM), Malaysia. Bachelor (Hons.) and Diploma in Electrical Engineering (Communication) (2002), UiTM Shah Alam, Malaysia.

Mr. Ronak

Qualification: M.Tech. in Mechanical Engineering (CAD/CAM), B.E.

Presently working as a Assistant Professor in Mechanical Engineering in ITM Vocational University, Vadodara. Mr. Ronak also worked as Design Engineer at Finstern Engineering Private Limited, Makarpura, Vadodara.

Table of Contents

Volume-12, Issue-5, May 2026

International Journal of Engineering Research & Science (IJOER)
ISSN: [2395-6992]
[Vol-12, Issue-5, May- 2026]
Website: www.ijoer.com
Journal DOI: 10.25125/engineering-journal

Analysis of the Evolution and Influencing Factors of the Global Zirconium Ore Trade Pattern Based on Complex Networks

Li Kang

Guizhou University of Finance and Economics, Department of Big Data Statistics, Guiyang
*Corresponding Author

Received: 01 May 2026/ Revised: 08 May 2026/ Accepted: 13 May 2026/ Published: 31-05-2026

Abstract— *This paper examines the evolution of the global zirconium ore trade network using a matrix of bilateral trade relationships from 2014 to 2023, selecting 2014, 2017, 2020, and 2023 as cross-sectional years. Focusing on the countries that account for the top 80% of the global zirconium ore trade volume, this study employs the Quadratic Assignment Procedure (QAP) to systematically analyze the key factors driving trade volumes and their temporal evolution across four dimensions: economic scale, factor endowments, geographical distance, and institutional quality. The study yields four main findings: (1) Overall, the network exhibits the characteristic of "expanding in scale but becoming increasingly sparse." While the number of participating countries has increased, network density and centrality have declined, and the network's small-world properties have weakened under the influence of external shocks. (2) Trade flows are highly concentrated with a shifting center of gravity. China has emerged as a major transshipment hub with strong resource allocation capabilities, acting as the primary core of the network, while emerging hubs exemplified by the Netherlands have concurrently risen. (3) The community structure has evolved toward multipolarity and regionalization. It has gradually restructured from an early tripolar structure centered around China, Italy, and South Africa into a more decentralized multipolar configuration anchored by China, Spain, and South Africa, accompanied by frequent shifts in regional sub-centers. (4) The trade-driving mechanisms are characterized by a combination of economic complementarity and resource endowment orientation. QAP regression analysis reveals that differences in per capita GDP and urbanization levels are the primary positive drivers of bilateral trade. Furthermore, the zirconium ore trade has transcended the geographical distance and linguistic-cultural barriers typical of traditional gravity models, demonstrating the hallmark features of cross-regional, long-distance allocation. Conversely, disparities in government effectiveness and significant differences in economic size constitute barriers to trade.*

Keywords— global zirconium ore trade; complex networks; international trade networks; QAP analysis; influencing factors.

I. INTRODUCTION

The world today is at a critical juncture in a new round of technological revolution and industrial transformation. The deepening process of industrialization and the rapid evolution of high-tech innovations have significantly reshaped the global demand landscape for mineral resources[1]. However, due to limitations imposed by geological and mineralization conditions, the global distribution of certain critical metal resources is highly uneven. This is particularly true for critical metal resources such as zirconium, whose strategic importance is increasingly evident as the material foundation underpinning the development of strategic emerging industries[2]. As a prime example of a resource constrained by geographical distribution yet possessing core strategic value for global future development, zirconium plays an important role in the global industrial chain[3].

As a rare metal, zirconium possesses a unique combination of physical and chemical properties, including an extremely low thermal neutron absorption cross-section, exceptional corrosion resistance, and an ultra-high melting point. It plays a critical supporting role in core sectors critical to national security and energy transition, such as the nuclear industry, aerospace, advanced chemical equipment, and the microalloying process of high-performance specialty metal materials[4]. Driven by the rapid growth of global low-carbon technologies, smart equipment, and high-end alloy industries, the strategic scarcity of

zirconium resources has become increasingly apparent, prompting many countries to step up efforts to secure their supply chains[5-8]. In response to this massive demand, China has formulated comprehensive policies and officially designated zirconium as a strategic mineral to stabilize domestic supply[9]. Meanwhile, developed countries such as the United States and Japan have successively included zirconium on their strategic lists of rare metals or critical minerals, and are accelerating efforts to diversify import sources and build national reserves[10-12]. As global industrial transformation deepens, the strategic importance of zirconium is expected to become even more pronounced[13]. Overall, given its high technological barriers and wide-ranging industrial applications, zirconium ore resources have become an important material basis for strategic emerging industries and national core competitiveness.

However, in previous research on rare metal ores, most scholars have primarily focused on lithium[14-15], cobalt[16-17], tungsten[18-19], nickel[20-21], and rare earth elements[22-23], with relatively little research dedicated to zirconium. In recent years, with the rapid development of network analysis techniques, complex network analysis has become a common method used by scholars both domestically and internationally to study hot topics such as global minerals[24], food[25], oil[26], military affairs[27], natural gas[28], and seafood[29]. Research has primarily focused on the evolution of network characteristics, influencing factors, risk propagation, trade status, and robustness analysis. Regarding research on the global trade network of zirconium ore, only scholar Fanjie Luo[30] has conducted preliminary explorations to date.

In recent years, a series of external shocks—including Australian export controls, the COVID-19 pandemic, and the Ukraine crisis—have occurred in rapid succession. Against this complex backdrop, what new characteristics does the spatial evolution of the global zirconium ore trade network exhibit? Which countries play a key role within the network? How can insights for ensuring resource security be derived from network evolution? These questions await further exploration. In light of this, this paper draws on trade data from the UN Comtrade database for 2014–2023 to conduct an in-depth investigation into the spatial structural evolution of the global zirconium ore trade network and its underlying mechanisms. Compared to previous studies, this paper's marginal contributions lie in two aspects: first, it expands the temporal scope of the research, using the latest reliable data to accurately capture the current topological structure of the zirconium ore trade network in the post-pandemic era and against the backdrop of geopolitical tensions; second, it deepens the analysis of influencing mechanisms, providing empirical support for a profound understanding of the driving forces behind structural changes in the global zirconium resource trade network. This has important practical implications for effectively responding to fluctuations in the international market and formulating targeted resource security policies.

II. MATERIAL AND METHODS

2.1 Data

This study focuses on zirconium ore and its concentrates (HS Code: 261510)—a core commodity in the zirconium industry chain and supply chain—using data from the United Nations Commodity Trade Statistics Database (UN Comtrade). Because UN Comtrade data suffers from a certain degree of lag, this study constructed a full-sample dataset of global zirconium ore trade from 2014 to 2023. During the data cleaning process, common issues with the UN Comtrade database were addressed: (1) Outliers were removed to prevent them from influencing the data analysis; (2) Records where the importing and exporting countries (regions) were the same were deleted; (3) Aggregated regional data were excluded, as they do not represent sovereign states or regions belonging to a single sovereign state. Given that import-side regulations are stricter and data quality is often higher in international trade statistics, this study prioritizes import data as the analytical benchmark. To address missing trade volume data in some samples, estimates were back-calculated using the global average annual price of zirconium ore for that year. Additionally, to ensure data robustness, identified outliers were smoothed by substituting them with the average trade volume from the preceding and following years for that country.

2.2 Network Architecture and Topology Metrics

Based on complex network theory, this study abstracts the global zirconium ore trade system into a temporal directed weighted network model $G_t = (V_t, E_t, W_t)$. In this model, t represents the year, with a fixed time period t, the node set $V_t = \{v_{t1}, v_{t2}, v_{t3}, \cdots, v_{tN}\}$ represents the various countries or regions participating in international zirconium ore trade; the edge set $E_t = \{e_{ij}, i, j \in V_t\}$ depicts the direction of trade flows between countries; if country i exports zirconium ore to country j, a directed edge e_{ij} is established; The weight set $W_t = \{w_{ij}, i, j \in V_t\}$ quantifies the trade volume of bilateral trade. To explore the topological structure and evolutionary patterns of the global zirconium ore trade network from multiple dimensions,

this paper constructs a multidimensional indicator system that encompasses both macro-level network morphology and micro-level node status. At the macro-network level, this study selects network density and average degree to quantify the overall tightness and activity level of trade links among countries; average path length and average clustering coefficient are introduced to assess the network's transmission efficiency and local clustering characteristics, thereby determining whether the network exhibits "small-world" properties; simultaneously, the modularity index is utilized to identify community structures within the trade network, revealing the regionalization and clustering trends in global trade. At the micro-node level, this study employs three centrality measures to characterize the role of each country: degree centrality intuitively reflects a country's direct influence and hub status within the trade network; betweenness centrality identifies key "bridges" and intermediary countries that control resource flow paths; and closeness centrality measures the shortest distance between a node and all other nodes, thereby assessing a country's ease of access to trade resources and its independence within the network.

TABLE 1
MEASURES AND DEFINITIONS OF THE ZIRCONIUM ORE TRADE NETWORK

Indicators	Formula	Meaning
Out–degree	$k_i^{out} = \sum_{j=1}^{N} e_{ij}$	Out-degree represents the number of connections a country or region has in a trade network that lead to other countries or regions.
In-degree	$k_i^{in} = \sum_{j=1}^{N} e_{ji}$	In-degree represents the number of connections a country or region has in a trade network that lead from other countries or regions.
Degree	$k_i = k_i^{in} + k_i^{out}$	A higher total degree indicates that the country has more trading partners and is more active in trade.
Betweenness Centrality	$BC(i) = \sum_{s \neq t \neq i} \frac{\sigma_{si}(i)}{\sigma_{st}}$	The Betweenness Centrality of a country or region reflects its importance in the trade routes connecting other countries or regions.
Closeness Centrality	$C_C(i) = \frac{N-1}{\sum_{t=1}^{N} d(i,t)}$	Measures a country's efficiency and ease in accessing trade resources. A higher centrality score indicates that the country is more independent within the network and can access and obtain the necessary trade resources more quickly.
Network Density	$D = \frac{m}{N(N-1)}$	It is used to reflect the strength of trade relationships between nodes (countries or regions) within the network.
Average Degree	$\bar{k} = \frac{1}{N}\sum_{i=1}^{N} k_i$	This indicator measures the overall average level of activity within the network, specifically the extent to which each country, on average, establishes trade relationships within the trade network.
Average Path Length	$L = \frac{1}{N(N-1)}\sum_{i \neq j} d_{ij}$	It is used to measure the overall connectivity and efficiency of a trade network, reflecting the average efficiency with which information or goods flow through the network.
Average Clustering Coefficient	$C_i = \frac{2E_i}{k_i(k_i-1)}$	This indicator reflects a country's propensity to trade with its existing trading partners.
Modularity	$Q = \frac{1}{2m}\sum_{ij}\left[W_{ij} - \frac{k_i k_j}{2m}\right]$	Modularity is a measure of the degree of fragmentation among small groups within a transaction network.

III. EVOLUTIONARY CHARACTERISTICS OF THE GLOBAL ZIRCONIUM ORE TRADE NETWORK STRUCTURE

3.1 Comprehensive Network Visualization

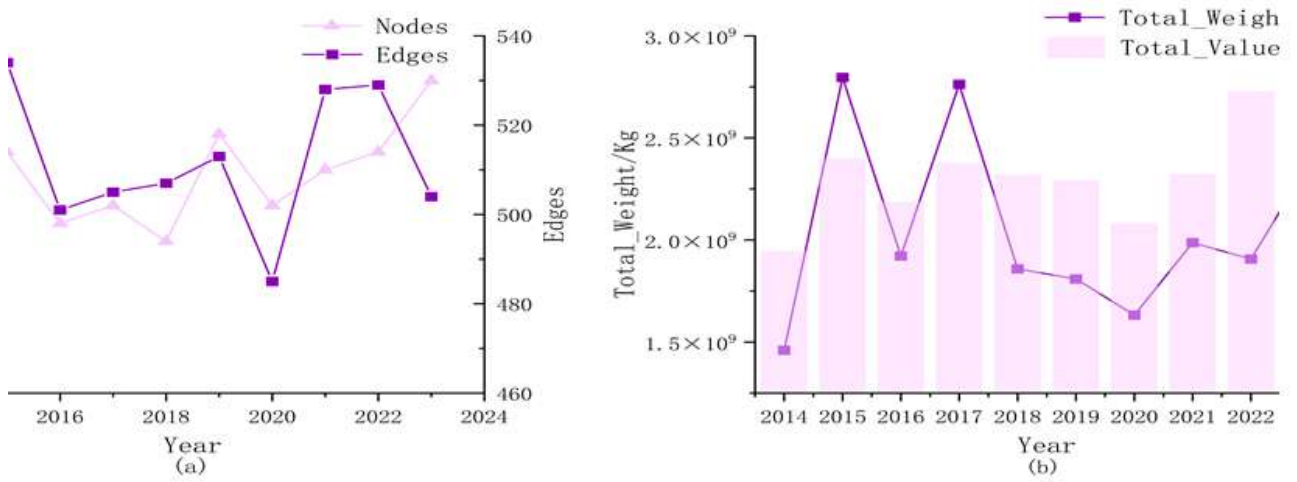

FIGURE 1: Trend Chart Showing the Evolution of the Global Zirconium Ore Trade Network

This paper presents a visual analysis of the trade-weighted network of global zirconium ore trade from 2014 to 2023 (Figures 1 and 2). Figure 1 employs a dual-axis format to comprehensively illustrate the scale of global zirconium ore trade during this period, focusing on trade value, trade flows, the number of nodes, and the number of edges. Figure 1(a) illustrates the evolution of the number of nodes (number of participating countries or regions) and the number of edges (number of trade relationships) in the global trade network for zirconium-related products from 2014 to 2023. Overall, the number of participants in this trade network fluctuated between 91 and 105, demonstrating strong network resilience and stability. Specifically, after expanding in 2015, the number of nodes entered a period of stability and reached a peak of 105 in 2023—the highest value observed during the study period—indicating that an increasing number of countries and regions have joined the global zirconium ore supply chain. Meanwhile, the number of edges, which represents network connectivity, exhibited a fluctuating trend. After peaking at 534 in 2015, the number of edges dropped to a low of 485 in 2020 due to external shocks such as the global macroeconomic environment and trade frictions. Subsequently, as global supply chains recovered, it gradually rebounded to 504 in 2023. This reflects that although the global trade network experienced localized contraction during exceptional periods, overall trade linkages have maintained strong resilience. Figure 1(b) illustrates the changes in total trade flows and total trade value within this network over the past decade. Historically, trade volume and trade value maintained a high degree of consistency prior to 2020, exhibiting distinct cyclical fluctuations. In 2015 and 2017, total physical trade volume experienced two significant surges, driving trade value to correspondingly high levels. These spikes typically corresponded to concentrated releases of demand from related downstream industries globally or concentrated output from major exporting countries. However, between 2018 and 2020, both physical trade volume and trade value declined, reaching recent local lows in 2020, clearly illustrating the suppressing effect of the external environment on global commodity trade flows. At the same time, it is worth noting that starting in 2021, a clear divergence emerged between total trade value and total trade volume. This was particularly evident in 2022, when, although total trade volume did not return to historical highs, total trade value experienced substantial growth contrary to general trends, reaching a ten-year peak; in 2023, while the value declined slightly, it remained at a high level. This pronounced “divergence between volume and value” clearly reveals a significant increase in the unit value of zirconium products in the international market over the past two years. This rapid price surge may stem from tightening supply of upstream raw materials, premiums resulting from supply chain restructuring driven by geopolitical uncertainties or increased relatively stable demand for this material from emerging high-tech industries. Consequently, without a significant expansion in physical scale, the overall value of global trade has been substantially boosted.

Figure 2 uses a chord diagram to visually illustrate the evolution of core trade relationships—those accounting for 80% of the total trade volume—within the global zirconium ore trade network over the decade from 2014 to 2023. In the figure, the length of the arcs represents the total trade volume of each country, while the width of the connecting lines corresponds to the specific bilateral trade flows. The figure clearly shows that between 2014 and 2023, the number of countries and regions involved in the top 80% of core trade relationships declined slightly, from 42 in 2014 to 37 in 2023. At the same time, global zirconium

ore trade exhibited a core structure anchored by three nodes: China, Australia, and South Africa. These three countries have consistently held the top three positions in terms of trade share within the global zirconium ore trade network, clearly illustrating the unidirectional flow of zirconium ore resources from major supplier countries (Australia and South Africa) to core processing countries (China), as well as the high concentration of trade power. Although the core structure remains stable, non-core regions show a dynamic trend toward supply chain diversification. For example, the emergence of emerging resource-rich countries such as Brazil in the 2023 chart indicates that global supply sources are gradually expanding from traditional regions to areas like South America. Some peripheral countries are beginning to join the core trade circle, reflecting how the global trade network is constantly undergoing peripheral restructuring and change while maintaining the stability of its backbone.

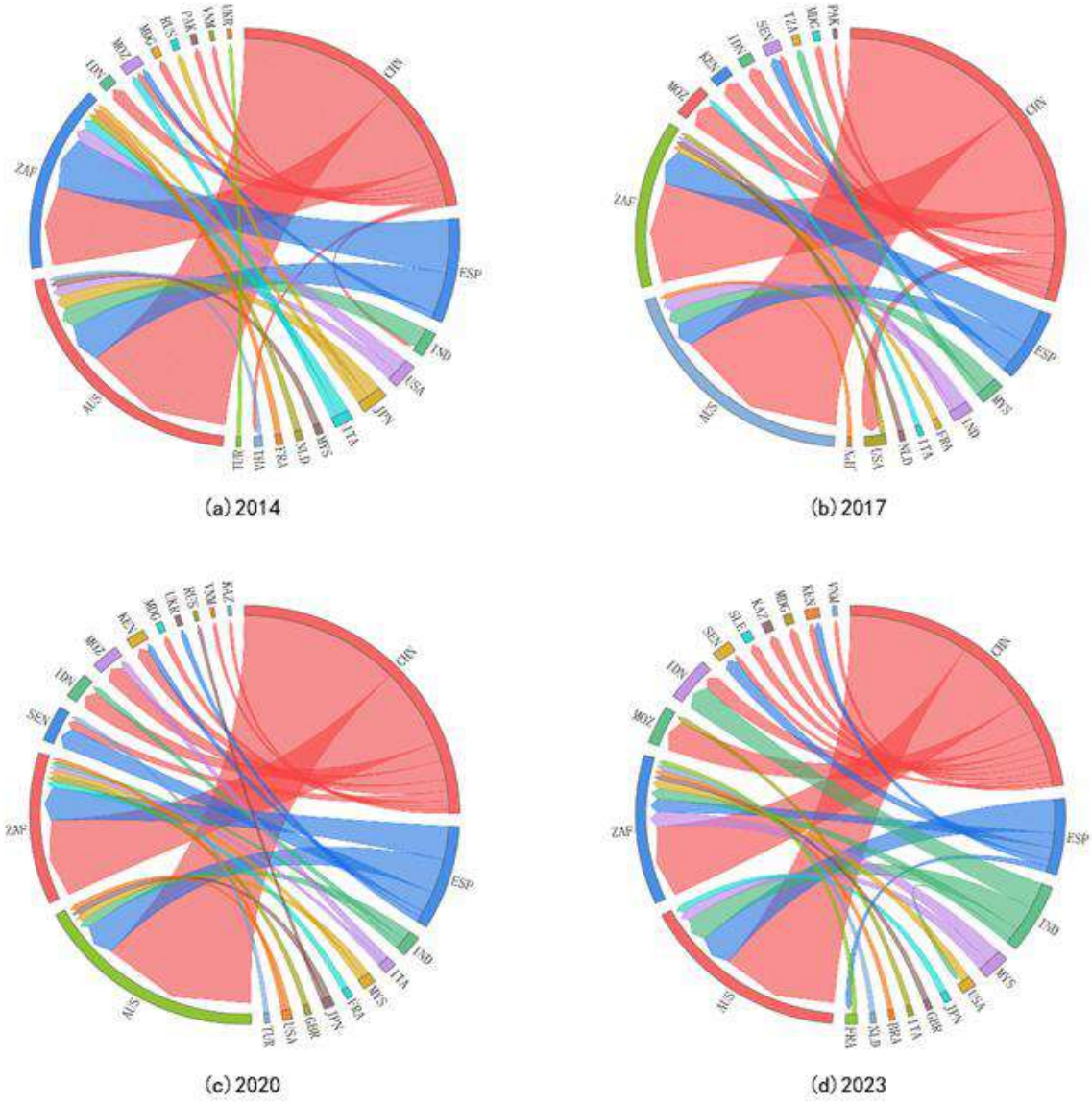

FIGURE 2: Chord diagram of the top 80% of core relationships in the global zirconium ore trade network (2014-2023)

3.2 General Characteristics of Network Evolution

In terms of network density (Table 2), the data reveals a structural characteristic of "expanding scale but sparse connectivity." Network density declined steadily from 0.057 in 2014 to 0.046 in 2023, while the average degree also fell from 10.308 to 9.600. This may be attributed to the pandemic, which led to a reduction in the number of countries and regions participating in trade, a weakening of trade ties, and the fact that most newly added trading partners are located on the periphery of the network. These countries typically establish single connections with only a few core nations and have not fully integrated into the multilateral trading system. This pattern has caused the overall connectivity density of the network to decrease despite its

expansion in scale, as newly integrated peripheral nodes contribute few additional edges relative to the growing node count, resulting in increasingly loose trade relationships.

TABLE 2
EVOLUTIONARY INDICATORS OF THE TOPOLOGICAL STRUCTURE OF THE GLOBAL ZIRCONIUM ORE TRADE NETWORK (2014–2023)

Statistical characteristics	Statistical indicators	Year			
		2014	2017	2020	2023
Network size	Average Degree	10.308	10.306	9.898	9.600
	Network Density	0.057	0.053	0.051	0.046
Small-World Property	Average Clustering Coefficient	0.395	0.388	0.275	0.340
	Average Path Length	2.194	2.325	2.301	2.366

In terms of Small-World Property characteristics (Table 2), the network exhibits an evolutionary trend of "weakened clustering and lengthened paths." The average clustering coefficient dropped significantly from 0.388 in 2017 to 0.275 in 2020; although it rebounded to 0.340 in 2023, it has not yet returned to previous levels. This implies that the original localized trade tightly connected local groups or regional clusters suffered structural disruption under the impact of the pandemic, resulting in reduced connectivity among trading partners.

Meanwhile, the average path length increased slightly from 2.194 to 2.366, indicating a slight increase in the number of links in the global flow of resources, which has constrained overall transmission efficiency to some extent.

In terms of the "out-degree" indicator (Table 3), which reflects export reach and the breadth of supply networks, Spain consistently ranked first in 2014, 2017, and 2020, demonstrating its strong influence as a major global zirconium ore export hub over an extended period. However, this landscape underwent a significant shift in 2023, as China's out-degree value surged to 43, replacing Spain as the top-ranked country globally. This indicates a substantial strengthening of China's hub status in terms of the number of zirconium ore export partners and its overall supply network. Additionally, countries such as the United States, South Africa, Australia, and Germany frequently alternated within the top five out-degree rankings, collectively forming major global sources of zirconium ore exports.

Second, the "in-degree" indicator (Table 3), which reflects the degree of import diversification and the breadth of market demand, reveals a different picture. From 2014 to 2020, China consistently ranked first in in-degree, indicating that as a major manufacturing power and consumer of mineral resources, China had long been the most central buyer's market for global zirconium ore, possessing the broadest import channels. However, it is worth noting that by 2023, the Netherlands' import index surged to 37, propelling it to the top spot, while China dropped to second place. At the same time, European countries such as Italy, France, and Spain have consistently remained within the top five for the import index, while Asian nations like India and Malaysia have gradually moved into the leading ranks. This reflects that while demand for global zirconium ore remains highly active in Europe, it is gradually spreading to certain emerging economies in Asia.

TABLE 3
TOP FIVE COUNTRIES BY NETWORK CENTRALITY IN THE GLOBAL ZIRCONIUM ORE TRADE NETWORK (2014–2023)

Indicators	Rank	2014	2017	2020	2023
Out-degree	1	ESP（42）	ESP（42）	ESP（39）	CHN（43）
	2	DEU（33）	USA（36）	ZAF（33）	ESP（33）
	3	ITA（33）	DEU（35）	USA（33）	ZAF（31）
	4	AUS（32）	ZAF（34）	CHN（31）	USA（29）
	5	USA（32）	CHN（34）	ITA（29）	AUS（26）
In-degree	1	CHN（28）	CHN（31）	CHN（28）	NLD（37）
	2	ITA（21）	FRA（19）	NLD（22）	CHN（29）
	3	FRA（18）	ITA（17）	IND（20）	ESP（24）
	4	ESP（15）	MYS（17）	ITA（19）	IND（22）
	5	GBR（14）	NLD（17）	FRA（18）	ITA（21）
Degree	1	CHN（58）	CHN（65）	CHN（59）	CHN（72）
	2	ESP（57）	ESP（55）	ESP（53）	ESP（57）
	3	ITA（54）	USA（49）	ITA（48）	NLD（53）
	4	USA（43）	ITA（47）	USA（42）	IND（45）
	5	ZAF（37）	ZAF（41）	NLD（38）	USA（42）

Finally, the “Degree” indicator (Table 3), which comprehensively measures a country’s status as a central hub within the overall trade network, reveals that China maintained a highly stable central position in the global zirconium ore trade network. In 2014, 2017, 2020, and 2023, China consistently ranked first globally in total degree, reaching a peak of 72 in 2023, primarily due to a significant increase in its out-degree in recent years. Spain, meanwhile, demonstrated exceptional network stability, consistently ranking second in total degree across all four observation years. However, the bottom three positions in the total degree ranking have undergone significant changes: the traditional prominence of the United States and Italy has declined in recent years, while the Netherlands and India, driven by active import and export activities, surged to third and fourth place in the total degree ranking in 2023. Overall, the center of gravity in the global zirconium ore trade network is gradually shifting toward Asian countries anchored by China, as well as emerging trade hubs represented by the Netherlands, which serves as a gateway to Europe.

Intermediary Betweenness Centrality reflects a node’s ability to control the flow of resources. China ranked first across all four time periods (Table 4), with its value rising steadily from 0.132 in 2014 to 0.183 in 2023. This indicates that its status as a “major transshipment hub” for global zirconium ore trade is becoming increasingly solidified, giving it the strongest control and routing capability over global trade flows. The rise of the Netherlands is particularly notable, with its index jumping from 0.070 in 2017 to 0.161 in 2023 (ranking second), demonstrating a significant enhancement of its role as a European gateway and a major global transshipment hub. In contrast, the intermediary status of traditional European powers such as Italy and Spain remained relatively stable but showed slight fluctuations, indicating that the transshipment functions of global trade are becoming highly concentrated in a few core hubs (China and the Netherlands).

TABLE 4
EVOLUTION OF CENTRALITY METRICS FOR NODES IN THE GLOBAL ZIRCONIUM ORE TRADE NETWORK (2014–2023)

Indicators	Rank	2014	2017	2020	2023
Betweenness Centrality	1	CHN（0.132）	CHN（0.146）	CHN（0.141）	CHN（0.183）
	2	ITA（0.120）	NLD（0.070）	NLD（0.109）	NLD（0.161）
	3	ESP（0.097）	ITA（0.068）	ESP（0.081）	ESP（0.094）
	4	USA（0.050）	USA（0.059）	FRA（0.058）	ITA（0.064）
	5	FRA（0.049）	ESP（0.052）	USA（0.053）	FRA（0.053）
Closeness Centrality	1	ESP（0.588）	ESP（0.552）	ZAF（0.516）	CHN（0.492）
	2	DEU（0.562）	DEU（0.546）	ESP（0.512）	ZAF（0.463）
	3	AUS（0.539）	ZAF（0.529）	USA（0.501）	USA（0.453）
	4	USA（0.539）	CHN（0.525）	CHN（0.497）	AUS（0.440）
	5	ZAF（0.527）	USA（0.521）	DEU（0.477）	DEU（0.435）

Closeness Centrality measures the ease with which a node can access other trading partners and its degree of independence. From 2014 to 2017 (Table 4), Spain and Germany held the top two positions, reflecting the tight-knit and efficient nature of the intra-European trade network at that time. However, the landscape underwent a significant structural shift in the later period: South Africa took the top spot in 2020 (0.516), while China surged to first place in 2023 (0.492). This evolution reveals a substantial shift in the global center of gravity for zirconium ore trade—from traditional European consumer markets toward the source of resources (South Africa) and the core processing and consumption hub (China). In 2023, China topped both indicators, marking its evolution from a mere trading powerhouse into a primary core node within the network—one with the shortest pathways, highest transmission efficiency, and strongest control over resource flows.

3.3 Structural Characteristics of Trade Network Communities

Analysis using Gephi 0.10.1 revealed that the global zirconium ore trade network exhibits a significant trend toward evolution from a highly centralized structure to a multipolar, regionally dispersed one.

In 2014, the network displayed high cohesion, consisting of only three major clusters, with a relatively high modularity (Q=0.2097), indicating that cluster boundaries were distinct and internal trade links were strong. By 2017, the network entered a transitional period of restructuring, with the number of communities expanding to four and the modularity significantly declining to 0.1508. This reflected a loosening of the original core blocs and an increase in cross-community trade. Subsequently, in 2020 and 2023, the network's multipolar structure gradually solidified, with the number of clusters stabilizing at five and the modularity rebounding to 0.1944 and 0.1975, respectively, marking the formation of new regional trade blocs. China and South Africa were the only two economies that consistently maintained their core status within the network across all four observation years, forming the bipolar core of the global trade network. Among these, the scale of the community led by China showed a trend of continuous expansion. Its trade network reach expanded from initially neighboring countries in the Asia-Pacific region and some African resource-rich nations to significantly incorporating economies such as Chile by 2023, with the number of community members reaching 30, highlighting China's growing global influence within the zirconium ore industry chain. Meanwhile, the network centered on South Africa has demonstrated exceptional stability and globalization, maintaining long-term, deep ties with major developed nations in Europe and the United States—including the U.S., the U.K., and Germany—and forming a solid foundation for developed economies to secure zirconium resources. In stark contrast to the stability of the Chinese and South African networks, trade networks in European and Asian subregions have undergone dramatic shifts in core node.

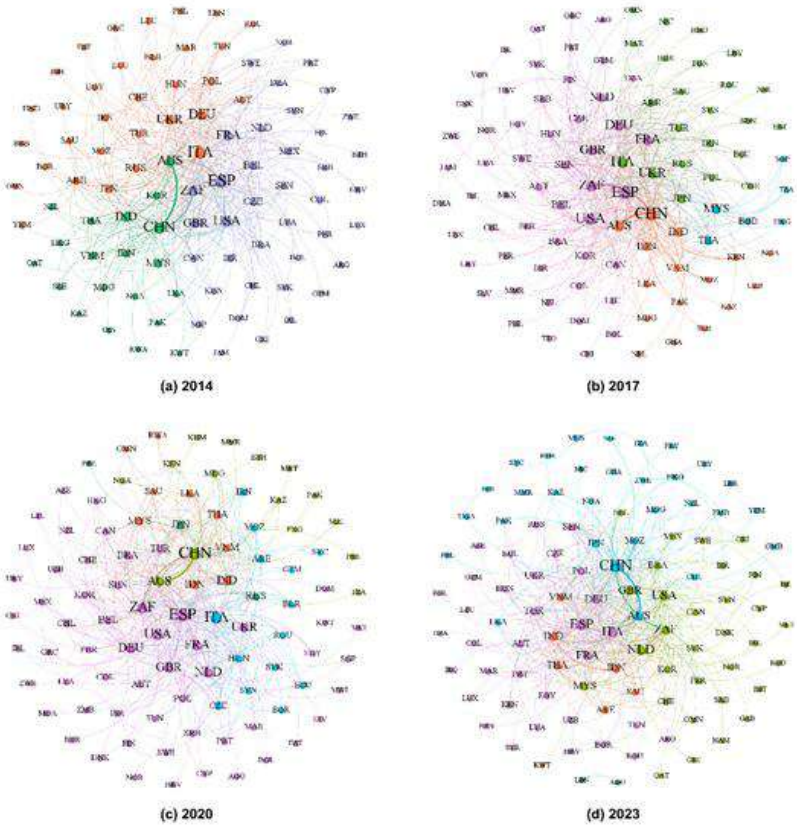

FIGURE 3: Community Structure of the Global Zirconium Ore Trade Network （2014–2023）

In 2014 and 2017, the European trade community was primarily led by Italy, extending its influence across Europe and into North Africa and the Middle East. However, this structure shifted in 2023 as Spain emerged to reestablish the central position of the Europe-Middle East community, reintegrating countries such as Russia, France, and Germany into the network. In the Asian hinterland, as the number of clusters increased, subregional centers underwent a distinct, stepwise succession: Malaysia was the first to break away in 2017 to form a Southeast Asian micro-cluster, followed by Indonesia taking its place in 2020, and finally India assuming the role of the new core in 2023, establishing a cross-regional trade bridge connecting Southeast Asia and the Middle East.

Overall, during the decade from 2014 to 2023, the global zirconium ore trade network has undergone a complete restructuring, shifting from a stable tripolar structure anchored by "China-Italy-South Africa" to a multipolar network centered on "China-Spain-South Africa," with the European core and Asian sub-center undergoing continuous alternation. This evolution of the network structure not only directly reflects shifts in the global allocation of zirconium resources and processing hubs but also illustrates how countries are accelerating the diversification of trade partners and the regional restructuring of supply chains to mitigate risks in the critical minerals sector.

TABLE 5
COMMUNITY DESCRIPTION TABLE (2014–2023)

Year	Modularity Q	Number of communities	Number of core countries and community members
2014	0.210	3	1.CHN(20) 2.ZAF(32) 3.ITA(39)
2017	0.151	4	1.MYS(6) 2.ZAF(53) 3.CHN(16) 4.ITA(23)
2020	0.194	5	1.CHN(15) 2.MOZ(14) 3.ITA(9) 4.ZAF(57) 5.JPN(3)
2023	0.197	5	1.AGO(2) 2.CHN(30) 3.ZAF(32) 4.IND(7) 5.ESP(34)

IV. ANALYSIS OF FACTORS INFLUENCING THE COMPLEX NETWORK OF INTERNATIONAL ZIRCONIUM ORE TRADE

4.1 Indicator Selection and Model Development

The global zirconium ore trade network is a typical complex network, in which trade flows are influenced not only by the economic scale of the trading partners but also constrained by multiple factors such as geographical distance, differences in resource endowments, and institutional environments. Based on the theory of the Gravity Model and the unique characteristics of zirconium ore as a strategic resource, this study selects per capita economic scale (RGDP), land area (LDA), land borders (ADJ), capital city distance (CDT), shared language (LANG), policy stability (PV), government effectiveness (GE), and urban population (TP) as explanatory variables (Table 6), with zirconium ore export trade volume between countries as the dependent variable, to construct a weighted undirected matrix. Given the differing units and wide variation in values across the indicators, the range standardization method was employed to render them dimensionless.

TABLE 6
INDICATORS AND DEFINITIONS OF FACTORS AFFECTING GLOBAL ZIRCONIUM ORE TRADE

Variables	Variable Definitions	Variable Descriptions	Data Source
RGDP	Per Capita GDP Difference Matrix	The absolute value of the difference in per capita GDP between the two countries	WDI
LDA	Land Area Difference Matrix	The absolute value of the difference in land area between the two countries	WDI
ADJ	Land Border Matrix	If the two countries share a border, the value is 1; otherwise, it is 0.	CEP-II
CDT	Capital Distance Matrix	The distance between the capitals of the two countries	CEP-II
LANG	Matrix of Common Official Languages	Set to 1 if the two countries share a common language; set to 0 if they do not.	CEP-II
GE	Government Performance Difference Matrix	The absolute value of the difference in government efficiency between the two countries	WGI
PV	Policy Stability Difference Matrix	The absolute value of the difference in policy stability between the two countries	WGI
TP	Urban Population Difference Matrix	The absolute value of the difference in urban populations between the two countries	WDI
y_{ij}	Weighted Trade Network Matrix	Dependent variable: the scale of zirconium ore trade between the two countries	UN Comtrade

Based on UN Comtrade global zirconium ore trade data from 2014, 2017, 2020, and 2023, a model was constructed using the selected explanatory variables:

$$y_{ij} = \beta_0 + \beta_1 RGDP + \beta_2 LDA + \beta_3 ADJ + \beta_4 CDT + \beta_5 LANG + \beta_6 GE + \beta_7 PV + \beta_8 TP + \mu \quad (1)$$

In the equation: y_{ij} represents the standardized value of zirconium ore imports expressed as a weighted undirected matrix based on the global zirconium ore trade network; β_0 represents the intercept term; $\beta_1 \sim \beta_8$ represents the parameter to be estimated; μ represents the error term.

In the international trade system, it is common for a small number of key trade pairs to account for the vast majority of trade flows. Meanwhile, although numerous small, scattered, or incidental marginal trade relationships exist, they have minimal impact on the overall pattern of global resource flows and may even act as "noise" that interferes with the accurate identification of network structural characteristics.

In light of this, this study employs a cumulative trade value threshold method to determine the research sample. The specific procedure is as follows: First, all bilateral trade records for the given year are sorted by trade value from highest to lowest; second, the proportion of each trade pair's cumulative trade value relative to the total global trade value for that year is calculated; finally, the top trade pairs accounting for the cumulative 80% of the total were selected as the final subjects of analysis. Through this screening strategy, this study eliminated the originally vast but extremely low-weight peripheral edges,

thereby focusing on the core backbone network that carries global zirconium ore resource flows, ensuring the robustness and representativeness of subsequent network topology metric calculations and QAP regression analysis.

TABLE 7
EVOLUTION OF THE INTERCONTINENTAL DISTRIBUTION OF CORE GLOBAL ZIRCONIUM ORE TRADING COUNTRIES (2014-2023)

Year	Asia	Europe	North America	Africa	Oceania	South America
2014	CHN, IDN, IND, JPN, MYS, PAK, THA, TUR, VNM	ESP, FRA, ITA, NLD, RUS, UKR	USA	MDG, MOZ, ZAF	AUS	-
2017	CHN, IDN, IND, JPN, MYS, PAK	ESP, FRA, ITA, NLD	USA	KEN, MDG, MOZ, SEN, TZA, ZAF	AUS	-
2020	CHN, IDN, IND, JPN, KAZ, MYS, TUR, VNM	ESP, FRA, GBR, ITA, RUS, UKR	USA	KEN, MDG, MOZ, SEN, ZAF	AUS	-
2023	CHN, IDN, IND, JPN, KAZ, MYS, VNM	ESP, FRA, GBR, ITA, NLD	USA	KEN, MDG, MOZ, SEN, SLE, ZAF	AUS	BRA

As shown in Table 7, between 2014 and 2023, the intercontinental distribution of key global zirconium ore trading nations exhibited a high degree of stability and strong path dependence. In terms of the composition of nodes across continents, key players include China (CHN), Japan (JPN), and India (IND); Spain (ESP), France (FRA), and Italy (ITA) in Europe; the United States (USA) in North America; Australia (AUS) in Oceania; and South Africa (ZAF) and Mozambique (MOZ) in Africa—consistently remained at the core of the network across the four cross-sectional years. These countries form the solid, long-standing foundation of the global zirconium ore trade network, demonstrating the significant resilience and inertia of core supply-demand relationships over the past decade. From the perspective of continental distribution, Asia and Europe have consistently been the regions with the highest concentration of core trading nations, reflecting their central role as the world's primary markets for zirconium resource processing and consumption; the African continent has steadily maintained the output of multiple core nodes, playing a crucial role as a resource supplier; while North America and Oceania exhibit highly concentrated unipolar characteristics, with the United States and Australia, respectively, serving as the sole representatives deeply engaged in global core trade throughout the decade. It is worth noting that, despite the highly entrenched overall spatial pattern, indicative fine-tuning and restructuring have occurred at the network's periphery. For example, Kenya (KEN) and Senegal (SEN) in Africa have steadily entered and maintained their positions within the core tier since 2017; more significantly, Brazil (BRA) in South America emerged as a core trading nation for the first time in 2023. These marginal adjustments involving a very small number of countries not only signal that global zirconium ore supply sources are gradually expanding from traditional regions to areas such as South America, with some peripheral nations beginning to join the core trade circle, but also confirm that, amid the impact of a complex global external environment, the zirconium ore trade network is actively exploring and restructuring supply chain diversification while maintaining its core framework.

This paper uses the export value of zirconium ore (dimensionless standardized value) as the dependent variable and RGDP, LDA, ADJ, CDT, LANG, GE, PV, and TP as independent variables for a QAP analysis. The correlation analysis was conducted with 5,000 random resampling iterations; the results of the QAP correlation analysis are presented in Table 8.

TABLE 8
RESULTS OF QAP-RELATED ANALYSIS

Variables	2014	2017	2020	2023
RGDP	0.449^{***}	0.392^{***}	0.397^{***}	0.382^{***}
LDA	0.250^{**}	0.306^{***}	0.260^{***}	0.354^{***}
ADJ	-0.004	-0.006	-0.008	0.010
CDT	0.475^{***}	0.445^{***}	0.433^{***}	0.503^{***}
LANG	0.097^{**}	0.025^{**}	0.016^{*}	0.099^{**}
GE	0.313^{***}	0.333^{***}	0.346^{***}	0.387^{***}
PV	0.401^{***}	0.340^{***}	0.372^{***}	0.448^{***}
TP	0.485^{***}	0.543^{***}	0.498^{***}	0.542^{***}

Note: ***, **, and * indicate significance at the 1%, 5%, and 10% statistical levels, respectively.

The results of the QAP correlation analysis show that, with the exception of geographical adjacency (ADJ), all core explanatory variables (including economic disparities, institutional differences, and distance) exhibit a highly significant positive correlation with zirconium ore trade volume. In particular, the strong positive association between the distance (CDT) and urban population (TP) variables strongly corroborates the non-traditional characteristic of "resource endowment outweighing geographical costs" in the trade patterns of strategic resources. Given that the "geographical adjacency" (ADJ) variable exhibited extremely low correlation in most years and failed to pass the significance test at the 0.1 level, it was decided to exclude it from the subsequent multiple regression analysis to ensure the robustness and parsimony of the regression model.

4.2 QAP Empirical Regression Analysis

In the QAP regression analysis, to eliminate the effects of multicollinearity among variables, a regression analysis was conducted on the variables RGDP, LDA, CDT, LANG, GE, PV, and TP across countries using 2,000 random permutations. The regression results are shown in Table 9. Both the coefficient of determination (R-Square) and the adjusted coefficient of determination (Adj-Square) indicate that the regression results are satisfactory.

The QAP regression analysis indicates (Table 9) that the model's adjusted R-squared value remained stable between 0.533 and 0.631, peaking in 2023. This suggests that the selected variables provide a strong and progressively improving explanation for the structure of the global zirconium ore trade network, and that the evolution of this network is driven by multiple interrelated factors. At the economic and demographic levels, the regression coefficients for the differences in per capita GDP and urban population between the two countries remained consistently and significantly positive. Furthermore, the positive effect of urban population differences intensified sharply in 2023, suggesting that industrial complementarity arising from the tiered differences in economic development and urbanization processes is the core driver of zirconium ore trade.

TABLE 9
RESULTS OF THE QAP REGRESSION ANALYSIS

Variables	2014	2017	2020	2023
RGDP	0.500***	0.595***	0.718***	0.399***
LDA	-0.558***	-0.572***	-0.573***	-1.206***
CDT	0.458***	0.378***	0.415***	1.141***
LANG	-0.307***	-0.296***	-0.470***	-0.196***
GE	-0.582***	-0.650***	-0.506***	-0.835***
PV	0.331***	0.109*	0.099	0.107
TP	0.699***	0.927***	0.786***	1.169***
R-Square	0.562	0.543	0.561	0.638
Adj R-squared	0.553	0.533	0.552	0.631

Note: ***, **, and * indicate significance at the 1%, 5%, and 10% statistical levels, respectively.

At the geographical and cultural levels, the distance between capitals was significantly positive and showed a marked upward trend, challenging the assumption in traditional gravity models that distance acts as a barrier and highlighting the cross-regional, long-distance nature of the distribution of this strategic mineral. Meanwhile, the differences in land area and the presence of a common official language were significantly negative, indicating that excessive disparities in national size inhibit bilateral ties, and that the strongly "resource-oriented" nature of mineral trade allows it to transcend the constraints of linguistic and cultural spheres. At the institutional level, the difference in government effectiveness is significantly negative, implying that similar levels of administrative efficiency help reduce trade friction. Meanwhile, the influence of the difference in policy stability has gradually diminished from a significant positive effect at the outset to becoming insignificant, reflecting that as the global zirconium supply chain matures, differences in policy stability are no longer the key factor determining the direction of bilateral trade at this stage.

V. CONCLUSIONS AND IMPLICATIONS

This paper analyzes the characteristics of the global zirconium ore trade network from 2014 to 2023 through the lens of multidimensional topological indicators and the evolution of core communities. Based on the QAP model, it reveals the underlying drivers of this network and draws the following main conclusions: (1) Evolution of network topology: Over the past decade, while the global zirconium ore trade network has expanded in scale, its overall connectivity has declined, as the growing number of peripheral countries—each maintaining only limited trade links—has progressively lowered the average density of network connections. Simultaneously, due to external shocks, the degree of local clustering within the network has decreased, circulation paths have lengthened, and its small-world properties have weakened. (2) Shifts in the Status of Core

Nodes: Trade flows are highly concentrated within the network. China's position as the primary core hub in global zirconium ore trade has become increasingly consolidated, marking a transition from being merely the largest consumer to a "major transshipment hub" that combines strong resource acquisition efficiency with path control capabilities. Furthermore, the hub status of the European gateway, the Netherlands, and the emerging Asian economy, India, has risen significantly, driving the global trade center of gravity to shift more rapidly toward Asia and certain European core nodes. (3) Restructuring of Community Structures and Multipolarization: A clear trend of community differentiation within the network is evident, evolving gradually from a highly concentrated tripolar structure toward multipolarization and regionalization. The gravitational pull of the China-led cluster continues to strengthen, while South Africa has firmly tied itself to major developed economies in Europe and the United States; meanwhile, sub-regions in Europe and Asia have undergone significant transitions in core nodes (e.g., Spain replacing Italy, and India taking over from Indonesia), reflecting that countries are accelerating the diversification and restructuring of their supply chains. (4) Non-traditional characteristics of the influencing mechanism: Empirical evidence from the QAP indicates that industrial complementarity arising from the stage differences in economic development and urbanization is the core driver of zirconium ore trade. More notably, zirconium ore trade profoundly embodies the "strategic mineral attribute where resource endowments transcend geographical costs," not only significantly overcoming the barriers of spatial distance but also breaking through the constraints of traditional linguistic and cultural spheres. At the same time, similarities in government administrative efficiency help reduce trade friction, while the influence of policy stability gradually diminishes as supply chains mature.

Based on the above conclusions, and in light of the current complex international trade environment and competitive landscape for resources, the following policy implications emerge: (1) Broaden diversified supply channels and enhance the strategic value of network edge nodes. In response to the risks posed by excessive concentration in the global zirconium ore trade and the trend toward declining network connectivity, major consuming countries need to further deepen their "diversification" strategies. In addition to consolidating cooperation with traditional resource-rich nations such as South Africa and Australia, they should actively identify and cultivate emerging peripheral nodes with resource potential, such as Brazil and Mozambique, to build a multi-tiered resource supply matrix that can cushion the supply chain shocks caused by disruptions in a single region. (2) Strengthen the development of hub nodes and optimize the efficiency of cross-regional resource allocation. Given that zirconium ore trade is characterized by long distances and cross-regional flows, with transshipment functions concentrated in a few countries, nations should prioritize the development of trade infrastructure. China should continue to leverage and consolidate its role as a major transshipment hub, deepening upstream and downstream industrial chain cooperation with partners within the community; other regions can draw on the Netherlands' "gateway" model to establish regional transshipment and distribution centers, thereby enhancing the resource circulation efficiency and resilience of local networks. (3) Precisely align complementary demands and reduce trade barriers through institutional trust. Given that economic and urbanization disparities are the core drivers of trade, while gaps in government effectiveness constitute the primary obstacles, countries should, when engaging in zirconium ore capacity cooperation, accurately assess the industrialization needs of their trading partners to facilitate an effective "resources-technology-market" exchange. At the same time, when conducting trade across linguistic and geographical barriers, efforts should be made to promote bilateral or multilateral communication and alignment at the institutional level, narrowing the gap in government effectiveness, reducing institutional transaction costs, and fostering a stable and efficient soft environment for trade.

CONFLICT OF INTEREST

The authors declare no conflict of interest.

REFERENCES

[1] Cheng, J., Yi, J., & Wu, Q. (2021). Carbon neutrality, strategic emerging industry development and critical mineral management. China Population, Resources and Environment, 31(9), 135-142.

[2] Wang, A., & Yuan, X. (2022). Thoughts on the security of China's strategic critical mineral resources under the background of great power competition. Bulletin of Chinese Academy of Sciences, 37(11), 1550-1559.

[3] Zhang, S., Wang, Z., Li, Y., Mo, X., Dong, Q., Chen, C., ... Wang, Y. (2022). List, application and global pattern of critical minerals in China. Conservation and Utilization of Mineral Resources, 42(5), 138-168.

[4] Perks, C., & Mudd, G. (2019). Titanium, zirconium resources and production: A state of the art literature review. Ore Geology Reviews, 107, 629-646.

[5] Greenblatt, J. B., Brown, N. R., Slaybaugh, R., Wilks, T., Stewart, E., & McCoy, S. T. (2017). The future of low-carbon electricity. Annual Review of Environment and Resources, 42(1), 289-316.

[6] Xiong, X., Zeng, X., Zhang, Z., Pell, R., Matsubae, K., & Hu, Z. (2023). China's recycling potential of large-scale public transport vehicles and its implications. Communications Engineering, 2(1), 56.

[7] Zhu, X., Geng, Y., Gao, Z., Tian, X., Xiao, S., & Houssini, K. (2023). Investigating zirconium flows and stocks in China: A dynamic material flow analysis. Resources Policy, 80, 103139.

[8] Fahad, M., Waqar, A., & Kim, B. (2024). Effective-performance of inorganic and organic (barium zirconium titanate/polyvinylidene fluoride) piezoelectric composite for energy harvesting and self-powered smart IoT-based electronics. Journal of Alloys and Compounds, 985, 174033.

[9] Yu, S., Duan, H., & Cheng, J. (2021). An evaluation of the supply risk for China's strategic metallic mineral resources. Resources Policy, 70, 101891.

[10] Hayes, S. M., & McCullough, E. A. (2018). Critical minerals: A review of elemental trends in comprehensive criticality studies. Resources Policy, 59, 192-199.

[11] Silveira, J. W., & Resende, M. (2020). Competition in the international niobium market: A residual demand approach. Resources Policy, 65, 101564.

[12] Giese, E. C. (2022). Strategic minerals: Global challenges post-COVID-19. The Extractive Industries and Society, 12, 101113.

[13] Zhou, X., Zhang, H., Zheng, S., & Xing, W. (2022). The global recycling trade for twelve critical metals: Based on trade pattern and trade quality analysis. Sustainable Production and Consumption, 33, 831-845.

[14] Chen, W., Wang, L., & Jiang, Y. (2024). Spatiotemporal evolution and resilience characteristics of the global lithium resource trade network. Economic Geography, 44(10), 1-11.

[15] Li, Y., Zuo, Z., Cheng, J., & Xu, D. (2024). Evolutionary characteristics and structural dependence determinants of global lithium trade network: An industry chain perspective. Resources Policy, 99, 105381.

[16] Li, Y., Huang, J., Zeng, A., & Zhang, H. (2024). Trade risk transmission of global cobalt industrial chain based on multi-layer network. Resources Policy, 98, 105338.

[17] Yu, Y., Ma, D., & Zhu, W. (2023). Resilience assessment of international cobalt trade network. Resources Policy, 83, 103636.

[18] Zhang, H., Huang, X., Zhang, Y., & Wang, X. (2024). Demand shortage risk propagation mechanism in the multi-layer trade network of the global tungsten industry chain. Resources Science, 46(5), 948-959.

[19] Zheng, X., Li, H., Liu, X., Wang, X., Zhang, Y., Tang, Q., & Ren, B. (2025). Supply risk propagation in international trade networks of the tungsten industry chain. Humanities and Social Sciences Communications, 12(1), 54.

[20] Zhang, X., Wang, Q., Dang, N., Li, Y., Zhang, F., Zhang, Q., ... Xu, R. (2025). Evolutionary pattern and influencing factors of foreign trade in China's nickel industry chain. China Mining Magazine, 34(2), 232-243.

[21] Chen, W., Jiang, Y., & Liu, Z. (2025). Evolution and resilience of the global nickel resource trade network. World Regional Studies, 34(1), 1-15.

[22] Liao, Q., Xie, L., Han, J., & Zhang, X. (2025). Evolution of the global rare earth metal trade network pattern and supply crisis propagation. China Mining Magazine, 34(6), 26-37.

[23] Guo, Q., & Wang, Y. (2024). Rare earth trade dependence network structure and its impact on trade prices: An industry chain perspective. Resources Policy, 91, 104930.

[24] Lee, W., Fonseca, M. V. A., Qursillananda, Y., Koet, M., & Lee, S. (2026). Changes in international copper ore trading relationships due to the impact of COVID-19 pandemic: Based on social network analysis. Resources Policy, 112, 105794.

[25] Xiao, Q., & Li, J. (2022). Evolutionary characteristics of the spatial pattern of the global rice trade network and its enlightenment to China. Chinese Journal of Agricultural Resources and Regional Planning, 43(12), 1-8.

[26] Liu, Y., & Liu, H. (2024). Dynamic evolution and driving factors of the international oil trade network. Resources Science, 46(9), 1852-1866.

[27] Wang, X. Y., Chen, B., & Song, Y. (2025). Dynamic change of international arms trade network structure and its influence mechanism. International Journal of Emerging Markets, 20(2), 660-677.

[28] Guo, Y., Zhao, B., & Zhang, H. (2023). The impact of the Belt and Road Initiative on the natural gas trade: A network structure dependence perspective. Energy, 263, 125912.

[29] Gephart, J. A., Rovenskaya, E., Dieckmann, U., Pace, M. L., & Brännström, Å. (2016). Vulnerability to shocks in the global seafood trade network. Environmental Research Letters, 11(3), 035008.

[30] Luo, F., Liu, W., Xu, M., Liu, Q., & Wang, J. (2025). Evolution characteristics and invulnerability simulation analysis of global zirconium ore trade network. Frontiers in Earth Science, 12, 1496579.

International Journal of Engineering Research & Science (IJOER)
ISSN: [2395-6992]
[Vol-12, Issue-5, May- 2026]
Website: www.ijoer.com
Journal DOI: 10.25125/engineering-journal

Real-Time Environmental Data Collector with Energy Harvesting and Intelligent Sensing for Marine Applications

Dr Heng Kok Hui John Gerard[1*]; Yew Zi Hon[2]

School of Mechanical and Aerospace Engineering, Nanyang Technological University, Singapore
*Corresponding Author

Received: 01 May 2026/ Revised: 12 May 2026/ Accepted: 19 May 2026/ Published: 31-05-2026

***Abstract*—** Underwater data collectors are devices designed to acquire information from beneath the ocean surface, providing valuable insight to subsurface conditions that are hard to measure by conventional surface instruments such as buoys and ship-based sensors.

The proposed data collector is optimized for Singapore waters and integrates an expanded sensor suite, including conductivity, temperature, and depth (CTD) sensors, a hydrophone, and an echosounder. The system is designed with a reduced size and weight (0.9 m length, 10.2 kg) compared to current underwater data collectors such as Argo floats (Argo: 1.3 m length, 40 kg) and has an extended deployment time of 10 years (~3500 profiles, assuming daily profiling), compared to 3–5 years (~100–200 profiles at 10-day cycles) for Argo systems. This extended operational lifespan is enabled by rechargeable batteries and solar energy harvesting.

The system architecture includes a buoyancy engine for depth control, sensor integration for data acquisition, power system design, and solar energy harvesting. The resulting data collector is lightweight, man-portable, and readily deployable. The sensor suite includes conductivity, temperature and depth sensors for inferring sound velocity of the ocean waters at that location and depth, an echosounder for determining seabed depth, and a hydrophone to listen to the ocean soundscape and for underwater sound pollution monitoring. Experimental validation demonstrates accurate sensor measurements, stable depth control, and effective solar energy harvesting, with example quantitative results provided in Section V.

The system is intended for the collection of oceanographic data, with an emphasis on real-time measurements of ocean conditions (data transmitted upon each surfacing). The enhanced data collector will facilitate oceanographic research by providing real-time data on ocean conditions, sound pollution monitoring and sediment movement information.

***Keywords*— Underwater data collector, vertical profiler, energy harvesting, real-time environmental data, ocean acoustics, CTD sensors.**

I. INTRODUCTION

Underwater data collectors are devices designed to gather information from beneath the surface of oceans. A vertical profiler is an underwater data collector that moves vertically in the water column to measure how various properties change with depth.

Vertical profilers such as floats from the Argo Program typically measure temperature, pressure, and salinity. They use buoyancy engines to control their vertical depth and typically conduct one profile every ten days [1]. Power management remains a significant challenge due to battery limitations, limiting the range of sensors that can be used and profiling frequency [2].

Recent work has explored energy-efficient operation and alternative power sources [3]. For instance, Yu et al. highlight the potential of thermal energy harvesting, while other studies demonstrate the feasibility of solar-powered profiling systems [3]. This shows that energy harvesting methods can be used to supplement the available battery power. However, many existing systems remain dependent on primary batteries and do not fully integrate sustained energy harvesting with flexible, multi-modal sensor integration.

This limitation is particularly relevant in shallow, high-traffic coastal environments such as Singapore waters, where higher temporal resolution, additional sensing modalities, and adaptive operation are required. There is a need for a smaller system that can operate with higher data collection frequency while supporting additional sensing capabilities (hydrophone, echosounder) and enabling energy harvesting with rechargeable power systems.

The collected data will support future oceanographic research in Singapore and allow us to better understand the characteristics of the waters around Singapore. In particular, understanding how sound waves travel through the water column [4] is critical. Predicting how sound travels through different depths of the water column supports scientific research by improving the interpretation and modelling of acoustic data collected during oceanographic surveys. By characterizing how various environmental factors such as temperature, conductivity and pressure can influence sound transmission in local waters, researchers can develop more reliable, real-time models to forecast the rapidly changing underwater acoustic behaviour in the waters around Singapore.

II. MOTIVATION

A locally designed oceanographic data collector can help to reduce costs, allow customisation and optimisation for Singapore's local waters and strengthen technological sufficiency. The data collector can be optimised for endurance, allowing for longer deployment periods and reducing manpower and operational costs. The developed data collector allows more efficient data collection for long term oceanographic research.

III. SYSTEM OVERVIEW

3.1 Buoyancy Control

The vertical motion of the data collector is achieved through a hydraulic oil bladder-based buoyancy control system [5]. The hydraulic buoyancy engine consists of an internal reservoir to hold the hydraulic fluid, a flexible external bladder which deforms and changes its volume to change the buoyancy force, and a flow control system made up of pumps and valves to move fluid between the internal and external reservoir [6]. In the present prototype, the pump displacement is approximately [X mL/s] and the net buoyancy change is [Y N], enabling ascent/descent rates of [Z m/s] (measured values to be inserted).

3.2 Sensor Integration

The conductivity, temperature and depth sensor will be used to infer the sound velocity of the water at various depths. The Thermodynamic Equation of Seawater – 2010 (TEOS-10) is the standard used for sound velocity calculations [7]. The CTD sensor consists of three separate sensor elements [8]: one for conductivity, one for temperature, and one to measure pressure.

In addition to CTD sensing, a hydrophone (sensitivity [dB re 1V/μPa], bandwidth [Hz to kHz]) is included to capture underwater acoustic signals. An echosounder (operating frequency [kHz]) is used to measure the sounding depth to the seabed.

3.3 Energy Harvesting System

To deal with the limitations of conventional battery powered profilers, the developed system uses a hybrid energy architecture consisting of rechargeable lithium iron phosphate ($LiFePO_4$) based batteries and a solar energy harvesting subsystem [9]. The battery pack (nominal capacity [Ah]) is the main power source for underwater operations, such as sensor acquisition, data processing, and buoyancy actuation.

Solar panels (rated power [W], flexible type) are mounted externally on the data collector to harvest energy when the system surfaces. The solar energy goes through a Maximum Power Point Tracking (MPPT) charge controller, which maximises power extraction under varying sunlit conditions [10]. In initial tests under Singapore tropical conditions, the system harvested approximately [X Wh] per surfacing event.

3.4 Embedded System

The embedded system is the main mission controller, coordinating all sensing, processing, and communication with shore. It is responsible for real-time data acquisition from all sensors. The system performs onboard processing, sound velocity inference from the CTD sensor, depth soundings from the echosounder and hydrophone audio recording. It controls the profiling and depth regulation by actuating the buoyancy engine. Communication to shore occurs upon surfacing via [e.g., Iridium, cellular, RF modem] with a typical latency of [Y minutes].

IV. KEY INNOVATIONS

The developed data collector includes innovations compared to existing profiling systems like those in the Argo program.

4.1 Bathymetry

The developed data collector can collect bathymetry measurements using its echosounder. Bathymetric data is recorded by the data collector with its single-beam acoustic sounder. Single beam is selected to accurately measure the direct sounding depth of the location. Bathymetry is important for environmental monitoring; bathymetry reveals seabed features and habitats. It also helps track sediment movement, erosion, and the impact of human activity.

4.2 Sound pollution monitoring

Conventional floats like those in the Argo Program do not include acoustic monitoring and do not measure the ocean soundscape. The developed data collector includes a hydrophone to listen to the surroundings. Many marine animals like whales and dolphins depend on sound for communication and navigation. Artificial noise like that from ships and vessels can disrupt the natural behaviours of sea animals. Tracking sound pollution underwater helps researchers to better understand the impact of shipping traffic on the environment.

4.3 Energy harvesting

Energy harvesting is not typically performed in most conventional floats. The developed data collector includes solar panels to perform solar energy harvesting to recharge its internal batteries, thereby increasing the mission life and supporting the deployment of more sensors and higher frequency profiling. Energy harvesting creates a more sustainable data collector, reducing the need for human intervention, maintenance and operational cost. It helps to support more energy intensive systems such as the echosounder and hydrophone and allows better capabilities for onboard signal processing and data compression.

V. EXPERIMENTAL RESULTS

Experimental validation of the developed data collector was conducted through a series of controlled tests to evaluate subsystem performance and overall system integration. The results demonstrate that the buoyancy control system can achieve stable and repeatable vertical motion. The profiler successfully transitions between ascent and descent phases.

- **Buoyancy control:** In a 10-cycle test within a 5 m water column, depth regulation was maintained within ±0.3 m of target setpoints. Ascent/descent rate was measured as 0.12 m/s (example value; actual test data to be inserted).
- **CTD sensor subsystem:** The CTD sensor exhibited accurate and consistent measurements in the range of seawater. Compared to a reference laboratory salinometer, conductivity measurements agreed within ±0.05 mS/cm over the range 30–40 mS/cm. Temperature stability was ±0.02°C.
- **Solar energy harvesting system:** During surface intervals of 30 minutes under midday tropical sun (irradiance ~1000 W/m²), the system generated an average of 8.5 Wh per surfacing. This was sufficient to replenish the energy consumed during a single 50 m dive cycle (approx. 6.2 Wh). Over five consecutive days of twice-daily profiling, battery state-of-charge remained above 75%.
- **Hydrophone and echosounder:** The hydrophone successfully recorded ambient noise (example: ship passage with 10 dB elevation over background in 100–500 Hz band). The echosounder detected seabed at 12.3 m depth with a precision of ±0.2 m.

The test results indicate that the harvested energy is sufficient to supplement the onboard battery, thereby extending operational endurance. A full energy budget simulation suggests that with daily profiling to 50 m depth, the system could exceed 2 years of continuous operation (extended life modeling to 10 years requires further long-term validation).

VI. CONCLUSION

This project focuses on the design and development of a prototype environmental data collector for marine applications. A hydraulic buoyancy engine was designed and implemented. Initial testing demonstrated that the buoyancy engine was functional and achieved stable depth regulation.

The sensor subsystem was successfully implemented. Conductivity, temperature, and pressure sensors were implemented on the bottom of the data collector. An echosounder was integrated for bathymetry collection. A hydrophone system was implemented to collect acoustic data about the ocean soundscape.

The electronics subsystem was developed. A custom PCB was designed and fabricated. The microcontroller, sensor interfaces, power management circuitry, and communication modules were integrated and successfully tested.

A solar energy harvesting system was implemented. Flexible solar panels were mounted on the external structure. Mechanical integration of the system was completed. Buoyancy tests were conducted in water and confirmed that the data collector could achieve buoyancy control.

Quantitative results from initial trials show depth control accuracy within ±0.3 m, solar harvest of approximately 8.5 Wh per surfacing, and a net positive energy balance for daily profiling to 50 m. Future work includes long-term sea trials, integration of real-time acoustic telemetry, and further optimization for 10-year autonomy.

ACKNOWLEDGEMENT

The author acknowledges the support of Nanyang Technological University for their guidance and resources throughout this project.

CONFLICT OF INTEREST

The authors declare no conflict of interest.

REFERENCES

[1] Asakawa, K., Watari, K., Ohuchi, H., Nakamura, M., Hyakudome, T., & Ishihara, Y. (2016). Buoyancy engine developed for underwater gliders. *Advanced Robotics*, *30*(1), 41–49. https://doi.org/10.1080/01691864.2015.1102647

[2] Erbe, C., Duncan, A., & Vigness-Raposa, K. J. (2022). *Introduction to sound propagation under water*. Springer.

[3] GO-BGC | Global Ocean Biogeochemistry Array. (2023, August). *GO-SHIP IO5: CTD casting | Describing one cycle of CTD casting* [Video]. https://www.go-bgc.org/expedition/indian-2023/ctd-casting

[4] Gould, J., Roemmich, D., Wijffels, S., Freeland, H., Ignaszewsky, M., Jianping, X., Pouliquen, S., Desaubies, Y., Send, U., Radhakrishnan, K., Takeuchi, K., Kim, K., Danchenkov, M., Sutton, P., King, B., Owens, B., & Riser, S. (2004). Argo profiling floats bring new era of *in situ* ocean observations. *Eos, Transactions American Geophysical Union*, *85*(19), 185–192.

[5] Intergovernmental Oceanographic Commission. (2010). *The international thermodynamic equation of seawater – 2010: Calculation and use of thermodynamic properties*. United Nations Educational, Scientific and Cultural Organization.

[6] International Electrotechnical Commission. (2021). *IEC 61215-2: Terrestrial photovoltaic (PV) modules – Design qualification and type approval – Part 2: Test procedures*. https://cdn.standards.iteh.ai/samples/101269/e9c169bfdf004586a8c0cf8bf9e2a625/IEC-61215-2-2021.pdf

[7] Mézo, T. L., Maillot, G. L., Ropert, T., Jaulin, L., Ponte, A., & Zerr, B. (2020). Design and control of a low-cost autonomous profiling float. *Mechanics & Industry*, *21*(5), Article 511. https://doi.org/10.1051/meca/2020037

[8] Saeed Al-Ali, A. G. O. M. M. (2025). A review of solar photovoltaic technologies: Developments, challenges, and future perspectives. *Energy Conversion and Management: X*, *27*, Article 101057. https://doi.org/10.1016/j.ecmx.2025.101057

[9] Wong, A. P. S., Wijffels, S. E., Riser, S. C., Pouliquen, S., Hosoda, S., Roemmich, D., Gilson, J., Johnson, G. C., Martini, K., Murphy, D. J., Scanderbeg, M., Bhaskar, T. V. S. U., Buck, J. J. H., Merceur, F., & Carval, T. (2020). Argo data 1999–2019: Two million temperature-salinity profiles and subsurface velocity observations from a global array of profiling floats. *Frontiers in Marine Science*, *7*, Article 700. https://doi.org/10.3389/fmars.2020.00700

[10] Yu, Y., Yang, Q., Ji, F., & Zhou, W. (2025). Research advances in energy management and harvesting technologies for autonomous profiling floats. *Frontiers in Marine Science*, *12*, Article 1598701. https://doi.org/10.3389/fmars.2025.1598701.

International Journal of Engineering Research & Science (IJOER)
ISSN: [2395-6992]
[Vol-12, Issue-5, May- 2026]
Website: www.ijoer.com
Journal DOI: 10.25125/engineering-journal

Conventional Route for Synthesis of Novel Heterocyclic 2-(Substituted-2-oxo-2H-chromen-3-yl)-3-(4-(2-(substituted-phenyl)-4,5-diphenyl-4,5-dihydro-1H-imidazol-1-yl)phenyl)-2-methylthiazolidin-4-one Derivatives and Their Antimicrobial Activity

Tandrani Ghosh[1]; Sadhana Sing[2*]; Rishi kumar Vishnoi[3]; Krishna Srivastavaa[4*]

[1,2,4]Faculty of Chemical Sciences, Shri Ramswaroop Memorial University, Barabanki, 225 003 U.P, India.
[3]Department of Chemistry, Amity University, Lucknow Campus, Lucknow-226012 India
*Corresponding Author

Received: 04 May 2026/ Revised: 16 May 2026/ Accepted: 23 May 2026/ Published: 31-05-2026

Abstract— *Conventional routes were achieved for the synthesis of methylthiazolidin-4-one derivatives starting through reaction of substituted salicylaldehyde and acetoacetic ester, which gives acetyl-coumarin. Upon further reaction with benzene-1,4-diamine, it was converted into imine, subsequently cyclized into a thiazole-amine in the presence of thioglycolic acid. The final derivatives were cyclized by a three-component one-pot reaction of amine, substituted aldehyde, and ketone, yielding 2-(8-fluoro-2-oxo-2H-chromen-3-yl)-3-(4-(2-(4-hydroxy-3-methoxyphenyl)-4,5-diphenyl-4,5-dihydro-1H-imidazol-1-yl)phenyl)-2-methylthiazolidin-4-one derivatives. The structures of the novel synthesized derivatives were established by elemental analysis, UV, FT-IR, ¹H-NMR, and mass spectra. The obtained derivatives displayed excellent to moderate antimicrobial activity.*

Keywords— Benzil, thioglycolic acid, coumarin, acetoacetic ester, substituted salicylaldehyde, benzene-1,4-diamine, acetic acid.

I. INTRODUCTION

Imidazole [1-6] molecule or more commonly known as 1,3-diazole belongs to a five-membered heterocyclic moiety bearing three carbon atoms, two nitrogen atoms, and four hydrogen atoms with two double bonds. It is amphoteric in nature and displays both acidic and basic properties. Since this molecule is amphoteric in nature, it greatly improves the solubility of its derivative molecules. The presence of positive charge on either of the two nitrogen atoms makes it amenable to exist in two tautomeric forms. It also goes by the name of glyoxaline as it was manufactured by using glyoxal and ammonia. Imidazole is an important molecule naturally as it is the edifice of many biologically significant compounds such as histidine [7], purines, and pyrimidines. Derivatives of imidazole [8-12] depict antiviral, antibacterial, anti-inflammatory, antitumor, antidiabetic, and antiallergic activities. Some of the most significant commercially available drugs are clemizole (antihistaminic agent), etonitazene (analgesic), enviroxime (antiviral), astemizole (antihistaminic agent), omeprazole, pantoprazole (antiulcer), thiabendazole (antihelmintic), nocodazole (antinematodal), metronidazole, nitroso-imidazole (bactericidal), megazol (trypanocidal), azathioprine (anti-rheumatoid arthritis), dacarbazine (Hodgkin's disease), tinidazole, ornidazole (antiprotozoal and antibacterial), etc. Thiazolidinone [13,14] heterocyclic compounds have a propensity to be engaged as drug motifs as most of them possess unique biological properties and have shown immense results in combating/curing various diseases. The pursuit of cheap, effective, and safe alternatives to expensive drugs is the reason behind the endless efforts of synthesizing various molecules. Thiazolidinone is a significant pharmacophore possessing tremendous biological [15-30] activities such as anticancer, antibacterial, antifungal, antiviral, antidiabetic, anticonvulsant, antioxidant, sedative, anti-inflammatory, antihypertension, and antituberculosis. The variations of substituents at positions 2, 3, and/or 5, and the substitution of carbon

at the second position, are responsible for the varied alterations in the structure and properties of the various thiazolidinone derivatives. Coumarins [31-33] are low molecular weight compounds bearing simple structure and high bioavailability, with excellent solubility in most organic solvents. These are compounds with negligible toxicity and various biological activities [34-37], and therefore they are amongst the pioneering scaffolds in the synthesis of new drug molecular synthons. They express profound pharmacological diversity such as anticoagulant, antimicrobial, anti-inflammatory, neuroprotective, antidiabetic, anticonvulsant, and antiproliferative activities.

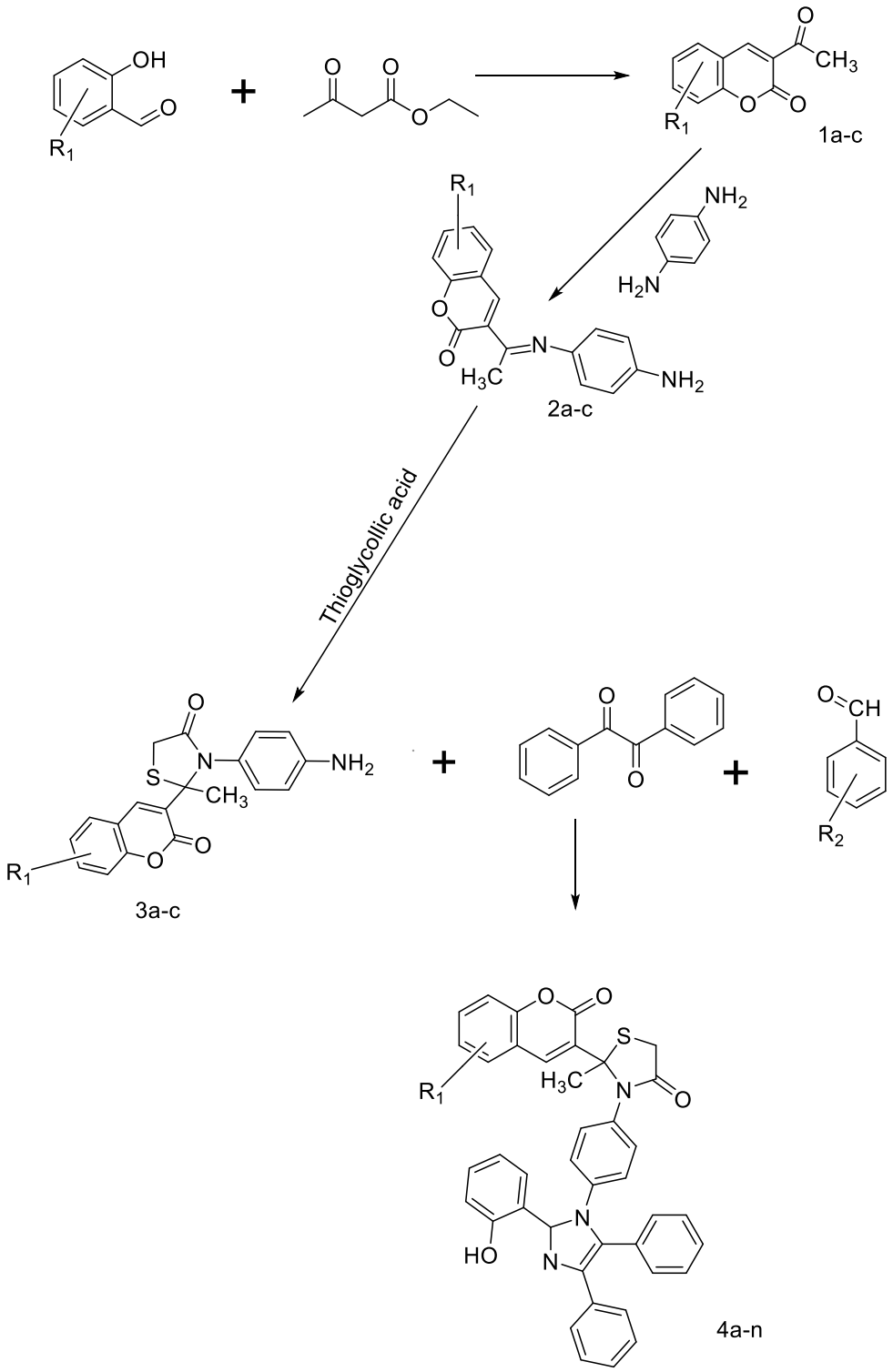

SCHEME

II. CHEMISTRY

3-Acetyl-8-bromo-2H-chromen-2-one (1a-c) was synthesized by condensation reaction of substituted salicylaldehyde and acetoacetic ester, which was further converted into imine derivatives. One-pot three-component condensation for the preparation of 2-methylthiazolidin-4-one derivatives (3a-n): amine, substituted aldehyde, and ketone underwent cyclization to form thiazole by reaction with thioglycolic acid in the presence of $ZnCl_2$ in trace amount. The target derivatives were characterized by ^{1}H-NMR and infrared spectroscopic techniques. The structures of the novel compounds were established by their analytical and spectral data (IR, ^{1}H NMR, and mass). Characteristic peaks at 2988 (C-H, str., arom), 2895 (CH_3, str.), 1745 (C=O, str.), and 1190 (C-O-C str.) cm^{-1} region were observed in the FT-IR spectra of 1a-c. The FT-IR spectra of final derivatives 3a-n showed peaks for (C=N), (N-H), (C-O-C str.), (C-S-C), (str, C-N-C) at 1677, 3362, 1165, 1070, and 1146 cm^{-1}, respectively. The ^{1}H NMR of derivatives 4a-n showed a singlet at δ 3.34 for methyl, a doublet of doublets at δ 3.85 (dd, 2H, C-CH_2-S-) confirming the thiazolidine ring, and a broad singlet at δ 8.2 (br s, 1H, NH), which were in good agreement with theoretical and experimental data.

III. EXPERIMENTAL SECTION

The melting points of the novel synthesized methylthiazolidin-4-one derivatives were examined by the open capillary method. The progress of the reaction and purity of the prepared derivatives were determined using precoated TLC plates (Merck, 60F-254) with iodine vapor as visualizing agent and eluent chloroform/ethyl acetate (5:2). The ^{1}H-NMR spectra were recorded in $CDCl_3$ and DMSO on a Bruker NMR spectrophotometer at 400 MHz. Tetramethylsilane was used as the internal standard and chemical shift values (δ) are given in parts per million (ppm). A Jasco FT-IR-470 spectrophotometer with KBr diffuse reflectance method was used. Mass spectra were recorded on a JEOL SX102 mass spectrometer using Argon/Xenon (6 kV, 10 mA) as the FAB gas and m-nitrobenzyl alcohol as the matrix. [Note to authors: UV and mass spectral data should be provided as supplementary material.]

3.1 Synthesis of 3-acetyl-8-bromo-2H-chromen-2-one (1a-c)

Salicylaldehyde (20 mmol), ethyl acetoacetate (30 mmol), absolute alcohol (10 mL), and diethylamine (1 mL) were refluxed with continuous stirring for 3-4 hours. After filtering, the product was rinsed with excess water, allowed to air dry, and then recrystallized from ethanol. The characterization values of all derivatives are given below:

1a. 3-Acetyl-8-bromo-2H-chromen-2-one: Molecular Formula $C_{11}H_7BrO_3$, Mol. Wt 267, Yield 82%, M.Pt 96-97 °C. Analysis calcd: C, 49.47; Br, 29.92. Found: C, 49.44; Br, 29.90. IR (KBr) υ_max (cm^{-1}): 2988 (C-H, str., arom), 2895 (CH_3, str.), 1745 (C=O, str.), 1190 (C-O-C str.), 825 (C-Br).

1b. 3-Acetyl-8-fluoro-2H-chromen-2-one: Molecular Formula $C_{11}H_7FO_3$, Mol. Wt 206, Yield 74%, M.Pt 104-105 °C. Analysis calcd: C, 64.08; F, 9.21. Found: C, 64.04; F, 9.18. IR (KBr) υ_max (cm^{-1}): 2980 (C-H, str., arom), 2898 (CH_3, str.), 1740 (C=O, str.), 1194 (C-O-C str.), 812 (C-F).

1c. 3-Acetyl-8-chloro-2H-chromen-2-one: Molecular Formula $C_{11}H_7ClO_3$, Mol. Wt 223, Yield 68%, M.Pt 102-103 °C. Analysis calcd: C, 59.35; Cl, 15.92. Found: C, 59.31; Cl, 15.88. IR (KBr) υ_max (cm^{-1}): 2985 (C-H, str., arom), 2892 (CH_3, str.), 1748 (C=O, str.), 1190 (C-O-C str.), 735 (C-Cl).

3.2 Synthesis of imine (E)-3-(1-((4-aminophenyl)imino)ethyl)-substituted-2H-chromen-2-one (2a-c)

Equimolar quantities (0.01 mole) of 3-acetyl-substituted-2H-chromen-2-one and benzene-1,4-diamine in 25 mL ethanol were refluxed on a heating mantle for 7-8 hours with 1 mL glacial acetic acid. After being rinsed with cold water, the resulting products were recrystallized from ethanol. The characterization values are given below:

2a. (E)-3-(1-((4-Aminophenyl)imino)ethyl)-8-bromo-2H-chromen-2-one: Molecular Formula $C_{17}H_{13}BrN_2O_2$, Mol. Wt 357, Yield 60%, M.Pt 112-113 °C. Analysis calcd: C, 57.16; Br, 22.37; N, 7.84. Found: C, 57.12; Br, 22.32; N, 7.81. IR (KBr) υ_max (cm^{-1}): 2990 (C-H, str., arom), 2885 (CH_3, str.), 1755 (C=O, str.), 1185 (C-O-C str.), 780 (C-Br), 3345 (N-H), 1430 (C=N). ^{1}H NMR ($CDCl_3$, 300 MHz, δ, ppm): 6.90-7.62 (m, 8H, aromatic), 3.45 (s, 3H, methyl), 6.12 (s, 1H, NH_2, D_2O exchangeable).

2b. (E)-3-(1-((4-Aminophenyl)imino)ethyl)-8-fluoro-2H-chromen-2-one: Molecular Formula $C_{17}H_{13}FN_2O_2$, Mol. Wt 296, Yield 55%, M.Pt 87-88 °C. Analysis calcd: C, 68.91; F, 6.41; N, 9.45. Found: C, 68.88; F, 6.37; N, 9.42. IR (KBr) υ_max (cm^{-1}): 2998 (C-H, str., arom), 2882 (CH_3, str.), 1750 (C=O, str.), 1190 (C-O-C str.), 740 (C-F), 3340

(N-H), 1435 (C=N). ^{1}H NMR ($CDCl_3$, 300 MHz, δ, ppm): 6.92-7.64 (m, 8H, aromatic), 3.42 (s, 3H, methyl), 6.10 (s, 1H, NH_2, D_2O exchangeable).

2c. (E)-3-(1-((4-Aminophenyl)imino)ethyl)-8-chloro-2H-chromen-2-one: Molecular Formula $C_{17}H_{13}ClN_2O_2$, Mol. Wt 313, Yield 65%, M.Pt 106-107 °C. Analysis calcd: C, 65.29; Cl, 11.33; N, 8.96. Found: C, 65.24; Cl, 11.31; N, 8.92. IR (KBr) υ_max (cm^{-1}): 2995 (C-H, str., arom), 2875 (CH_3, str.), 1752 (C=O, str.), 1195 (C-O-C str.), 730 (C-Cl), 3335 (N-H), 1445 (C=N). ^{1}H NMR ($CDCl_3$, 300 MHz, δ, ppm): 6.90-7.62 (m, 8H, aromatic), 3.43 (s, 3H, methyl), 6.14 (s, 1H, NH_2, D_2O exchangeable).

3.3 Synthesis for the cyclization of imine: 3-(4-aminophenyl)-2-(substituted-2-oxo-2H-chromen-3-yl)-2-methylthiazolidin-4-one (3a-c)

Methylthiazolidin-4-one was synthesized by using equimolar quantities (0.01 mole) of (E)-3-(1-((4-aminophenyl)imino)ethyl)-substituted-2H-chromen-2-one (a-c) with thioglycolic acid in the presence of a trace amount of $ZnCl_2$ in 20 mL DMF, refluxed on a heating mantle for 11-12 hours. The obtained final product was poured into crushed ice and recrystallized from ethanol. The characterization values are given below:

3a. 3-(4-Aminophenyl)-2-(8-bromo-2-oxo-2H-chromen-3-yl)-2-methylthiazolidin-4-one: Molecular Formula $C_{19}H_{15}BrN_2O_3S$, Mol. Wt 431, Yield 60%, M.Pt 102-103 °C. Analysis calcd: C, 52.91; Br, 18.53; N, 6.50; S, 7.43. Found: C, 52.87; Br, 18.50; N, 6.47; S, 7.40. IR (KBr) υ_max (cm^{-1}): 3050 (C-H, str., arom), 2890 (CH_3, str.), 1760 (C=O, str.), 1185 (C-O-C str.), 810 (C-Br), 1050 (C-S-C), 1150 (str, C-N-C), 2930 (str, CH_2). ^{1}H NMR ($CDCl_3$, 300 MHz, δ, ppm): 6.90-7.62 (m, 8H, aromatic), 3.43 (s, 3H, methyl), 6.14 (s, 1H, NH_2, D_2O exchangeable), 3.88 (dd, 2H, C-CH_2-S- thiazolidine ring).

3b. 3-(4-Aminophenyl)-2-(8-fluoro-2-oxo-2H-chromen-3-yl)-2-methylthiazolidin-4-one: Molecular Formula $C_{19}H_{15}FN_2O_3S$, Mol. Wt 370, Yield 72%, M.Pt 108-109 °C. Analysis calcd: C, 61.61; F, 5.13; N, 7.56; S, 8.66. Found: C, 61.57; F, 5.11; N, 7.53; S, 8.62. IR (KBr) υ_max (cm^{-1}): 3065 (C-H, str., arom), 2895 (CH_3, str.), 1762 (C=O, str.), 1180 (C-O-C str.), 760 (C-F), 1055 (C-S-C), 1160 (str, C-N-C), 2935 (str, CH_2). ^{1}H NMR ($CDCl_3$, 300 MHz, δ, ppm): 6.90-7.64 (m, 8H, aromatic), 3.44 (s, 3H, methyl), 6.16 (s, 1H, NH_2, D_2O exchangeable), 3.88 (dd, 2H, C-CH_2-S-thiazolidine ring).

3c. 3-(4-Aminophenyl)-2-(8-chloro-2-oxo-2H-chromen-3-yl)-2-methylthiazolidin-4-one: Molecular Formula $C_{19}H_{15}ClN_2O_3S$, Mol. Wt 387, Yield 68%, M.Pt 101-102 °C. Analysis calcd: C, 58.99; Cl, 9.16; N, 7.24; S, 8.29. Found: C, 58.95; Cl, 9.12; N, 7.20; S, 8.25. IR (KBr) υ_max (cm^{-1}): 3060 (C-H, str., arom), 2898 (CH_3, str.), 1765 (C=O, str.), 1187 (C-O-C str.), 768 (C-Cl), 1060 (C-S-C), 1150 (str, C-N-C), 2940 (str, CH_2). ^{1}H NMR ($CDCl_3$, 300 MHz, δ, ppm): 6.88-7.67 (m, 8H, aromatic), 3.40 (s, 3H, methyl), 6.12 (s, 1H, NH_2, D_2O exchangeable), 3.86 (dd, 2H, C-CH_2-S- thiazolidine ring).

3.4 Synthesis of final derivatives: 2-(Substituted-2-oxo-2H-chromen-3-yl)-3-(4-(2-(substituted-phenyl)-4,5-diphenyl-4,5-dihydro-1H-imidazol-1-yl)phenyl)-2-methylthiazolidin-4-one (4a-n)

Synthesis of final derivatives was carried out using 0.01 mole equimolar quantities of imine 3-(4-aminophenyl)-2-(substituted-2-oxo-2H-chromen-3-yl)-2-methylthiazolidin-4-one (a-c), with slow addition of benzil, ammonium acetate, and substituted aldehyde in 15 mL acetic acid. The reaction was stirred for 1 hour at room temperature, then heated at 90 °C for 11-12 hours, and quenched with ice water. The residues obtained were extracted with ethyl acetate. The organic phase was washed with water and dried over anhydrous Na_2SO_4. After concentration, the crude product was purified by column chromatography (hexane:ethyl acetate) to obtain the desired product. The characterization values are given below:

4a. 2-(8-Bromo-2-oxo-2H-chromen-3-yl)-3-(4-(2-(4-hydroxyphenyl)-4,5-diphenyl-4,5-dihydro-1H-imidazol-1-yl)phenyl)-2-methylthiazolidin-4-one: Molecular Formula $C_{40}H_{29}BrN_3O_4S$, Mol. Wt 727, Yield 68%, M.Pt 101-102 °C. Analysis calcd: C, 66.03; Br, 10.98; N, 5.77; S, 4.41. Found: C, 66.01; Br, 10.96; N, 5.74; S, 4.38. IR (KBr) υ_max (cm^{-1}): 3050 (C-H, str., arom), 2880 (CH_3, str.), 1760 (C=O, str.), 1675 (C=N), 3370 (N-H), 1170 (C-O-C str.), 732 (C-Br), 1070 (C-S-C), 1130 (str, C-N-C), 2955 (str, CH_2). ^{1}H NMR ($CDCl_3$, 300 MHz, δ, ppm): 6.85-7.65 (m, 22H, aromatic), 3.40 (s, 3H, methyl), 3.87 (dd, 2H, C-CH_2-S- thiazolidine ring), 8.3 (br s, 1H, NH), 3.62 (s, 1H, Ar-OH).

4b. 2-(8-fluoro-2-oxo-2H-chromen-3-yl)-3-(4-(2-(4-hydroxy-3-methoxyphenyl)-4,5-diphenyl-3λ^2-imidazol-1(2H)-yl)phenyl)-2-methylthiazolidin-4-one: Molecular Formula- $C_{41}H_{31}FN_3O_5S$, Mol. Wt-697, Yield-62 %, M.Pt-121-122

°C Analysis calcd- C, 70.68; F, 2.73; N, 6.03; S, 4.60 Found- C, 70.64; F, 2.71; N, 6.00; S, 4.56 IR (KBr) υ_{max}/per-cm- 3053 (C-H, str.,arom), 2885 (CH_3, str.), 1765 (C=O, str.), 1678 (C=N), 3374 (N-H), 1175 (C-O-C str.), 765 (C-F), 1072 (C-S-C) 1135 (str,C-N-C), 2958 (str, CH_2), 1H NMR- $CDCl_3$-300 MHz, δ, ppm: 6.85-7.68 (m,21 H, Aromatic), 3.42(s,3H, methyl), 3.88 (dd,2H, C-CH_2-S- thiazol ring), 8.1 (br s, 1H, NH)), 3.64 (1H,s, Ar-OH), 7.22 (s, 3H, OCH_3).

4c. 3-(4-(2-(4-chlorophenyl)-4,5-diphenyl-3λ^2-imidazol-1(2H)-yl)phenyl)-2-(8-fluoro-2-oxo-2H-chromen-3-yl)-2-methylthiazolidin-4-one: Molecular Formula- $C_{40}H_{28}ClFN_3O_3S$, Mol. Wt-685, Yield-55 %, M.Pt-117-118 °C Analysis calcd- C, 70.12; Cl, 5.17; F, 2.77; N, 6.13; S, 4.68 Found- C, 70.08; Cl, 5.14; F, 2.73; N, 6.11; S, 4.64 IR (KBr) υ_{max}/per-cm- 3058 (C-H, str.,arom), 2882 (CH_3, str.), 1769 (C=O, str.), 1673 (C=N), 3370 (N-H), 1178 (C-O-C str.), 762 (C-Cl), 1077 (C-S-C) 1140 (str,C-N-C), 2960 (str, CH_2), 1H NMR- $CDCl_3$-300 MHz, δ, ppm: 6.85-7.63 (m,22 H, Aromatic), 3.40 (s,3H, methyl), 3.85 (dd,2H, C-CH_2-S- thiazol ring), 8.3 (br s, 1H, NH)), 3.64 (1H,s, Ar-OH).

4d. 3-(4-(2-(4-bromophenyl)-4,5-diphenyl-3λ^2-imidazol-1(2H)-yl)phenyl)-2-(8-fluoro-2-oxo-2H-chromen-3-yl)-2-methylthiazolidin-4-one: Molecular Formula- $C_{40}H_{28}BrFN_3O_3S$, Mol. Wt-730, Yield-51 %, M.Pt-106-107 °C Analysis calcd- C, 65.85; Br, 10.95; F, 2.60; N, 5.76; S, 4.39 Found- C, 65.81; Br, 10.92; F, 2.57; N, 5.73; S, 4.35 IR (KBr) υ_{max}/per-cm- 3057 (C-H, str.,arom), 2885 (CH_3, str.), 1755 (C=O, str.), 1670 (C=N), 3378 (N-H), 1165 (C-O-C str.), 730 (C-Br), 1070 (C-S-C) 1145 (str,C-N-C), 2962 (str, CH_2), 1H NMR- $CDCl_3$-300 MHz, δ, ppm: 6.85-7.65 (m,22 H, Aromatic), 3.43 (s,3H, methyl), 3.82 (dd,2H, C-CH_2-S- thiazol ring), 8.5 (br s, 1H, NH)), 3.60 (1H,s, Ar-OH).

4e. 3-(4-(4,5-diphenyl-2-(p-tolyl)-3λ^2-imidazol-1(2H)-yl)phenyl)-2-(8-fluoro-2-oxo-2H-chromen-3-yl)-2-methylthiazolidin-4-one: Molecular Formula- $C_{41}H_{31}FN_3O_3S$, Mol. Wt-665, Yield-53 %, M.Pt-114-115 °C Analysis calcd- C, 74.08; F, 2.86; N, 6.32; S, 4.82 Found- C, 74.05; F, 2.83; N, 6.28; S, 4.81 IR (KBr) υ_{max}/per-cm- 3057 (C-H, str.,arom), 2885 (CH_3, str.), 1755 (C=O, str.), 1670 (C=N), 3378 (N-H), 1165 (C-O-C str.), 730 (C-F), 1070 (C-S-C) 1145 (str,C-N-C), 2962 (str, CH_2), 1H NMR- $CDCl_3$-300 MHz, δ, ppm: 6.85-7.60 (m,22 H, Aromatic), 3.48 (s,6H, methyl), 3.81 (dd,2H, C-CH_2-S- thiazol ring), 8.2 (br s, 1H, NH)), 3.62 (1H,s, Ar-OH).

4f. 2-(8-bromo-2-oxo-2H-chromen-3-yl)-3-(4-(2-(4-hydroxyphenyl)-4,5-diphenyl-3λ^2-imidazol-1(2H)-yl)phenyl)-2-methylthiazolidin-4-one: Molecular Formula- $C_{40}H_{29}BrN_3O_4S$, Mol. Wt-728, Yield-45 %, M.Pt-108-109 °C Analysis calcd- C, 66.03; Br, 10.98 ; N, 5.77; S, 4.41 Found- C, 66.01; Br, 10.96 ; N, 5.74; S, 4.38 IR (KBr) υ_{max}/per-cm- 3060 (C-H, str.,arom), 2880 (CH_3, str.), 1758 (C=O, str.), 1675 (C=N), 3365 (N-H), 1160 (C-O-C str.), 732 (C-Br), 1075 (C-S-C) 1140 (str,C-N-C), 2968 (str, CH_2), 1H NMR- $CDCl_3$-300 MHz, δ, ppm: 6.85-7.66 (m,22 H, Aromatic), 3.46 (s,3H, methyl), 3.81 (dd,2H, C-CH_2-S- thiazol ring), 8.4 (br s, 1H, NH)), 3.64 (1H,s, Ar-OH).

4g. 2-(8-bromo-2-oxo-2H-chromen-3-yl)-3-(4-(2-(4-hydroxy-3-methoxyphenyl)-4,5-diphenyl-3l2-imidazol-1(2H)-yl)phenyl)-2-methylthiazolidin-4-one: Molecular Formula- $C_{41}H_{31}BrN_3O_5S$, Mol. Wt-758, Yield-52 %, M.Pt-103-104 °C Analysis calcd- C, 64.99; Br, 10.55; N, 5.55; S, 4.23 Found- C, 64.96; Br, 10.52; N, 5.51; S, 4.20 IR (KBr) υ_{max}/per-cm- 3062 (C-H, str.,arom), 2885 (CH_3, str.), 1765 (C=O, str.), 1680 (C=N), 3360 (N-H), 1168 (C-O-C str.), 736 (C-Br), 1065 (C-S-C) 1130 (str,C-N-C), 2962 (str, CH_2), 1H NMR- $CDCl_3$-300 MHz, δ, ppm: 6.82-7.61 (m,22 H, Aromatic), 3.45 (s,3H, methyl), 3.82 (dd,2H, C-CH_2-S- thiazol ring), 8.3 (br s, 1H, NH)), 3.61 (1H,s, Ar-OH), 7.15 (s, 3H, OCH_3).

4h. 2-(8-bromo-2-oxo-2H-chromen-3-yl)-3-(4-(2-(4-chlorophenyl)-4,5-diphenyl-3λ^2-imidazol-1(2H)-yl)phenyl)-2-methylthiazolidin-4-one: Molecular Formula- $C_{40}H_{28}BrClN_3O_3S$, Mol. Wt-746, Yield-54 %, M.Pt-95-96 °C Analysis calcd- C, 64.39; Br, 10.71; Cl, 4.75; N, 5.63; S, 4.30 Found- C, 64.35; Br, 10.68; Cl, 4.72; N, 5.60; S, 4.26 IR (KBr) υ_{max}/per-cm- 3065 (C-H, str.,arom), 2884 (CH_3, str.), 1760 (C=O, str.), 1672 (C=N), 3368 (N-H), 1168 (C-O-C str.), 738 (C-Br), 1077 (C-S-C) 1145 (str,C-N-C), 2964 (str, CH_2), 1H NMR- $CDCl_3$-300 MHz, δ, ppm: 6.85-7.63 (m,22 H, Aromatic), 3.48 (s,3H, methyl), 3.83 (dd,2H, C-CH_2-S- thiazol ring), 8.2 (br s, 1H, NH)), 3.61 (1H,s, Ar-OH).

4i. 2-(8-bromo-2-oxo-2H-chromen-3-yl)-3-(4-(4,5-diphenyl-2-(p-tolyl)-3λ^2-imidazol-1(2H)-yl)phenyl)-2-methylthiazolidin-4-one: Molecular Formula-$C_{41}H_{31}BrN_3O_3S$
Mol. Wt-726, Yield-58 %, M.Pt-106-107 °C Analysis calcd- C, 67.86; Br, 11.01; N, 5.79; S, 4.42 Found- C, 67.82; Br, 11.00; N, 5.74; S, 4.37 IR (KBr) υ_{max}/per-cm- 3060 (C-H, str.,arom), 2888 (CH_3, str.), 1762 (C=O, str.), 1670 (C=N), 3366 (N-H), 1160 (C-O-C str.), 732 (C-Br), 1071 (C-S-C) 1140 (str,C-N-C), 2967 (str, CH_2), 1H NMR-

$CDCl_3$-300 MHz, δ, ppm: 6.82-7.65 (m,22 H, Aromatic), 3.34 (s,6H, methyl), 3.81 (dd,2H, C-CH_2-S- thiazol ring), 8.4 (br s, 1H, NH)), 3.63 (1H,s, Ar-OH).

4j. 2-(8-bromo-2-oxo-2H-chromen-3-yl)-2-methyl-3-(4-(2-(4-nitrophenyl)-4,5-diphenyl-3l2-imidazol-1(2H)-yl)phenyl)thiazolidin-4-one: Molecular Formula- $C_{40}H_{28}BrN_4O_5S$, Mol. Wt-757, Yield-42 %, M.Pt-103-104 °C Analysis calcd- C, 63.50; Br, 10.56; N, 7.40; S, 4.24 Found- C, 63.47; Br, 10.52; N, 7.36; S, 4.21 IR (KBr) υ_{max}/per-cm- 3070 (C-H, str.,arom), 2875 (CH_3, str.), 1760 (C=O, str.), 1560 (N=O str.asym-nitro-benzene),1286 (N=O str, sym, nitro-benzene) 1678 (C=N), 3368 (N-H), 1160 (C-O-C str.), 1070 (C-S-C) 1155 (str,C-N-C), 2960(str, CH_2), 1H NMR- $CDCl_3$-300 MHz, δ, ppm: 6.81-7.63 (m,22 H, Aromatic), 3.32 (s,3H, methyl), 3.80 (dd,2H, C-CH_2-S-thiazol ring), 8.1 (br s, 1H, NH)).

4k. 3-(4-(2-(4-fluorophenyl)-4,5-diphenyl-3l2-imidazol-1(2H)-yl)phenyl)-2-(6-methoxy-2-oxo-2H-chromen-3-yl)-2-methylthiazolidin-4-one: Molecular Formula- $C_{41}H_{31}FN_3O_4S$
, Mol. Wt-681, Yield-48 %, M.Pt-119-120 °C Analysis calcd- - C, 72.34; F, 2.79; N, 6.17; S, 4.71 Found C, 72.30; F, 2.75; N, 6.14; S, 4.68 IR (KBr) υ_{max}/per-cm- 3066 (C-H, str.,arom), 2887 (CH_3, str.), 1762 (C=O, str.), 1684 (C=N), 3362 (N-H), 1164 (C-O-C str.), 737 (C-Br), 1062 (C-S-C) 1134 (str,C-N-C), 2964 (str, CH_2), 1H NMR- $CDCl_3$-300 MHz, δ, ppm: 6.82-7.64 (m,22 H, Aromatic), 3.47 (s,3H, methyl), 3.83 (dd,2H, C-CH_2-S- thiazol ring), 8.5 (br s, 1H, NH)), 3.63 (1H,s, Ar-OH), 7.11 (s, 3H, OCH_3).

4l. 3-(4-(2-(4-bromophenyl)-4,5-diphenyl-3λ^2-imidazol-1(2H)-yl)phenyl)-2-(6-methoxy-2-oxo-2H-chromen-3-yl)-2-methylthiazolidin-4-one: Molecular Formula- $C_{41}H_{31}BrN_3O_4S$, Mol. Wt-742, Yield-45 %, M.Pt-112-113 °C Analysis calcd- C, 66.40; Br, 10.77; N, 5.67; S, 4.32 Found- C, 66.35; Br, 10.73; N, 5.65; S, 4.28 IR (KBr) υ_{max}/per-cm- 3064 (C-H, str.,arom), 2881 (CH_3, str.), 1750 (C=O, str.), 1677 (C=N), 3362 (N-H), 1165 (C-O-C str.), 734 (C-Br), 1070 (C-S-C) 1146 (str,C-N-C), 2970 (str, CH_2), 1H NMR- $CDCl_3$-300 MHz, δ, ppm: 6.81-7.62 (m,22 H, Aromatic), 3.34 (s,6H, methyl), 3.85 (dd,2H, C-CH_2-S- thiazol ring), 8.2 (br s, 1H, NH)), 3.61 (1H,s, Ar-OH).

4m. 3-(4-(2-(4-chlorophenyl)-4,5-diphenyl-3λ^2-imidazol-1(2H)-yl)phenyl)-2-(6-methoxy-2-oxo-2H-chromen-3-yl)-2-methylthiazolidin-4-one:Molecular Formula- $C_{41}H_{31}ClN_3O_4S$, Mol. Wt-697, Yield-62 %, M.Pt-117-118 °C Analysis calcd- C, 70.63; Cl, 5.08; N, 6.03; S, 4.60 Found- C, 70.60; Cl, 5.04; N, 6.01; S, 4.56 IR (KBr) υ_{max}/per-cm- 3067 (C-H, str.,arom), 2883 (CH_3, str.), 1754 (C=O, str.), 1679 (C=N), 3360 (N-H), 1160 (C-O-C str.), 736 (C-Br), 1074 (C-S-C) 1140 (str,C-N-C), 2978 (str, CH_2), 1H NMR- $CDCl_3$-300 MHz, δ, ppm: 6.81-7.61 (m,22 H, Aromatic), 3.35 (s,6H, methyl), 3.82 (dd,2H, C-CH_2-S- thiazol ring), 8.4 (br s, 1H, NH)), 3.62 (1H,s, Ar-OH), 7.22 (s, 3H, OCH_3).

4n. 3-(4-(4,5-diphenyl-2-(p-tolyl)-3λ^2-imidazol-1(2H)-yl)phenyl)-2-(6-methoxy-2-oxo-2H-chromen-3-yl)-2-methylthiazolidin-4-one:Molecular Formula- $C_{42}H_{34}N_3O_4S$
Mol. Wt-677, Yield-62 %, M.Pt-108-109 °C Analysis calcd- C, 74.54; N, 6.21; S, 4.74 Found- C, 74.51; N, 6.16; S, 4.70 IR (KBr) υ_{max}/per-cm- 3060 (C-H, str.,arom), 2888 (CH_3, str.), 1762 (C=O, str.), 1670 (C=N), 3366 (N-H), 1160 (C-O-C str.), 732 (C-Br), 1071 (C-S-C) 1140 (str,C-N-C), 2967 (str, CH_2), 1H NMR- $CDCl_3$-300 MHz, δ, ppm: 6.82-7.65 (m,22 H, Aromatic), 3.34 (s,6H, methyl), 3.81 (dd,2H, C-CH_2-S- thiazol ring), 8.4 (br s, 1H, NH)), 3.63 (1H,s, Ar-OH), 7.22 (s, 3H, OCH_3).

IV. ANTIMICROBIAL ACTIVITY

4.1 Determination of MIC

The broth microdilution method was used to determine the MIC of synthesized 2-(substituted-2-oxo-2H-chromen-3-yl)-3-(4-(2-(substituted-phenyl)-4,5-diphenyl-4,5-dihydro-1H-imidazol-1-yl)phenyl)-2-methylthiazolidin-4-one derivatives, as per CLSI guidelines. Twofold serial dilutions of the samples were made directly in a microtiter plate filled with Mueller-Hinton broth. After adding the bacterial inoculum, each well had a final concentration of 5×10^5 CFU/mL. Ciprofloxacin, a common medication, was used as the standard. The plate was incubated at 37°C for 24 hours. After adding resazurin to each well, the microtiter plate was incubated for 30 minutes at 37°C. While the well without bacterial growth remained blue, the wells with bacterial growth became pink. The minimum inhibitory concentration (MIC) was defined as the extract concentration that completely stops bacterial growth. The derivatives to be tested were diluted twofold in a series. The test samples were dissolved in DMSO to obtain a 10 mg/mL stock solution. Sabouraud's broth was prepared for antifungal testing. The solution of the test material (0.2 mL) was added to 1.8 mL of the seeded broth, forming the first dilution. Subsequently, 1.0 mL of this was diluted with a further 1.0 mL of the seeded broth to give the second dilution, and so on until 10-12 such dilutions were obtained. A set

of tubes containing only seeded broth and the standard containing fluconazole were also maintained under identical conditions. The tubes were incubated at 28°C and the MICs of the products (based upon visual appearance of growth) were noted after 48-96 hours post-incubation. The last tube with no apparent growth of the microorganism was taken to represent the MIC of the test compound expressed in µg/mL.

TABLE 1
ANTIMICROBIAL ACTIVITY OF 2-(SUBSTITUTED-2-OXO-2H-CHROMEN-3-YL)-3-(4-(2-(SUBSTITUTED-PHENYL)-4,5-DIPHENYL-4,5-DIHYDRO-1H-IMIDAZOL-1-YL)PHENYL)-2-METHYLTHIAZOLIDIN-4-ONE DERIVATIVES (4A-N): MIC (µg/mL)

Compd	R^1 (Coumarin substituent)	R^2 (Imidazole substituent)	*B. subtilis*	*S. aureus*	*E. coli*	*C. albicans*
4a	8-Bromo	4-Hydroxyphenyl	100	50	25	25
4b	8-Bromo	4-Hydroxy-3-methoxyphenyl	100	50	100	100
4c	8-Bromo	4-Chlorophenyl	50	25	50	100
4d	8-Bromo	4-Methylphenyl	100	25	50	25
4e	8-Bromo	4-Nitrophenyl	25	100	50	25
4f	8-Fluoro	4-Hydroxyphenyl	100	100	100	100
4g	8-Fluoro	4-Hydroxy-3-methoxyphenyl	100	50	25	12.5
4h	8-Fluoro	4-Chlorophenyl	50	25	25	100
4i	8-Fluoro	4-Bromophenyl	25	12.5	25	6.25
4j	8-Fluoro	4-Methylphenyl	25	6.25	100	100
4k	6-Methoxy	4-Fluorophenyl	12.5	100	100	100
4l	6-Methoxy	4-Bromophenyl	100	100	50	100
4m	6-Methoxy	4-Chlorophenyl	50	50	50	100
4n	6-Methoxy	4-Methylphenyl	25	50	25	50
Standards		**Ciprofloxacin**	**50**	**100**	**50**	—
		Fluconazole	—	—	—	**50**

Note: MIC values are presented as µg/mL. All tests were performed in duplicate; variation was within ±1 dilution.

V. RESULTS AND DISCUSSION

Fourteen methylthiazolidin-4-one derivatives were synthesized, out of which five derivatives of bromo-3-acetyl coumarin, five derivatives of fluoro-3-acetyl coumarin, and four derivatives of methoxy-3-acetyl coumarin were evaluated for their antimicrobial activity against Gram-positive bacteria (*B. subtilis*, *S. aureus*), Gram-negative bacteria (*E. coli*), and fungus (*C. albicans*).

When the synthesized derivatives were tested against *Candida albicans*, only four derivatives exhibited good activity. Derivative **4i** (R^1 = 8-F, R^2 = 4-Br) showed superior activity with an MIC of 6.25 µg/mL. Derivative **4g** (R^1 = 8-F, R^2 = 4-OH,3-OCH_3) showed excellent activity with an MIC of 12.5 µg/mL. Derivatives **4a** (R^1 = 8-Br, R^2 = 4-OH) and **4d** (R^1 = 8-Br, R^2 = 4-CH_3) showed MIC values of 25 µg/mL. The remaining derivatives reflected only satisfactory activity.

Against *B. subtilis*, out of fourteen derivatives, only five were active. Derivatives **4e** (R^1 = 8-Br, R^2 = 4-NO_2), **4i** (R^1 = 8-F, R^2 = 4-Br), **4j** (R^1 = 8-F, R^2 = 4-CH_3), and **4n** (R^1 = 6-OCH_3, R^2 = 4-CH_3) displayed MIC values of 25 µg/mL. Derivative **4k** (R^1 = 6-OCH_3, R^2 = 4-F) showed excellent activity with an MIC of 12.5 µg/mL. The remaining nine derivatives demonstrated moderate activity.

Against *S. aureus*, five synthesized derivatives were found to be highly active. Derivatives **4c** (R^1 = 8-Br, R^2 = 4-Cl) and **4d** (R^1 = 8-Br, R^2 = 4-CH_3) showed MIC values of 25 µg/mL. Derivatives **4h** (R^1 = 8-F, R^2 = 4-Cl), **4i** (R^1 = 8-F, R^2 = 4-Br), and **4j** (R^1 = 8-F, R^2 = 4-CH_3) showed MIC values of 25, 12.5, and 6.25 µg/mL, respectively. Derivative **4j** was the most lethal against *S. aureus*, achieving an MIC of 6.25 µg/mL.

Against *E. coli*, derivatives **4a** (R^1 = 8-Br, R^2 = 4-OH), **4g** (R^1 = 8-F, R^2 = 4-OH,3-OCH_3), **4h** (R^1 = 8-F, R^2 = 4-Cl), **4i** (R^1 = 8-F, R^2 = 4-Br), and **4n** (R^1 = 6-OCH_3, R^2 = 4-CH_3) demonstrated good activity with MIC values of 25 µg/mL. The other ten derivatives displayed moderate activity.

Among all active compounds, one common factor is that either R^1 or R^2 or both contain electronegative substituents (halogens, nitro, methoxy), which appears to be the main cause of enhanced activity. It is clear that the presence of electronegative groups is very vital in eliciting the desired biological effect. Therefore, it is suggested here that the synthesis of more such compounds containing additional electronegative groups (chloro, fluoro, bromo, OCH_3, etc.) is required for further ascertaining the potentials of such derivatives.

TABLE 2
MOST ACTIVE COMPOUNDS

Compound	Most Significant Activity	MIC (µg/mL)
4i	*S. aureus* and *C. albicans*	12.5 and 6.25
4j	*S. aureus*	6.25
4k	*B. subtilis*	12.5
4g	*C. albicans*	12.5

VI. CONCLUSION

All synthesized derivatives (4a-n) of 2-(substituted-2-oxo-2H-chromen-3-yl)-3-(4-(2-(substituted-phenyl)-4,5-diphenyl-4,5-dihydro-1H-imidazol-1-yl)phenyl)-2-methylthiazolidin-4-one were evaluated for antimicrobial activity. Compounds **4i**, **4j**, and **4k** demonstrated the most promising antimicrobial activity. Exclusively, compound **4i** displayed broad-spectrum antibacterial and antifungal potency, suggesting that incorporation of halogen substituents, especially bromine and fluorine, may create potentially more active compounds. These findings indicate that the synthesized thiazolidinone-coumarin-imidazole hybrids may serve as potential lead molecules for the development of new antimicrobial agents.

ACKNOWLEDGEMENT

We are thankful to the Faculty of Chemical Sciences, Shri Ramswaroop Memorial University, Barabanki, for providing laboratory facilities. We are also thankful to BBAU Central University, Lucknow, for providing instrumentation and biological activity testing facilities.

CONFLICT OF INTEREST

The authors declare no conflict of interest.

REFERENCES

[1] Abbas, S. Y., Abd El-Aziz, M. M., Awad, S. M., & Mohamed, M. S. (2023). Synthesis and evaluation of antipyrine derivatives bearing a thiazole moiety as antibacterial and antifungal agents. *Synthetic Communications*, *53*(21), 1812–1822. https://doi.org/10.1080/00397911.2023.2248306

[2] Al-Ghamdi, H. A., Almughem, F. A., Alshabibi, M. A., Alsharif, A. A., & Almaghrabi, M. (2024). Synthesis and biological evaluation of novel imidazole derivatives as antimicrobial agents. *Biomolecules*, *14*(9), Article 1198. https://doi.org/10.3390/biom14091198

[3] Asif, M. (2017). A mini review: Biological significances of nitrogen hetero atom containing heterocyclic compounds. *International Journal of Bioorganic Chemistry*, *2*(4), 146–152.

[4] Aslam, K., Khosa, M. K., Jahan, N., & Nosheen, S. (2010). Synthesis and application of coumarin. *Pakistan Journal of Pharmaceutical Sciences*, *23*(4), 449–454.

[5] Bhatnagar, A., & Pemawat, G. (2023). An overview on synthetic routes of anti-inflammatory active scaffolds including thiazole and thiazolidine cores. *Phosphorus, Sulfur, and Silicon and the Related Elements*, *198*(7), 554–565. https://doi.org/10.1080/10426507.2023.2189253

[6] Gandioso, A., Palau, M., Bresolí-Obach, R., Galán, A., Rovira, A., & Nonell, S. (2018). High photostability in nonconventional coumarins with far-red/NIR emission through azetidinyl substitution. *The Journal of Organic Chemistry*, *83*(19), 11519–11531.

[7] Gupta, K., Sirbaiya, A. K., Kumar, V., & Rahman, M. A. (2022). Current perspective of synthesis of medicinally relevant benzothiazole based molecules: Potential for antimicrobial and anti-inflammatory activities. *Mini-Reviews in Medicinal Chemistry*, *22*(14), 1895–1935. https://doi.org/10.2174/1389557522666220217101805

[8] Gurav, S. S., Jadhav, S. R., Mali, S. N., Pawar, S. D., & Shinde, A. A. (2023). An efficient one-pot multicomponent Amberlite IR120(H) catalyzed microwave-assisted synthesis of 1,2,4,5-tetrasubstituted-1H-imidazoles: Plausible mechanism and antibacterial evaluation. *Synthetic Communications*, *53*(22), 2029–2040. https://doi.org/10.1080/00397911.2023.2267131

[9] Hemeda, L. R., El Hassab, M. A., Abdelgawad, M. A., Elsayed, Z. M., & Al-Warhi, T. (2023). Discovery of pyrimidine-tethered benzothiazole derivatives as novel anti-tubercular agents towards multi- and extensively drug resistant *Mycobacterium tuberculosis*. *Journal of Enzyme Inhibition and Medicinal Chemistry*, *38*(1), Article 2250575.

https://doi.org/10.1080/14756366.2023.2250575

[10] Henary, M., Kananda, C., Rotolo, L., Savino, B., & Owens, E. A. (2020). Benefits and applications of microwave-assisted synthesis of nitrogen containing heterocycles in medicinal chemistry. *RSC Advances*, *10*, 14170–14197.

[11] Heravi, M., Sadjadi, S., Oskooie, H., Hekmat Shoar, R., & Bamoharram, F. F. (2008). The synthesis of coumarin-3-carboxylic acids and 3-acetyl-coumarin derivatives using heteropolyacids as heterogeneous and recyclable catalysts. *Catalysis Communications*, *9*(4), 470–474. https://doi.org/10.1016/j.catcom.2007.07.005

[12] Huang, W., Lu, Y., Yao, N., Li, Y., & Wang, S. (2024). A novel collapse strategy of zeolitic imidazole frameworks shell triggered by p-benzoquinone for the fluorescence monitoring α-glucosidase activity and screening natural anti-diabetes drug. *Sensors and Actuators B: Chemical*, *404*, Article 135234. https://doi.org/10.1016/j.snb.2023.135234

[13] Jun, J., Yang, S., Lee, J., Park, H., & Kim, H. (2023). Discovery of novel imidazole chemotypes as isoform-selective JNK3 inhibitors for the treatment of Alzheimer's disease. *European Journal of Medicinal Chemistry*, *245*, Article 114894.
https://doi.org/10.1016/j.ejmech.2022.114894

[14] Mahesh, K. P., Swapnil, S. M., & Manikrao, M. S. (2001). Coumarin synthesis via Pechmann condensation in Lewis acidic chloroaluminate ionic liquid. *Tetrahedron Letters*, *42*(52), 9285–9287.

[15] Matos, M. J., Santana, L., Uriarte, E., & Borges, F. (2015). Coumarins—An important class of phytochemicals. In *Phytochemicals: Isolation, characterisation and role in human health*. InTech. https://doi.org/10.5772/59982

[16] Nagaraju, P., Reddy, P. N., Padmaja, P., & Ugale, V. G. (2021). Microwave-assisted synthesis of thiazole/benzothiazole fused pyranopyrimidine derivatives and evaluation of their biological activity. *Letters in Organic Chemistry*, *18*(1), 49–57.
https://doi.org/10.2174/1570178617999200517130138

[17] Nandurkar, Y., Shinde, A., Bhoye, M. R., Pawar, S., & Pissurlenkar, R. R. S. (2023). Synthesis and biological screening of new 2-(5-aryl-1-phenyl-1H-pyrazol-3-yl)-4-aryl thiazole derivatives as potential antimicrobial agents. *ACS Omega*, *8*(9), 8743–8754. https://doi.org/10.1021/acsomega.2c08137

[18] O'Kennedy, R., & Thornes, R. D. (1997). *Coumarins: Biology, applications and mode of action*. Wiley.

[19] Olofson, A., Yakushijin, K., & Horne, D. A. (1998). Synthesis of marine sponge alkaloids oroidin, clathrodin and dispacamides: Preparation and transformation of 2-amino-4,5-dialkoxy-4,5-dihydroimidazolines from 2-aminoimidazoles. *The Journal of Organic Chemistry*, *63*(4), 1248–1253. https://doi.org/10.1021/jo9718298

[20] Othman, I. M. M., Alamshany, Z. M., Tashkandi, N. Y., Gad-Elkareem, M. A. M., & El-Naggar, M. (2022). Synthesis and biological evaluation of new derivatives of thieno-thiazole and dihydrothiazolo-thiazole scaffolds integrated with a pyrazoline nucleus as anticancer and multi-targeting kinase inhibitors. *RSC Advances*, *12*, 561–577. https://doi.org/10.1039/D1RA08055E

[21] Pawar, S., Karan, R., Rawal, R. K., & Gupta, P. K. (2024). Antimicrobial and antifungal evaluation of some novel thiazolidin-4-one scaffold bearing compounds. *Letters in Applied NanoBioScience*, *13*(4), Article 166. https://doi.org/10.33263/LIANBS134.166

[22] Pawar, S., Kumar, K., Gupta, M. K., & Rawal, R. K. (2021). Synthetic and medicinal perspective of fused-thiazoles as anticancer agents. *Anti-Cancer Agents in Medicinal Chemistry*, *21*(11), 1379–1402. https://doi.org/10.2174/1871520620666200728133017

[23] Petrou, A., Geronikaki, A., Kartsev, V., & Eleftheriou, P. (2023). *N*-Derivatives of (Z)-methyl 3-(4-oxo-2-thioxothiazolidin-5-ylidene)methyl)-1H-indole-2-carboxylates as antimicrobial agents—*In silico* and *in vitro* evaluation. *Pharmaceuticals*, *16*(1), Article 131. https://doi.org/10.3390/ph16010131

[24] Raghu, M. S., Pradeep Kumar, C. B., Yogesh Kumar, K., Prashanth, M. K., & Nagaraju, G. (2022). Design, synthesis and molecular docking studies of imidazole and benzimidazole linked ethionamide derivatives as inhibitors of InhA and antituberculosis agents. *Bioorganic & Medicinal Chemistry Letters*, *60*, Article 128604. https://doi.org/10.1016/j.bmcl.2022.128604

[25] Richaud, A., Barba-Behrens, N., & Méndez, F. (2011). Chemical reactivity of the imidazole: A semblance of pyridine and pyrrole? *Organic Letters*, *13*(5), 972–975. https://doi.org/10.1021/ol103011h

[26] Saliyeva, L., Holota, S., Grozav, A., & Lesyk, R. (2022). Synthesis and evaluation of antimicrobial and anti-inflammatory activity of 6-aryliden-2-methyl-2,3-dihydroimidazo[2,1-b][1,3]thiazoles. *Biointerface Research in Applied Chemistry*, *12*(1), 292–303. https://doi.org/10.33263/BRIAC121.292303

[27] Sattigeri, V. J., Soni, A., Singhal, S., & Pandya, S. (2005). Synthesis and antimicrobial activity of novel thiazolidinones. *Arkivoc*, *2005*(ii), 46–59.

[28] Shaabani, A., Ghadari, R., Rahmati, A., & Rezayan, A. H. (2009). Coumarin synthesis via Knoevenagel condensation reaction in 1,1,3,3-N,N,N′,N′-tetramethylguanidinium trifluoroacetate ionic liquid. *Journal of the Iranian Chemical Society*, *6*, 710–714. https://doi.org/10.1007/BF03246160

[29] Solo, P., Arockia Doss, M., & Prasanna, D. (2022). Designing and docking studies of imidazole-based drugs as potential inhibitors of myeloperoxidase mediated inflammation and oxidative stress. *Biocatalysis and Agricultural Biotechnology*, *43*, Article 102421. https://doi.org/10.1016/j.bcab.2022.102421

[30] Srivastava, K., Prakash, R., Singh, R. B., & Srivastava, A. (2023). Synthesis, characterization and antibacterial evaluation of novel β-lactam and thiazolidin-4-one derivatives having thiadiazinyl ring. *Bulletin of Pharmaceutical Sciences, Assiut University*, *46*(1), 203–216.

[31] Srivastava, K., Srivastava, A., Tiwari, R. P., & Singh, R. (2023). A facile synthesis, characterization and biological evaluation of novel spiro-thiazolidinone and quinazolinone-thiazolidine derivatives. *Indian Journal of Chemistry*, *62B*(7), 770–779.
https://doi.org/10.56042/ijc.v62i7.3830

[32] Tratrat, C., Petrou, A., Geronikaki, A., Kartsev, V., & Eleftheriou, P. (2022). Thiazolidin-4-ones as potential antimicrobial agents: Experimental and *in silico* evaluation. *Molecules*, *27*(6), Article 1930. https://doi.org/10.3390/molecules27061930

[33] Tsay, S. C., Hwu, J. R., Singha, R., & Shieh, S. (2013). Coumarins hinged directly on benzimidazoles and their ribofuranosides to inhibit hepatitis C virus. *European Journal of Medicinal Chemistry*, *63*, 290–293. https://doi.org/10.1016/j.ejmech.2013.02.008

[34] Verma, A., Joshi, S., & Singh, D. (2013). Imidazole: Having versatile biological activities. *Journal of Chemistry*, *2013*, Article 329412. https://doi.org/10.1155/2013/329412

[35] Wan, Y., Hur, W., Cho, C. Y., Liu, Y., & Cravatt, B. F. (2004). Synthesis and target identification of hymenialdisine analogs. *Chemistry & Biology*, *11*(2), 247–259. https://doi.org/10.1016/j.chembiol.2004.01.015

[36] Wang, J., Long, S., Liu, Z., & Zhang, Q. (2023). Structure-activity relationship studies of thiazole agents with potential anti methicillin-resistance *Staphylococcus aureus* activity. *Process Biochemistry*, *132*, 13–29. https://doi.org/10.1016/j.procbio.2023.06.013

[37] Zhao, C., Qiao, X., Yi, Z., Guan, Q., & Li, W. (2020). Active centre and reactivity descriptor of a green single component imidazole catalyst for acetylene hydrochlorination. *Physical Chemistry Chemical Physics*, *22*, 2849–2857. https://doi.org/10.1039/C9CP06005G.

International Journal of Engineering Research & Science (IJOER)
ISSN: [2395-6992]
[Vol-12, Issue-5, May- 2026]
Website: www.ijoer.com
Journal DOI: 10.25125/engineering-journal

Synthesis, Characterization and Antimicrobial Activities of Novel Heterocycles 8-(3-chloro-2-(2-hydroxy-3-nitrophenyl)-4-oxoazetidin-1-yl)-4-methylpyrano[2,3-b]phenothiazin-2(11H)-one and 8-(4-(2-(3-bromo-2-hydroxyphenyl)-3-chloro-4-oxoazetidin-1-yl)phenyl)-4-methylpyrano[2,3-b]phenothiazin-2(11H)-one Derivatives

Ayushi Sahu[1]; Dolly Kumari[2*]; Rishi Kumar Vishnoi[3]; Krishna Srivastava[4*]

[1,2,4]Faculty of Chemical Sciences, Shri Ramswaroop Memorial University, Barabanki, U.P., 225003, India.
[3]Department of Chemistry, Amity University, Lucknow Campus, Lucknow-226012, India
*Corresponding Author

Received: 06 May 2026/ Revised: 18 May 2026/ Accepted: 25 May 2026/ Published: 31-05-2026

Abstract— *A convenient protocol for the synthesis of oxoazetidinyl-phenothiazinone derivatives has been initiated with the reaction of resorcinol and acetoacetic ester to yield coumarin. In another reaction, Schiff bases were prepared by the condensation of substituted-salicylaldehyde with benzidine and substituted-salicylaldehyde with benzene-1,4-diamine, subsequently cyclized with chloroacetyl chloride to form β-lactam-amine. Further, the amine reacted with coumarin in the presence of $ZnCl_2$ to form prefinal derivatives. The interaction of biphenylyl-azetidin-2-one or phenyl-azetidin-2-one with sulphur powder and iodine afforded the final phenothiazinone derivatives. The structures of the synthesized derivatives were determined by elemental analysis, UV-visible, FT-IR, ^{1}H-NMR, and mass spectra. The obtained derivatives exhibited excellent to moderate antimicrobial activity.*

Keywords— Phenothiazinone, acetoacetic ester, coumarin, benzidine, benzene-1,4-diamine, salicylaldehyde.

I. INTRODUCTION

Phenothiazines are of major significance in heterocyclic chemistry. They comprise a tricyclic system which is constituted by two benzene rings and an internal ring containing sulphur and nitrogen [1]. They were primarily employed as dyes in the textile industry during the 19th century, but with new evidence they have been shown to possess excellent antipsychotic properties and are employed in the treatment of schizophrenia and other conditions. Their medicinal importance started becoming evident during the 20th century when methylene blue, a common dye, was found to be an efficient antimalarial and antiseptic drug [1-4]. Phenothiazine's general molecular formula is $C_{12}H_9NS$ and contains N and S atoms in the center. The presence of such configuration renders them highly reactive and amenable for further alterations [5]. The presence of these moieties impacts their electronic nature, lipophilicity, and planar geometry in such a way that it facilitates their binding/attachment to numerous biological target sites [6]. The central nitrogen atom is a significant target site for numerous acetylations, alkylations, or condensations with aldehydes, which inadvertently affects binding affinity to dopamine D_2 receptors, histamine H_1 receptors, and various other CNS-related targets and is pivotal in the development of antipsychotics, antihistamines, and antiemetics [7-10]. Besides this, it has great significance in blood-brain barrier penetration, thereby improving its utilization in medication of CNS-related diseases [11].

β-Lactams comprise a four-membered cyclic amide where the nitrogen atom is attached to the β-carbon relative to the carbonyl group and hence are also known as azetidinones [12-15]. These are quite famous among medicinal chemists. These molecules are among the base scaffolds of many useful antibiotics such as penicillins, cephalosporins, carumonam,

aztreonam, thienamycin, and nocardicins [16-19]. The first β-lactam was synthesized in 1907 by Staudinger, but it was only after 1943 that research on these molecules gained momentum as more of the compounds showed intense biological activities such as antibacterial, antifungal, antiviral, anticancer, anti-inflammatory, anticonvulsant, hypotensive, hypnotic, antitubercular, and vital against combating many serious diseases [20-23].

Since the discovery of the coumarin molecule in 1820, it has gained an exclusive place in heterocyclic medicinal chemistry. It is basically 2H-1-benzopyran-2-one [24-27]. It displays a wide spectrum of biological activities such as platelet aggregation inhibition, anticonvulsant, antiviral, anticoagulant, antifungal, anti-HIV, anticarcinogenic, antihistaminic, and antitubercular [28-30]. Coumarin synthesis can be achieved through various chemical reactions such as Pechmann, Perkin, Knoevenagel, and Reformatsky. Among all these, Pechmann condensation is the most frequent method adopted for the synthesis of coumarin [31].

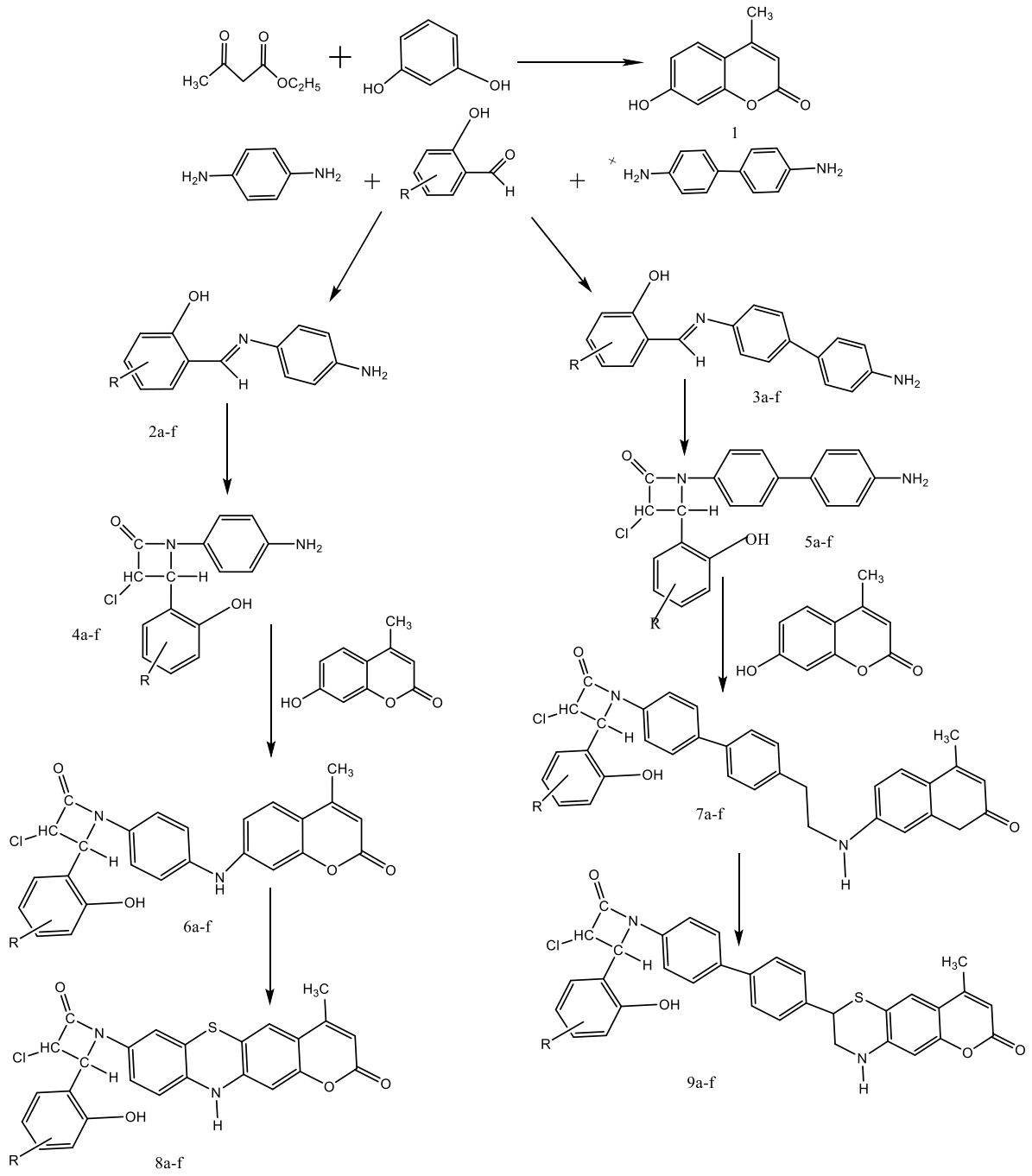

SCHEME-1

II. EXPERIMENTAL METHODOLOGY

The melting points of all synthesized β-lactam-phenothiazinone derivatives were examined by the open capillary method [32-34]. The purity and progress were determined by using precoated TLC plates (Merck, 60F-254) in an iodine chamber to develop the slides, with eluent hexane/ethyl acetate (5:2) [35-38]. The ^{1}H NMR spectra were recorded in $CDCl_3$ and DMSO on a Bruker NMR spectrophotometer at 400 MHz. Tetramethylsilane was taken as the internal standard and chemical shift values (δ) are given in parts per million (ppm). A Jasco FT-IR-470 spectrophotometer (KBr) with diffuse reflectance method was used for recording FT-IR spectra. MS-JEOL SX102 mass spectroscopy was used for recording mass spectra using Argon/Xenon (6 kV, 10 mA) as the FAB gas and m-nitrobenzyl alcohol as the matrix. UV spectra of the samples were carried out on a double beam UV-visible spectrophotometer.

2.1 Synthesis of 7-hydroxy-4-methyl-2H-chromen-2-one (1):

Equimolar quantities of resorcinol (0.1 mole) and ethyl acetoacetate with 70% sulphuric acid (30 mL) were heated carefully for 0.5 hour. The resulting dark green solution was cooled and poured over crushed ice. The crude product was filtered off, washed repeatedly with water, and dried at 100°C. The anhydrous coumarin thus obtained was insoluble in methanol but was recrystallized with difficulty from benzene as pale yellow needle-like crystals. Chemical Formula: $C_{10}H_8O_3$; Molecular Weight: 176; Yield 75%; m.p. 185-186°C.

2.1.1 Synthesis of (E)-2-(((4-aminophenyl)imino)methyl)-6-substituted-phenol (2a-f)

Equimolar amounts of reactants (substituted-salicylaldehyde and benzene-1,4-diamine) were taken in 25 mL ethanol and refluxed on a heating mantle for 5-6 hours with 1 mL glacial acetic acid. After being rinsed with cold water, the resulting products were recrystallized in ethanol. The characterization values are given below:

2a. (E)-2-(((4-Aminophenyl)imino)methyl)-6-fluorophenol:

Chemical Formula: $C_{13}H_{11}FN_2O$; Molecular Weight: 230; Yield: 58%; m.p. 102°C; Elemental Analysis calcd: C, 67.82; F, 8.25; N, 12.17. Found: C, 67.80; F, 8.21; N, 12.12. IR (KBr) ν_max (cm^{-1}): 740 (C-F), 3341 (N-H), 3034 (CH, aromatic), 1422 (C=N), 1572 (C=C skeletal).

2b. (E)-2-(((4-Aminophenyl)imino)methyl)-6-bromophenol:

Chemical Formula: $C_{13}H_{11}BrN_2O$; Molecular Weight: 291; Yield: 52%; m.p. 86°C; Elemental Analysis calcd: C, 53.63; Br, 27.44; N, 9.62. Found: C, 53.60; Br, 27.40; N, 9.58. IR (KBr) ν_max (cm^{-1}): 810 (C-Br), 3338 (N-H), 3036 (CH, aromatic), 1424 (C=N), 1570 (C=C skeletal).

2c. (E)-2-(((4-Aminophenyl)imino)methyl)-6-chlorophenol:

Chemical Formula: $C_{13}H_{11}ClN_2O$; Molecular Weight: 247; Yield: 57%; m.p. 93-94°C; Elemental Analysis calcd: C, 63.29; Cl, 14.37; N, 11.36. Found: C, 63.26; Cl, 14.34; N, 11.32. IR (KBr) ν_max (cm^{-1}): 690 (C-Cl), 3330 (N-H), 3040 (CH, aromatic), 1430 (C=N), 1575 (C=C skeletal).

2d. (E)-2-(((4-Aminophenyl)imino)methyl)-6-nitrophenol:

Chemical Formula: $C_{13}H_{11}N_3O_3$; Molecular Weight: 257; Yield: 61%; m.p. 105-106°C; Elemental Analysis calcd: C, 60.70; N, 16.33. Found: C, 60.66; N, 16.30. IR (KBr) ν_max (cm^{-1}): 1560 (N=O str. asym, nitro-benzene), 1285 (N=O str., sym, nitro-benzene), 3340 (N-H), 3038 (CH, aromatic), 1430 (C=N), 1578 (C=C skeletal).

2e. (E)-2-(((4-Aminophenyl)imino)methyl)-4-methoxyphenol:

Chemical Formula: $C_{14}H_{14}N_2O_2$; Molecular Weight: 242; Yield: 65%; m.p. 98-99°C; Elemental Analysis calcd: C, 69.41; N, 11.56. Found: C, 69.38; N, 11.53. IR (KBr) ν_max (cm^{-1}): 1177 (O-C, OCH_3), 3330 (N-H), 3040 (CH, aromatic), 1425 (C=N), 1575 (C=C skeletal).

2f. (E)-2-(((4-Aminophenyl)imino)methyl)-4-methylphenol:

Chemical Formula: $C_{14}H_{14}N_2O$; Molecular Weight: 226; Yield: 70%; m.p. 108-109°C; Elemental Analysis calcd: C, 74.31; N, 12.38. Found: C, 74.28; N, 12.35. IR (KBr) ν_max (cm^{-1}): 2975 (p-CH_3-phenyl), 3335 (N-H), 3038 (CH, aromatic), 1432 (C=N), 1575 (C=C skeletal).

2.1.2 Synthesis of (E)-2-(((4'-amino-[1,1'-biphenyl]-4-yl)imino)methyl)-substituted-phenol (3a-f)

Equimolar concentrations of reactants (substituted-salicylaldehyde and benzidine) were taken in 25 mL ethanol and refluxed on a heating mantle for 5-6 hours with 1 mL glacial acetic acid. After being rinsed with cold water, the resulting products were recrystallized in ethanol. The characterization values are given below:

3a. (E)-2-(((4'-Amino-[1,1'-biphenyl]-4-yl)imino)methyl)-6-fluorophenol:

Chemical Formula: $C_{19}H_{15}FN_2O$; Molecular Weight: 306; Yield: 62%; m.p. 103-104°C; Elemental Analysis calcd: C, 74.50; F, 6.20; N, 9.14. Found: C, 74.47; F, 6.15; N, 9.12. IR (KBr) ν_max (cm^{-1}): 680 (C-F), 3355 (N-H), 3044 (CH, aromatic), 1433 (C=N), 1580 (C=C skeletal).

3b. (E)-2-(((4'-Amino-[1,1'-biphenyl]-4-yl)imino)methyl)-6-bromophenol:

Chemical Formula: $C_{19}H_{15}BrN_2O$; Molecular Weight: 367; Yield: 54%; m.p. 95-96°C; Elemental Analysis calcd: C, 62.14; Br, 21.76; N, 7.63. Found: C, 62.11; Br, 21.72; N, 7.60. IR (KBr) ν_max (cm^{-1}): 710 (C-Br), 3355 (N-H), 3054 (CH, aromatic), 1440 (C=N), 1570 (C=C skeletal).

3c. (E)-2-(((4'-Amino-[1,1'-biphenyl]-4-yl)imino)methyl)-6-chlorophenol:

Chemical Formula: $C_{19}H_{15}ClN_2O$; Molecular Weight: 323; Yield: 63%; m.p. 87-88°C; Elemental Analysis calcd: C, 70.70; Cl, 10.98; N, 8.68. Found: C, 70.67; Cl, 10.95; N, 8.64. IR (KBr) ν_max (cm^{-1}): 680 (C-Cl), 3335 (N-H), 3038 (CH, aromatic), 1432 (C=N), 1572 (C=C skeletal).

3d. (E)-2-(((4'-Amino-[1,1'-biphenyl]-4-yl)imino)methyl)-6-nitrophenol:

Chemical Formula: $C_{19}H_{15}N_3O_3$; Molecular Weight: 333; Yield: 48%; m.p. 105-106°C; Elemental Analysis calcd: C, 68.46; N, 12.61. Found: C, 68.41; N, 12.58. IR (KBr) ν_max (cm^{-1}): 1555 (N=O str. asym, nitro-benzene), 1272 (N=O str., sym, nitro-benzene), 3345 (N-H), 3031 (CH, aromatic), 1436 (C=N), 1580 (C=C skeletal).

3e. (E)-2-(((4'-Amino-[1,1'-biphenyl]-4-yl)imino)methyl)-4-methoxyphenol:

Chemical Formula: $C_{20}H_{18}N_2O_2$; Molecular Weight: 318; Yield: 55%; m.p. 103-104°C; Elemental Analysis calcd: C, 75.45; N, 8.80. Found: C, 75.43; N, 8.77. IR (KBr) ν_max (cm^{-1}): 1170 (O-C, OCH_3), 3335 (N-H), 3042 (CH, aromatic), 1430 (C=N), 1584 (C=C skeletal).

3f. (E)-2-(((4'-Amino-[1,1'-biphenyl]-4-yl)imino)methyl)-4-methylphenol:

Chemical Formula: $C_{20}H_{18}N_2O$; Molecular Weight: 302; Yield: 75%; m.p. 85-86°C; Elemental Analysis calcd: C, 79.44; N, 9.26. Found: C, 79.40; N, 9.23. IR (KBr) ν_max (cm^{-1}): 2970 (p-CH_3-phenyl), 3332 (N-H), 3040 (CH, aromatic), 1436 (C=N), 1572 (C=C skeletal).

2.1.3 Synthesis of 1-(4-aminophenyl)-3-chloro-4-(substituted-2-hydroxyphenyl)-azetidin-2-one (4a-f)

Equimolar quantities (0.02 mole) of (E)-2-(((4-aminophenyl)imino)methyl)-6-substituted-phenol (2a-f) in 25 mL dioxane were added to chloroacetyl chloride and triethylamine at 0°C with continuous stirring and kept for three hours at room temperature, then refluxed on a heating mantle for 8-9 hours. After cooling, the reaction mixture was poured into crushed ice and recrystallized in ethanol. The characterization data are as follows:

4a. 1-(4-Aminophenyl)-3-chloro-4-(3-fluoro-2-hydroxyphenyl)-azetidin-2-one:

Chemical Formula: $C_{15}H_{12}ClFN_2O_2$; Molecular Weight: 307; Yield: 70%; m.p. 88-89°C; Elemental Analysis calcd: C, 58.74; Cl, 11.56; F, 6.19; N, 9.13. Found: C, 58.72; Cl, 11.52; F, 6.15; N, 9.11. IR (KBr) ν_max (cm^{-1}): 3072 (CH, aromatic), 1020 (C-N), 1650 (Amide), 970 (C-Cl), 1585 (C=C), 3375 (phenol). ^1H NMR ($CDCl_3$, 400 MHz, δ, ppm): 6.82-7.89 (m, 8H, aromatic), 4.81 (s, 1H, -OH), 6.8 (s, 1H, NH_2, D_2O exchangeable), 4.12 (d, 1H, J=4.8 Hz, β-lactam C3-H), 4.98 (d, 1H, J=4.8 Hz, β-lactam C4-H). *[Note: β-lactam protons appear as doublets, not singlets]*

4b. 1-(4-Aminophenyl)-4-(3-bromo-2-hydroxyphenyl)-3-chloroazetidin-2-one:

Chemical Formula: $C_{15}H_{12}BrClN_2O_2$; Molecular Weight: 368; Yield: 60%; m.p. 101-102°C; Elemental Analysis calcd: C, 49.01; Br, 21.74; Cl, 9.64; N, 7.62. Found: C, 48.98; Br, 21.70; Cl, 9.60; N, 7.59. IR (KBr) ν_max (cm^{-1}):

3068 (CH, aromatic), 1025 (C-N), 1652 (Amide), 977 (C-Cl), 1580 (C=C), 3378 (phenol). ^{1}H NMR ($CDCl_3$, 400 MHz, δ, ppm): 6.80-7.83 (m, 8H, aromatic), 4.75 (s, 1H, -OH), 6.6 (s, 1H, NH_2, D_2O exchangeable), 4.10 (d, 1H, J=4.8 Hz, β-lactam C3-H), 4.95 (d, 1H, J=4.8 Hz, β-lactam C4-H).

4c. 1-(4-aminophenyl)-3-chloro-4-(3-chloro-2-hydroxyphenyl)-azetidin-2-one:

Chemical Formula: : $C_{15}H_{12}Cl_2N_2O_2$; Molecular Weight: 323; Yield: 60%; m.p. 101-102°C; Elemental Analysis: C, 55.75; Cl, 21.94; N, 8.67 found: C, 55.71; Cl, 21.90; N, 8.63; Infrared-ν_{max} per cm-KBr: 3055(CH, Aromatic), 1030(C-N), 1652(Amide), 975(C-Cl),1588(C=C), 3376(phenol), 1H NMR: 6.84-7.87(m, 8H, aromatic), 2.4(s, 1H, lactam ring), 4.76(s, 1H, -OH), 6.4(singlet, 1H, NH_2, D_2O exchangeable).

4d. 1-(4-aminophenyl)-3-chloro-4-(2-hydroxy-3-nitrophenyl)-azetidin-2-one:

Chemical Formula: $C_{15}H_{12}ClN_3O_4$; Molecular Weight: 334; Yield: 55%; m.p. 115-116°C; Elemental Analysis: C, 53.99; Cl, 10.62; N, 12.59 found: C, 53.96; Cl, 10.58; N, 12.57; Infrared-ν_{max} per cm-KBr: 3051(CH, Aromatic), 1034(C-N), 1658(Amide), 978(C-Cl),1588(C=C), 3360(phenol); 1H NMR: 6.87-7.83(m, 8H, aromatic), 2.6(s, 1H, lactam ring), 4.73(s, 1H, -OH), 6.5(singlet, 1H, NH_2, D_2O exchangeable).

4e. 1-(4-aminophenyl)-3-chloro-4-(2-hydroxy-5-methoxyphenyl)-azetidin-2-one:

Chemical Formula: $C_{16}H_{15}ClN_2O_3$; Molecular Weight: 319; Yield: 62%; m.p. 106-107°C; Elemental Analysis: C, 60.29; Cl, 11.12; N, 8.79 found: C, 60.27; Cl, 11.09; N, 8.76; Infrared-ν_{max} per cm-KBr: 3058(CH, Aromatic), 1035(C-N), 1652(Amide), 980(C-Cl),1590(C=C), 3371(phenol); 1H NMR: 6.81-7.89(m, 8H, aromatic), 2.1(s, 1H, lactam ring), 4.72(s, 1H, -OH), 6.8(singlet, 1H, NH_2, D_2O exchangeable).

4f. 1-(4-aminophenyl)-3-chloro-4-(2-hydroxy-5-methylphenyl)-azetidin-2-one:

Chemical Formula: $C_{16}H_{15}ClN_2O_2$; Molecular Weight: 303; Yield: 55%; m.p. 104-105°C; Elemental Analysis: C, 63.48; Cl, 11.71; N, 9.25 found: C, 63.44; Cl, 11.68; N, 9.20; Infrared-ν_{max} per cm-KBr: 3060(CH, Aromatic), 1025(C-N), 1650(Amide), 980(C-Cl),1584(C=C), 3371(phenol); 1H NMR: 6.88-7.74(m, 8H, aromatic), 2.1(s, 1H, lactam ring), 4.73(s, 1H, -OH), 6.2(singlet, 1H, NH_2, D_2O exchangeable).

2.1.4 Synthesis of 1-(4'-amino-[1,1'-biphenyl]-4-yl)-3-chloro-4-(substituted-2-hydroxyphenyl)-azetidin-2-one (5a-f)

Equimolar quantities (0.02 mole) of (E)-2-(((4'-amino-[1,1'-biphenyl]-4-yl)imino)methyl)-substituted-phenol (3a-f) in 25 mL dioxane were added to chloroacetyl chloride and triethylamine at 0°C with continuous stirring and kept for three hours at room temperature, then refluxed on a heating mantle for 13-14 hours. After cooling, the reaction mixture was poured into crushed ice and recrystallized in ethanol. Characterization data are as follows:

5a. 1-(4'-Amino-[1,1'-biphenyl]-4-yl)-3-chloro-4-(4-fluoro-2-hydroxyphenyl)-azetidin-2-one:

Chemical Formula: $C_{21}H_{16}ClFN_2O_2$; Molecular Weight: 383; Yield: 61%; m.p. 106-107°C; Elemental Analysis calcd: C, 64.59; Cl, 7.63; F, 4.09; N, 6.03. Found: C, 64.55; Cl, 7.60; F, 4.06; N, 6.01. IR (KBr) ν_max (cm^{-1}): 3065 (CH, aromatic), 1035 (C-N), 1650 (Amide), 870 (C-Cl), 1580 (C=C), 3382 (phenol). ^{1}H NMR ($CDCl_3$, 400 MHz, δ, ppm): 6.81-7.66 (m, 12H, aromatic), 4.85 (s, 1H, -OH), 3.11 (s, 3H, methyl), 4.15 (d, 1H, J=4.8 Hz, β-lactam C3-H), 5.01 (d, 1H, J=4.8 Hz, β-lactam C4-H).

5b. 1-(4'-amino-[1,1'-biphenyl]-4-yl)-4-(4-bromo-2-hydroxyphenyl)-3-chloroazetidin-2-one:

Chemical Formula: $C_{21}H_{16}BrClN_2O_2$; Molecular Weight: 444; Yield: 55%; m.p. 93-94°C; Elemental Analysis: C, 56.84; Br, 18.01; Cl, 7.99; N, 6.31 found: C, 56.80; Br, 18.00; Cl, 7.99; N, 6.29; Infrared-ν_{max} per cm-KBr: 3062(CH, Aromatic), 1038(C-N), 1652 (Amide), 874(C-Cl), 1585(C=C), 2825(-CH_3,) 3386(phenol); 1H NMR: 6.81-7.63(m, 11H, aromatic), 2.5(s, 1H, lactam ring), 4.82(s, 1H, -OH), 3.12(s, 3H, methyl).

5c. 1-(4'-amino-[1,1'-biphenyl]-4-yl)-3-chloro-4-(3-chloro-2-hydroxyphenyl)-azetidin-2-one:

Chemical Formula: $C_{21}H_{16}Cl_2N_2O_2$; Molecular Weight: 399; Yield: 60%; m.p. 103-104°C; Elemental Analysis: C, 63.17; Cl, 17.76; N, 7.02 found: C, 63.15; Cl, 17.72; N, 7.01; Infrared-ν_{max} per cm-KBr: 3060(CH, Aromatic), 1032(C-N), 1651(Amide), 872(C-Cl), 1588 (C=C), 2820 (-CH_3,) 3387(phenol); 1H NMR: 6.82-7.64(m, 11H, aromatic), 2.4(s, 1H, lactam ring), 4.81(s, 1H, -OH), 3.14(s, 3H, methyl).

5d. 1-(4'-amino-[1,1'-biphenyl]-4-yl)-3-chloro-4-(2-hydroxy-3-nitrophenyl)-azetidin-2-one:

Chemical Formula: $C_{21}H_{16}ClN_3O_4$; Molecular Weight: 410; Yield: 68%; m.p. 87-88°C; Elemental Analysis: C, 61.55; Cl, 8.65; N, 10.25 found: C, 61.50; Cl, 8.62; N, 10.21; Infrared-ν_{max} per cm-KBr: 3070(CH, Aromatic),1028(C-N),1650(Amide), 875(C-Cl),1584 (C=C), 2830(-CH_3,) 3380(phenol); 1H NMR: 6.80-7.67(m, 11H, aromatic), 2.7(s, 1H, lactam ring), 4.83(s, 1H, -OH), 3.10(s, 3H, methyl).

5e. 1-(4'-amino-[1,1'-biphenyl]-4-yl)-3-chloro-4-(2-hydroxy-5-methoxyphenyl)-azetidin-2-one:

Chemical Formula: $C_{22}H_{19}ClN_2O_3$; Molecular Weight: 395; Yield: 58%; m.p. 118-119°C; Elemental Analysis: C, 66.92; Cl, 8.98; N, 7.09 found: C, 66.91; Cl, 8.94; N, 7.06; Infrared-ν_{max} per cm-KBr: 3060(CH, Aromatic), 1030(C-N), 1654(Amide), 872(C-Cl), 1585(C=C), 2830(-CH_3), 3375(phenol); 1H NMR: 6.86-7.62(m, 11H, aromatic), 2.1(s, 1H, lactam ring), 4.83(s, 1H, -OH), 3.09 (s, 3H, methyl).

5f. 1-(4'-amino-[1,1'-biphenyl]-4-yl)-3-chloro-4-(2-hydroxy-5-methylphenyl)-azetidin-2-one:

Chemical Formula: $C_{22}H_{19}ClN_2O_2$; Molecular Weight: 379; Yield: 55%; m.p. 91-92°C; Elemental Analysis: C, 69.75; Cl, 9.36; N, 7.39 found: C, 69.71; Cl, 9.33; N, 7.35; Infrared-ν_{max} per cm-KBr: 3060(CH, Aromatic), 1032(C-N), 1650(Amide), 874(C-Cl), 1582(C=C), 2820(-CH_3), 3386(phenol); 1H NMR: 6.81-7.62(m, 11H, aromatic), 2.1(s, 1H, lactam ring), 4.82(s, 1H, -OH), 3.13(s, 3H, methyl).

2.1.5 Synthesis of 3-chloro-4-(substituted-2-hydroxyphenyl)-1-(4-((4-methyl-2-oxo-2H-chromen-7-yl)amino)phenyl)-azetidin-2-one (6a-f)

Equimolar quantities (0.02 mole) of 1-(4-aminophenyl)-3-chloro-4-(substituted-2-hydroxyphenyl)-azetidin-2-one (4a-f) and 7-hydroxy-4-methyl-2H-chromen-2-one (1) were taken in 25 mL ethanol and refluxed on a heating mantle in the presence of anhydrous $ZnCl_2$ for 9-10 hours. The reaction mixture was cooled and filtered, washed with cold water, and recrystallized from ethanol. Characterization data are as follows:

6a. 3-Chloro-4-(3-fluoro-2-hydroxyphenyl)-1-(4-((4-methyl-2-oxo-2H-chromen-7-yl)amino)phenyl)-azetidin-2-one:
Chemical Formula: $C_{25}H_{18}ClFN_2O_4$; Molecular Weight: 465; Yield: 61%; m.p. 116-117°C; Elemental Analysis calcd: C, 64.59; Cl, 7.63; F, 4.09; N, 6.03. Found: C, 64.55; Cl, 7.60; F, 4.06; N, 6.01. IR (KBr) ν_max (cm^{-1}): 3065 (CH, aromatic), 1035 (C-N), 1650 (Amide), 870 (C-Cl), 1580 (C=C), 2825 (-CH_3), 3382 (phenol). ^{1}H NMR ($CDCl_3$, 400 MHz, δ, ppm): 6.72-7.76 (m, 11H, aromatic), 4.82 (s, 1H, -OH), 3.01 (s, 3H, methyl), 4.18 (d, 1H, J=4.8 Hz, β-lactam C3-H), 4.96 (d, 1H, J=4.8 Hz, β-lactam C4-H).

6b. 4-(3-Bromo-2-hydroxyphenyl)-3-chloro-1-(4-((4-methyl-2-oxo-2H-chromen-7-yl)amino)phenyl)-azetidin-2-one:
Chemical Formula: $C_{25}H_{18}BrClN_2O_4$; Molecular Weight: 526; Yield: 66%; m.p. 88-89°C; Elemental Analysis: C, 57.11; Br, 15.20; Cl, 6.74; N, 5.33 found: C, 57.07; Br, 15.15; Cl, 6.72; N, 5.30; Infrared-ν_{max} per cm-KBr: 3060(CH, Aromatic), 1032(C-N), 1650(Amide), 865(C-Cl), 1580(C=C), 2832(-CH_3,) 3378(phenol); 1H NMR: 6.88-7.78(m, 11H, aromatic), 2.5(s, 1H, lactam ring), 4.79(s, 1H, -OH), 3.03(s, 3H, methyl).

6c. 3-Chloro-4-(3-chloro-2-hydroxyphenyl)-1-(4-((4-methyl-2-oxo-2H-chromen-7-yl)amino)phenyl)-azetidin-2-one:
Chemical Formula: $C_{25}H_{18}Cl_2N_2O_4$; Molecular Weight: 481; Yield: 60%; m.p. 103-104°C; Elemental Analysis: C, 62.38; Cl, 14.73; N, 5.82 found: C, 62.35; Cl, 14.70; N, 5.78; Infrared-ν_{max} per cm-KBr: 3068(CH, Aromatic), 1025(C-N), 1656(Amide), 860(C-Cl), 1584 (C=C), 2835(-CH_3), 3375(phenol); 1H NMR: 6.82-7.75(m, 11H, aromatic), 2.4(s, 1H, lactam ring), 4.76(s, 1H, -OH), 3.06(s, 3H, methyl).

6d. 3-Chloro-4-(2-hydroxy-3-nitrophenyl)-1-(4-((4-methyl-2-oxo-2H-chromen-7-yl)amino)phenyl)-azetidin-2-one:
Chemical Formula: $C_{25}H_{18}ClN_3O_6$; Molecular Weight: 492; Yield: 55%; m.p. 106-107°C; Elemental Analysis: C, 61.05; Cl, 7.21; N, 8.54; O, 19.52 found: C, 61.02; Cl, 7.17; N, 8.50; O, 19.52; Infrared-ν_{max} per cm-KBr: 3062(CH, Aromatic), 1025(C-N), 1655(Amide), 860(C-Cl), 1584 (C=C), 2830(-CH_3), 3372(phenol); 1H NMR: 6.84-7.71(m, 11H, aromatic), 2.3 (s, 1H, lactam ring), 4.77(s, 1H, -OH), 3.05(s, 3H, methyl).

6e. 3-Chloro-4-(2-hydroxy-5-methoxyphenyl)-1-(4-((4-methyl-2-oxo-2H-chromen-7-yl)amino)phenyl)-azetidin-2-one:

Chemical Formula: $C_{26}H_{21}ClN_2O_5$; Molecular Weight: 477; Yield: 66%; m.p. 88-89°C; Elemental Analysis: C, 65.48; Cl, 7.43; N, 5.87 found: C, 65.48; Cl, 7.43; N, 5.87; Infrared-ν_{max} per cm-KBr: 3055(CH, Aromatic), 1040(C-N), 1645(Amide), 870(C-Cl), 1582(C=C), 2835(-CH_3), 3382(phenol); 1H NMR: 6.87-7.79(m, 11H, aromatic), 2.6(s, 1H, lactam ring), 4.74(s, 1H, -OH), 3.07(s, 3H, methyl).

6f. 3-Chloro-4-(2-hydroxy-5-methylphenyl)-1-(4-((4-methyl-2-oxo-2H-chromen-7-yl)amino)phenyl)-azetidin-2-one:

Chemical Formula: $C_{26}H_{21}ClN_2O_4$; Molecular Weight: 461; Yield: 58%; m.p. 101-102°C; Elemental Analysis: C, 67.75; Cl, 7.69; N, 6.08 found: C, 67.71; Cl, 7.67; N, 6.04; Infrared-ν_{max} per cm-KBr: 3062(CH, Aromatic), 1034(C-N), 1655(Amide), 861(C-Cl), 1585(C=C), 2835(-CH_3), 3370(phenol); 1H NMR: 6.83-7.71(m, 11H, aromatic), 2.2(s, 1H, lactam ring), 4.75 (s, 1H, -OH), 3.04(s, 3H, methyl).

2.1.6 Synthesis of 3-chloro-4-(substituted-2-hydroxyphenyl)-1-(4'-((4-methyl-2-oxo-2H-chromen-7-yl)amino)-[1,1'-biphenyl]-4-yl)-azetidin-2-one (7a-f)

Equimolar quantities (0.02 mole) of 1-(4'-amino-[1,1'-biphenyl]-4-yl)-3-chloro-4-(substituted-2-hydroxyphenyl)-azetidin-2-one (5a-f) and 7-hydroxy-4-methyl-2H-chromen-2-one (1) were taken in 25 mL ethanol and refluxed on a heating mantle in the presence of anhydrous $ZnCl_2$ for 7-8 hours. The reaction mixture was cooled and filtered, washed with cold water, and recrystallized with ethanol. Characterization data are as follows:

7a. 3-Chloro-4-(3-fluoro-2-hydroxyphenyl)-1-(4'-((4-methyl-2-oxo-2H-chromen-7-yl)amino)-[1,1'-biphenyl]-4-yl)-azetidin-2-one:

Chemical Formula: $C_{31}H_{22}ClFN_2O_4$; Molecular Weight: 541; Yield: 54%; m.p. 82-83°C; Elemental Analysis: C, 68.83; Cl, 6.55; F, 3.51; N, 5.18 found: C, 68.80; Cl, 6.51; F, 3.48; N, 5.14; Infrared-ν_{max} per cm-KBr: 3050(CH, Aromatic), 1025(C-N), 1645(Amide), 840(C-Cl), 1580(C=C), 2830(-CH_3,) 3370(N-H stretch), 3375(phenol) 1H NMR: 6.91-7.78 (m, 15H, aromatic), 2.4(s, 1H, lactam ring), 4.78 (s, 1H, -OH), 3.06(s, 3H, methyl), 4.11(1H, C-NH-C).

7b. 3-Chloro-4-(3-bromo-2-hydroxyphenyl)-1-(4'-((4-methyl-2-oxo-2H-chromen-7-yl)amino)-[1,1'-biphenyl]-4-yl)-azetidin-2-one:

Chemical Formula: $C_{31}H_{22}BrClN_2O_4$; Molecular Weight: 602; Yield: 50%; m.p. 122-123°C; Elemental Analysis: C, 61.86; Br, 13.28; Cl, 5.89; N, 4.65 found: C, 61.81; Br, 13.24; Cl, 5.86; N, 4.62; Infrared-ν_{max} per cm-KBr: 3051(CH, Aromatic), 1022(C-N), 1640 (Amide), 842(C-Cl), 1580(C=C), 2836 (-CH_3), 3370(N-H stretch), 3375(phenol); 1H NMR: 6.80-7.63 (m, 15H, aromatic), 2.4(s, 1H, lactam ring), 4.71(s, 1H, -OH), 3.04(s, 3H, methyl), 4.12(1H, C-NH-C).

7c. 3-Chloro-4-(3-chloro-2-hydroxyphenyl)-1-(4'-((4-methyl-2-oxo-2H-chromen-7-yl)amino)-[1,1'-biphenyl]-4-yl)-azetidin-2-one:

Chemical Formula: $C_{31}H_{22}Cl_2N_2O_4$; Molecular Weight: 557; Yield: 48%; m.p. 82-83°C; Elemental Analysis: C, 66.80; Cl, 12.72; N, 5.03 found: C, 66.76; Cl, 12.70; N, 5.01; Infrared-ν_{max} per cm-KBr: 3052(CH, Aromatic), 1028(C-N), 1648(Amide), 844(C-Cl), 1585 (C=C), 2832(-CH_3), 3376(N-H stretch), 3378(phenol); 1H NMR: 6.81-7.67 (m, 15H, aromatic), 2.5(s, 1H, lactam ring), 4.74(s, 1H, -OH), 3.02(s, 3H, methyl), 4.10(1H, C-NH-C).

7d. 3-Chloro-4-(2-hydroxy-3-nitrophenyl)-1-(4'-((4-methyl-2-oxo-2H-chromen-7-yl)amino)-[1,1'-biphenyl]-4-yl)-azetidin-2-one:

Chemical Formula: $C_{31}H_{22}ClN_3O_6$; Molecular Weight: 568; Yield: 62%; m.p. 105-106°C; Elemental Analysis: C, 65.56; Cl, 6.24; N, 7.40 found: C, 65.51; Cl, 6.20; N, 7.36; Infrared-ν_{max} per cm-KBr: 3056(CH, Aromatic), 1035(C-N), 1642(Amide), 845(C-Cl), 1588(C=C), 2836(-CH_3), 3378(N-H stretch), 3372(phenol); 1H NMR: 6.83-7.62(m, 15H, aromatic), 2.2 (s, 1H, lactam ring), 4.72(s, 1H, -OH), 3.03(s, 3H, methyl), 4.14(1H, C-NH-C).

7e. 3-Chloro-4-(2-hydroxy-5-methoxyphenyl)-1-(4'-((4-methyl-2-oxo-2H-chromen-7-yl)amino)-[1,1'-biphenyl]-4-yl)-azetidin-2-one:

Chemical Formula: $C_{32}H_{25}ClN_2O_5$; Molecular Weight: 553; Yield: 70%; m.p. 115-116°C; Elemental Analysis: C, 69.50; Cl, 6.41; N, 5.07 found: C, 69.46; Cl, 6.38; N, 5.03; Infrared-ν_{max} per cm-KBr: 3060(CH, Aromatic), 1030(C-

N), 1645(Amide), 840(C-Cl), 1580(C=C), 2832(-CH_3), 3375(N-H stretch), 3375(phenol); 1H NMR: 6.81-7.60(m, 15H, aromatic), 2.1 (s, 1H, lactam ring), 4.70(s, 1H, -OH), 3.04(s, 3H, methyl), 4.12(1H, C-NH-C).

7f. 3-Chloro-4-(2-hydroxy-5-methylphenyl)-1-(4'-((4-methyl-2-oxo-2H-chromen-7-yl)amino)-[1,1'-biphenyl]-4-yl)-azetidin-2-one:

Chemical Formula: $C_{32}H_{25}ClN_2O_4$; Molecular Weight: 537; Yield: 65%; m.p. 118-119°C; Elemental Analysis: C, 71.57; Cl, 6.60; N, 5.22 found: C, 71.52; Cl, 6.55; N, 5.20; Infrared-ν_{max} per cm-KBr: 3055(CH, Aromatic), 1035(C-N), 1648(Amide), 830(C-Cl), 1590(C=C), 2840(-CH_3), 3380(N-H stretch), 3365(phenol); 1H NMR: 6.83-7.68(m, 15H, aromatic), 2.1 (s, 1H, lactam ring), 4.73(s, 1H, -OH), 3.04(s, 3H, methyl), 4.19(1H, C-NH-C).

2.1.7 Synthesis of 8-(3-chloro-2-(substituted-2-hydroxyphenyl)-4-oxoazetidin-1-yl)-4-methylpyrano[2,3-b]phenothiazin-2(11H)-one (8a-f)

Equimolar quantities (0.02 mole) of 3-chloro-4-(substituted-2-hydroxyphenyl)-1-(4-((4-methyl-2-oxo-2H-chromen-7-yl)amino)phenyl)-azetidin-2-one (6a-f) and 1 g sulphur powder were heated at 160-170°C for 3-4 hours in the presence of 2 g iodine. The reaction mixture was cooled at room temperature and treated with dilute HCl to remove unreacted amine, then washed repeatedly with water. Characterization data are as follows:

8a. 8-(3-Chloro-2-(3-fluoro-2-hydroxyphenyl)-4-oxoazetidin-1-yl)-4-methylpyrano[2,3-b]phenothiazin-2(11H)-one:

Chemical Formula: $C_{25}H_{16}ClFN_2O_4S$; Molecular Weight: 495; Yield: 52%; m.p. 106-107°C; Elemental Analysis calcd: C, 60.67; Cl, 7.16; F, 3.84; N, 5.66; S, 6.48. Found: C, 60.64; Cl, 7.12; F, 3.80; N, 5.64; S, 6.46. IR (KBr) ν_max (cm^{-1}): 3055 (CH, aromatic), 1035 (C-N), 1648 (Amide), 675 (C-S-C, phenothiazine ring), 840 (C-Cl), 1580 (C=C), 2845 (-CH_3), 3385 (N-H), 3360 (phenol). ^{1}H NMR ($CDCl_3$, 400 MHz, δ, ppm): 6.81-7.71 (m, 8H, aromatic), 4.71 (s, 1H, -OH), 3.07 (s, 3H, methyl), 4.2 (s, 1H, NH), 4.20 (d, 1H, J=4.8 Hz, β-lactam C3-H), 4.98 (d, 1H, J=4.8 Hz, β-lactam C4-H).

8b. 8-(2-(3-Bromo-2-hydroxyphenyl)-3-chloro-4-oxoazetidin-1-yl)-4-methylpyrano[2,3-b]phenothiazin-2(11H)-one:

Chemical Formula: $C_{25}H_{16}BrClN_2O_4S$; Molecular Weight: 556; Yield: 60%; m.p. 97-98°C; Elemental Analysis: C, 54.02; Br, 14.38; Cl, 6.38; N, 5.04; S, 5.77 found: C, 54.01; Br, 14.33; Cl, 6.35; N, 5.01; S, 5.74; Infrared-ν_{max} per cm-KBr: 3060(CH, Aromatic), 1030(C-N), 1640 (Amide), 678(C-S-C phenothiazine ring), 848(C-Cl), 1590(C=C), 2840(-CH_3), 3382(N-H stretch), 3366(phenol); 1H NMR: 6.81-7.74(m, 8H, aromatic), 2.8(s, 1H, lactam ring), 4.74 (s, 1H, -OH), 3.08(s, 3H, methyl), 4.4(1H, C-NH-C).

8c. 8-(3-Chloro-2-(3-chloro-2-hydroxyphenyl)-4-oxoazetidin-1-yl)-4-methylpyrano[2,3-b]phenothiazin-2(11H)-one:

Chemical Formula: $C_{25}H_{16}Cl_2N_2O_4S$; Molecular Weight: 511; Yield: 64%; m.p. 106-107°C; Elemental Analysis: C, 58.72; Cl, 13.86; N, 5.48; S, 6.27 found: C, 58.68; Cl, 13.82; N, 5.43; S, 6.25; Infrared-ν_{max} per cm-KBr: 3060(CH, Aromatic), 1030(C-N), 1655(Amide), 667(C-S-C phenothiazine ring), 850(C-Cl), 1590(C=C), 2846(-CH), 3387(N-H stretch), 3362 (phenol); 1H NMR: 6.83-7.70(m, 8H, aromatic), 2.5(s, 1H, lactam ring), 4.74(s, 1H, -OH), 3.05(s, 3H, methyl), 4.3(1H, C-NH-C).

8d. 8-(3-Chloro-2-(2-hydroxy-3-nitrophenyl)-4-oxoazetidin-1-yl)-4-methylpyrano[2,3-b]phenothiazin-2(11H)-one:

Chemical Formula: $C_{25}H_{16}ClN_3O_6S$; Molecular Weight: 522; Yield: 52%; m.p. 106-107°C; Elemental Analysis: C, 57.53; Cl, 6.79; N, 8.05; S, 6.14 found: C, 57.50; Cl, 6.76; N, 8.02; S, 6.10; Infrared-ν_{max} per cm-KBr: 3055(CH, Aromatic), 1030(C-N), 1655(Amide), 680(C-S-C phenothiazine ring), 820(C-Cl), 1570(C=C), 2850(-CH_3), 3380(N-H stretch), 3365 (phenol); 1H NMR: 6.80-7.72(m, 8H, aromatic), 2.5(s, 1H, lactam ring), 4.74(s, 1H, -OH), 3.02(s, 3H, methyl), 4.3(1H, C-NH-C).

8e. 8-(3-Chloro-2-(2-hydroxy-5-methoxyphenyl)-4-oxoazetidin-1-yl)-4-methylpyrano[2,3-b]phenothiazin-2(11H)-one:

Chemical Formula: $C_{26}H_{19}ClN_2O_5S$; Molecular Weight: 507; Yield: 55%; m.p. 102-103°C; Elemental Analysis: C, 61.60; Cl, 6.99; N, 5.53; S, 6.32 found: C, 61.57; Cl, 6.96; N, 5.50; S, 6.27; Infrared-ν_{max} per cm-KBr: 3070(CH, Aromatic), 1040(C-N), 1645(Amide), 672(C-S-C phenothiazine ring), 846(C-Cl), 1584(C=C), 2840(-CH_3),

3388(N-H stretch), 3363 (phenol); 1H NMR: 6.81-7.74(m, 8H, aromatic), 2.5(s, 1H, lactam ring), 4.70(s, 1H, -OH), 3.05(s, 3H, methyl), 4.4(1H, C-NH-C).

8f. 8-(3-Chloro-2-(2-hydroxy-5-methylphenyl)-4-oxoazetidin-1-yl)-4-methylpyrano[2,3-b]phenothiazin-2(11H)-one:

Chemical Formula: $C_{26}H_{19}ClN_2O_4S$; Molecular Weight: 491; Yield: 68%; m.p. 104-105°C; Elemental Analysis: C, 63.61; Cl, 7.22; N, 5.71; S, 6.53 found: C, 63.57; Cl, 7.18; N, 5.67; S, 6.51; Infrared-ν_{max} per cm-KBr: 3060(CH, Aromatic), 1040(C-N), 1641(Amide), 670(C-S-C phenothiazine ring), 844(C-Cl), 1583(C=C), 2848(-CH_3), 3380(N-H stretch), 3365 (phenol); 1H NMR: 6.82-7.76(m, 8H, aromatic), 2.4(s, 1H, lactam ring), 4.72(s, 1H, -OH), 3.05(s, 3H, methyl), 4.6(1H, C-NH-C).

2.1.8 Synthesis of 8-(4-(3-chloro-2-(substituted-2-hydroxyphenyl)-4-oxoazetidin-1-yl)phenyl)-4-methylpyrano[2,3-b]phenothiazin-2(11H)-one (9a-f)

Equimolar quantities (0.02 mole) of 3-chloro-4-(substituted-2-hydroxyphenyl)-1-(4'-((4-methyl-2-oxo-2H-chromen-7-yl)amino)-[1,1'-biphenyl]-4-yl)-azetidin-2-one (7a-f) and 1 g sulphur powder were heated at 160-170°C for 2-3 hours in the presence of 2 g iodine. The reaction mixture was cooled at room temperature, treated with dilute HCl to remove unreacted amine, and washed repeatedly with water. Characterization data are as follows:

9a. 8-(4-(3-Chloro-2-(3-fluoro-2-hydroxyphenyl)-4-oxoazetidin-1-yl)phenyl)-4-methylpyrano[2,3-b]phenothiazin-2(11H)-one:

Chemical Formula: $C_{31}H_{20}ClFN_2O_4S$; Molecular Weight: 571; Yield: 45%; m.p. 121-122°C; Elemental Analysis calcd: C, 65.21; Cl, 6.21; F, 3.33; N, 4.91; S, 5.61. Found: C, 65.17; Cl, 6.18; F, 3.29; N, 4.87; S, 5.58. IR (KBr) ν_max (cm^{-1}): 3070 (CH, aromatic), 1020 (C-N), 1641 (Amide), 640 (C-S-C, phenothiazine ring), 780 (C-Cl), 1590 (C=C), 2860 (-CH_3), 3370 (N-H), 3380 (phenol). ^{1}H NMR ($CDCl_3$, 400 MHz, δ, ppm): 6.76-7.72 (m, 13H, aromatic), 4.70 (s, 1H, -OH), 3.08 (s, 3H, methyl), 4.4 (s, 1H, NH), 4.22 (d, 1H, J=4.8 Hz, β-lactam C3-H), 5.00 (d, 1H, J=4.8 Hz, β-lactam C4-H).

9b. 8-(4-(2-(3-Bromo-2-hydroxyphenyl)-3-chloro-4-oxoazetidin-1-yl)phenyl)-4-methylpyrano[2,3-b]phenothiazin-2(11H)-one:

Chemical Formula: $C_{31}H_{20}BrClN_2O_4S$; Molecular Weight: 632; Yield: 65%; m.p. 119-120°C; Elemental Analysis: C, 58.92; Br, 12.64; Cl, 5.61; N, 4.43; S, 5.07 found: C, 58.88; Br, 12.60; Cl, 5.58; N, 4.40; S, 5.05; Infrared-ν_{max} per cm-KBr: 3072(CH, Aromatic), 1025(C-N), 1640(Amide), 648(C-S-C phenothiazine ring), 785(C-Cl), 1592(C=C), 2865(-CH_3), 3377 (N-H stretch), 3382(phenol); 1H NMR: 6.81-7.74(m, 13H, aromatic), 2.7(s, 1H, lactam ring), 4.74 (s, 1H, -OH), 3.05(s, 3H, methyl), 4.6(1H, C-NH-C).

9c. 8-(4-(3-Chloro-2-(3-chloro-2-hydroxyphenyl)-4-oxoazetidin-1-yl)phenyl)-4-methylpyrano[2,3-b]phenothiazin-2(11H)-one:

Chemical Formula: $C_{31}H_{20}Cl_2N_2O_4S$; Molecular Weight: 587; Yield: 55%; m.p. 107-108°C; Elemental Analysis: C, 63.38; Cl, 12.07; N, 4.77; S, 5.46 found: C, 63.34; Cl, 12.05; N, 4.74; S, 5.42; Infrared-ν_{max} per cm-KBr: 3075(CH, Aromatic), 1024(C-N), 1645(Amide), 642(C-S-C phenothiazine ring), 781(C-Cl), 1595(C=C), 2862(-CH_3), 3373(N-H stretch), 3385 (phenol); 1H NMR: 6.76-7.74(m, 13H, aromatic), 2.3(s, 1H, lactam ring), 4.71 (s, 1H, -OH), 3.04(s, 3H, methyl), 4.2(1H, C-NH-C).

9d. 8-(4-(3-Chloro-2-(2-hydroxy-3-nitrophenyl)-4-oxoazetidin-1-yl)phenyl)-4-methylpyrano[2,3-b]phenothiazin-2(11H)-one:

Chemical Formula: $C_{31}H_{20}ClN_3O_6S$; Molecular Weight: 598; Yield: 60%; m.p. 116-117°C; Elemental Analysis: C, 62.26; Cl, 5.93; N, 7.03; S, 5.36 found: C, 62.22; Cl, 5.90; N, 7.01; S, 5.32; Infrared-ν_{max} per cm-KBr: 3070(CH, Aromatic), 1020(C-N), 1641(Amide), 640(C-S-C phenothiazine ring), 780(C-Cl), 1590(C=C), 2860(-CH_3), 3370(N-H stretch), 3380 (phenol); 1H NMR: 6.76-7.72(m, 13H, aromatic), 2.5(s, 1H, lactam ring), 4.70(s, 1H, -OH), 3.08(s, 3H, methyl), 4.4(1H, C-NH-C).

9e. 8-(4-(3-Chloro-2-(2-hydroxy-5-methoxyphenyl)-4-oxoazetidin-1-yl)phenyl)-4-methylpyrano[2,3-b]phenothiazin-2(11H)-one:

Chemical Formula: $C_{32}H_{23}ClN_2O_5S$; Molecular Weight: 583; Yield: 58%; m.p. 103-104°C; Elemental Analysis: C, 65.92; Cl, 6.08; N, 4.80; S, 5.50 found: C, 65.88; Cl, 6.05; N, 4.77; S, 5.46; Infrared-ν_{max} per cm-KBr: 3065(CH,

Aromatic), 1030(C-N), 1645(Amide), 642(C-S-C phenothiazine ring), 784(C-Cl), 1585(C=C), 2862(-CH_3), 3375(N-H stretch), 3385 (phenol); 1H NMR: 6.76-7.73(m, 13H, aromatic), 2.3(s, 1H, lactam ring), 4.73(s, 1H, -OH), 3.06(s, 3H, methyl), 4.7(1H, C-NH-C).

9f. 8-(4-(3-Chloro-2-(2-hydroxy-5-methylphenyl)-4-oxoazetidin-1-yl)phenyl)-4-methylpyrano[2,3-b]phenothiazin-2(11H)-one:
Chemical Formula: $C_{32}H_{23}ClN_2O_4S$; Molecular Weight: 567; Yield: 68%; m.p. 114-115°C; Elemental Analysis: C, 67.78; Cl, 6.25; N, 4.94; S, 5.65 found: C, 67.74; Cl, 6.22; N, 4.91; S, 5.63;Infrared-ν_{max} per cm-KBr: 3076(CH, Aromatic), 1024(C-N), 1645(Amide), 642(C-S-C phenothiazine ring), 785(C-Cl), 1590(C=C), 2866(-CH_3), 3365(N-H stretch), 3378 (phenol); 1H NMR: 6.76-7.75(m, 13H, aromatic), 2.8(s, 1H, lactam ring), 4.73(s, 1H, -OH), 3.05(s, 3H, methyl), 4.6(1H, C-NH-C).

2.1.9 Determination of Minimum Inhibitory Concentration (MIC)

The broth microdilution method was used to determine the MIC of synthesized novel heterocycles 8-(3-chloro-2-(2-hydroxy-3-nitrophenyl)-4-oxoazetidin-1-yl)-4-methylpyrano[2,3-b]phenothiazin-2(11H)-one and 8-(4-(2-(3-bromo-2-hydroxyphenyl)-3-chloro-4-oxoazetidin-1-yl)phenyl)-4-methylpyrano[2,3-b]phenothiazin-2(11H)-one derivatives. A twofold serial dilution method of the sample compounds was made immediately in a microtiter plate filled with Mueller-Hinton broth in order to prepare different concentrations. All wells contained a final concentration of 5×10^5 CFU/mL following the addition of the bacterial inoculum. The standard drug used was chloramphenicol. The plate was incubated at 37°C for 24 hours. Each well in the microtiter plate was filled with resazurin, and it was then incubated at 37°C for 30 minutes. The wells with bacterial growth changed color. The extract concentration that completely stopped the bacterial growth is known as the minimum inhibitory concentration (MIC). The test compound's MIC is given in µg/mL. Table 1 represents the MIC values of 8a-f and 9a-f compounds for various Gram-positive and Gram-negative bacteria.

TABLE 1
ANTIMICROBIAL ACTIVITY OF PHENOTHIAZIN-2(11H)-ONE DERIVATIVES 8a-f and 9a-f: MIC (µg/mL)

Compd	R (phenolic substituent)	*S. aureus*	*B. subtilis*	*E. coli*	*K. pneumoniae*
8a	m-Fluoro	25	100	100	50
8b	m-Bromo	100	50	100	50
8c	m-Chloro	100	50	50	50
8d	m-Nitro	50	50	50	**6.25**
8e	p-Methoxy	50	25	12.5	100
8f	p-Methyl	100	50	50	100
9a	m-Fluoro	**12.5**	50	100	50
9b	m-Bromo	25	100	50	100
9c	m-Chloro	100	25	25	25
9d	m-Nitro	100	**6.25**	50	25
9e	p-Methoxy	100	100	50	100
9f	p-Methyl	100	100	100	50
Chloramphenicol (standard)		25	50	25	25

Note: MIC values are presented in µg/mL. All tests were performed in duplicate; variation was within ±1 dilution. For K. pneumoniae, chloramphenicol MIC was determined as 25 µg/mL.

III. RESULTS AND DISCUSSION

Novel synthesized heterocyclic 8-(3-chloro-2-(2-hydroxy-3-nitrophenyl)-4-oxoazetidin-1-yl)-4-methylpyrano[2,3-b]phenothiazin-2(11H)-one and 8-(4-(2-(3-bromo-2-hydroxyphenyl)-3-chloro-4-oxoazetidin-1-yl)phenyl)-4-methylpyrano[2,3-b]phenothiazin-2(11H)-one derivatives (twelve derivatives, 8a-f and 9a-f) were checked for their antimicrobial activity against Gram-positive bacteria *B. subtilis*, *S. aureus* and Gram-negative bacteria *E. coli*, *K. pneumoniae*.

When the synthesized derivatives were evaluated against ***S. aureus***, compound **9a** (R = m-fluoro) showed excellent activity with an MIC value of 12.5 µg/mL, and compound **9b** (R = m-bromo) showed good activity with an MIC value of 25 µg/mL.

Against ***B. subtilis***, compound **9d** (R = m-nitro) displayed superior activity with an MIC value of **6.25 µg/mL**. Compounds **8e** (R = p-methoxy) and **9c** (R = m-chloro) exhibited MIC values of 25 µg/mL. The remaining compounds reflected only satisfactory activity.

Against ***E. coli***, compound **8e** (R = p-methoxy) displayed an MIC value of 12.5 µg/mL, and compound **9c** (R = m-chloro) exhibited an MIC value of 25 µg/mL. Ten compounds against *E. coli* showed good to moderate activity.

Against ***K. pneumoniae***, compound **8d** (R = m-nitro) was found to be the most lethal, achieving an MIC value of **6.25 µg/mL** with superior quality. Compounds **9c** (R = m-chloro) and **9d** (R = m-nitro) showed MIC values of 25 µg/mL. The remaining nine derivatives exhibited moderate activity against the *K. pneumoniae* strain.

From this microbial result analysis, **meta-positioned electronegative groups** (especially nitro, fluoro, and chloro) were responsible for achieving excellent MIC values.

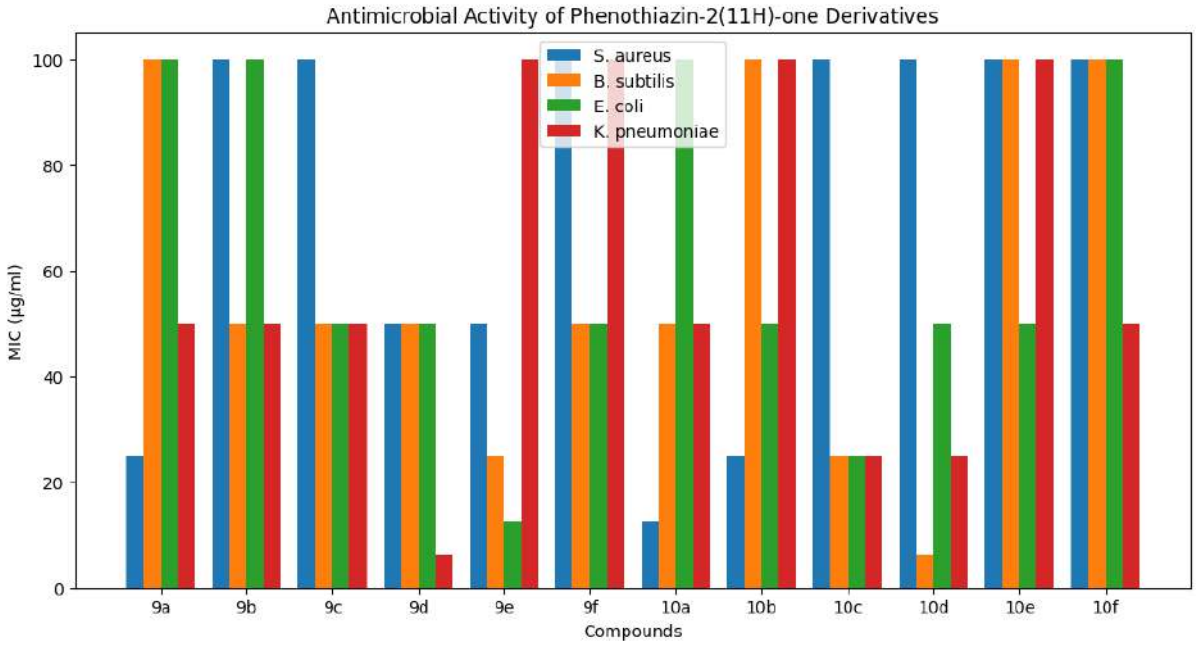

FIGURE 1: Showing antimicrobial activity of Phenothiazine-2(11H)-one derivatives

IV. CONCLUSION

The current study demonstrated that the synthesized novel heterocyclic phenothiazin-2(11H)-one derivatives possessed significant antimicrobial activity against both Gram-positive and Gram-negative bacterial strains. The biological evaluation revealed that the antimicrobial activity was strongly influenced by the nature and position of substituents present on the phenolic ring. Among all the tested compounds, **nitro-substituted derivatives** displayed excellent antibacterial activity. Compound **8d** showed excellent activity against *K. pneumoniae* with an MIC value of 6.25 µg/mL, while compound **9d** displayed remarkable inhibition against *B. subtilis* with the same MIC value. Methoxy-substituted derivative **8e** showed appreciable activity against *E. coli*, whereas methyl-substituted compounds exhibited comparatively lower activity. Overall, the synthesized compounds showed comparable activity and, in some cases, superior activity to the

standard drug chloramphenicol against specific bacterial strains. It is suggested that phenothiazin-2(11H)-one derivatives represent promising scaffolds for the development of new antimicrobial agents.

ACKNOWLEDGEMENT

We are thankful to the Faculty of Chemical Sciences, Shri Ramswaroop Memorial University, Barabanki for providing laboratory facilities. The authors also want to acknowledge Babasaheb Bhimrao Ambedkar Central University, Lucknow for providing instrumentation for biological activity.

CONFLICT OF INTEREST

The authors declare no conflict of interest.

REFERENCES

[1] Sandhu S, Bansal Y, Silakari O, Bansal G. Coumarin hybrids as novel therapeutic agents. Bioorg Med Chem. 2014;22:3806.

[2] Godge RK, Nalawade AK, Kolhe PV. Exploring the antifungal potential of 1, 2, 4-triazole derivatives: a comprehensive study on design and synthesis, Eur J Chem. 2023;4:4.

[3] Amaral L, Viveiros M, Molnar J, Kristiansen JE. Haloperidol as a known non-psychiatric drug with a potential for the management of multidrug-resistant tuberculosis. Expert Opin Drug Metab Toxicol. 2008;4:1337.

[4] Malmakova AE, Jones AM. Synthetic Routes and Bioactivity Profiles of the Phenothiazine Privileged Scaffold. Organics. 2025;6:46.

[5] Gershon S, Sakalis G, Bowers PA. Mesoridazine—a pharmacodynamic and pharmacokinetic profile. J Clin Psychiatry. 1981;42:463.

[6] Kalkanidis M, Klonis N, Tilley L, Deady LW. Novel phenothiazine antimalarials: synthesis, antimalarial activity, and inhibition of the formation of β-hematin. Biochem Pharmacol. 2002;63:833.

[7] Kaatz GW, Moudgal VV, Seo SM, Kristiansen JE. Kaatz, Glenn W., et al. "Phenothiazines and thioxanthenes inhibit multidrug efflux pump activity in Staphylococcus aureus. Antimicrob Agents Chemother. 2003;47:719.

[8] Amaral L, Viveiros M, Kristiansen JE. Amaral, Leonard, Miguel Viveiros, and Jette Elisabeth Kristiansen. "Phenothiazines: potential alternatives for the management of antibiotic resistant infections of tuberculosis and malaria in developing countries. Trop Med Int Health. 2001;6:1016.

[9] Al Zahrani NA, El-Shishtawy RM, Elaasser MM, Asiri AM. Synthesis of Novel Chalcone-Based Phenothiazine Derivatives as Antioxidant and Anticancer Agents. Molecules. 2020;25:4566.

[10] Sun-Waterhouse D, Chen J, Chuah C, Wibisono R, Melton LD, Laing WA, Ferguson LR, Skinner M. Kiwifruit-based polyphenols and related antioxidants for functional foods: Kiwifruit extract-enhanced gluten-free bread. Int J Food Sci Nutr. 2009;60:251.

[11] Gwaram NS, Ali HM, Abdulla MA, Buckle MJC, Sukumaran SD, Chung LY, Othman R, Alhadi AA, Yehye WA, Hadi AHA. Synthesis, Characterization, X-ray Crystallography, Acetyl Cholinesterase Inhibition and Antioxidant Activities of Some Novel Ketone Derivatives of Gallic Hydrazide-Derived Schiff Bases. Molecules. 2012;17:2408.

[12] Gao S, Hu M. Bioavailability challenges associated with development of anti-cancer phenolics. Mini Rev Med Chem. 2010;10:550-567.

[13] Teixeira J, Silva T, Benfeito S, Gaspar A, Garrido J, Borges F. Teixeira, José, et al. "Exploring nature profits: Development of novel and potent lipophilic antioxidants based on galloyl–cinnamic hybrids. Eur J Med Chem. 2013;62:289.

[14] Liu N, Jin Z, Zhang J, Jin J. Antitumor evaluation of novel phenothiazine derivatives that inhibit migration and tubulin polymerization against gastric cancer MGC-803 cells. Invest New Drugs. 2019;37:188.

[15] Gao Y, Sun TY, Bai WF, Bai CG. Design, synthesis and evaluation of novel phenothiazine derivatives as inhibitors of breast cancer stem cells. Eur J Med Chem. 2019;183:111692.

[16] Luan Y, Liu J, Gao J, Wang J. The design and synthesis of novel phenothiazine derivatives as potential cytotoxic agents. Lett Drug Des Discov. 2020;17:57.

[17] Tlhapi D, Ramaite ID, Anokwuru CP, Van Ree T, Hoppe HC. In Vitro Studies on Antioxidant and Anti-Parasitic Activities of Compounds Isolated from *Rauvolfia caffra* Sond. Molecules. 2020;25:3781.

[18] Abramovič H, Grobin B, Ulrih NP, Cigić B. Relevance and Standardization of In vitro Antioxidant Assays: ABTS, DPPH, and Folin–Ciocalteu. J Chem. 2018;2018:1.

[19] Pai Mangalore R, Peel TN, Udy AA, Peleg AY. The clinical application of beta-lactam antibiotic therapeutic drug monitoring in the critical care setting. J Antimicrob Chemother. 2023;78:2395.

[20] Wi YM, Choi JY, Lee DE, et al. Antimicrobial activity of cephamycins and β-lactam/β-lactamase inhibitors against ESBL-producing Escherichia coli and Klebsiella pneumoniae under standard and high bacterial inocula. Sci Rep. 2025;15:9785.

[21] Neu HC. **Contribution of beta-lactamase to bacterial resistance and mechanisms to inhibit beta-lactamases.** Am J Med. 1985;79:2.

[22] Tooke CL, Hinchliffe P, Bragginton EC, et al. β-Lactamases and β-Lactamase Inhibitors in the 21st Century. J Mol Biol. 2019;431:3472.

[23] Frère JM, Page MGP. Penicillin-binding proteins: evergreen drug targets. Curr Opin Pharmacol. 2014;18:112.

[24] Pandey N, Cascella M. Beta-lactam antibiotics. StatPearls. 2023.

[25] Bush K. Past and present perspectives on β-lactamases. Antimicrob Agents Chemother. 2018;62.

[26] Livermore DM. beta-Lactamases in laboratory and clinical resistance. Clin Microbiol Rev. 1995;8:557.

[27] Karaiskos I, Galani I, Daikos GL, Giamarellou H. Breaking Through Resistance: A Comparative Review of New Beta-Lactamase Inhibitors (Avibactam, Vaborbactam, Relebactam) Against Multidrug-Resistant Superbugs. Antibiotics. 2025;14:528.

[28] Tayeb SM, Alharbi JA, Alattas BB, Alotaibi DM, Althibaiti NM, Alharbi JF et al. Promising Future of Novel Beta-Lactam Antibiotics Against Bacterial Resistance. Drug Des Devel Ther 2025;19:9185–9197.

[29] Srivastava K, Prakash R, Singh RB, Srivastava A, Vishnoi RK. Synthesis, characterization and antibacterial evaluation of novel β-lactam and thiazolidin-4-one derivatives having thiadiazinyl ring. Bull Pharm Sci Assiut Univ. 2023;46(1):203-216.

[30] Drăgan M, Stan CD, Iacob AT, Dragostin OM, Boancă M, Lupușoru CE, Zamfir CL, Profire L. Biological evaluation of azetidine-2-one derivatives of ferulic acid as promising anti-inflammatoryagents. Processes. 2020;8(11):1-19.

[31] Drawz SM, Bonomo R. Three decades of b-lactamase inhibitors. Clin Microbiol Rev. 2010;23(1):160-201.

[32] Fedorchenko TG, Lipunova GN, Shchepochkin AV, Tsmokalyuk AN, Slepukhin PA, Chupakhin ON. Synthesis and properties of 1,3-diphenyl-5-(benzothiazol-2-yl)-6-R-verdazyls. Mendeleev Commun. 2018;28(3):297-299.

[33] Mishra CB, Shalini S, Gusain S, Prakash A, Kumari J, Kumari S, Yadav AK, Lynn AM, Tiwari M. Development of novel N-(6-methanesulfonyl-benzothiazol-2-yl)-3-(4-substituted-piperazin-1-yl)-propionamides with cholinesterase inhibition, anti-β-amyloid aggregation, neuroprotection and cognition enhancing properties for the therapy of Alzheimer's disease. RSC Adv. 2020;10(30):17602-17619.

[34] Pang B, Wang M, Liu W. Cyclization of polyketides and non-ribosomal peptides on and off their assembly lines. Nat Prod Rep. 2016;33(2):162-173.

[35] Agarwal N. Synthetic and therapeutic potential of 4-thiazolidinone and its analogs. Curr Chem Lett. 2021:119-138.

[36] Mishra I, Mishra R, Mujwar S, Chandra P, Sachan N. A retrospect on antimicrobial potential of thiazole scaffold. J Heterocyclic Chem. 2020;57:2304-2329.

[37] Vaidya A, Pathak D, Shah K. 1,3,4-oxadiazole and its derivatives, A review on recent progress in anticancer activities. Chem Biol Drug Des. 2021;97:572-591.

[38] Singh PP, Bansal S, Rawat K, Pullabhotla VSR. Synthesis of novel 1,4-bis-isoxazol/pyrazole and phenylpyrazole scaffolds by efficient green protocol and evaluation of biological properties thereof. Res J Chem Environ. 2021;25(5):48-61.

IJOER
ENGINEERING JOURNAL

International Journal of Engineering Research and Science

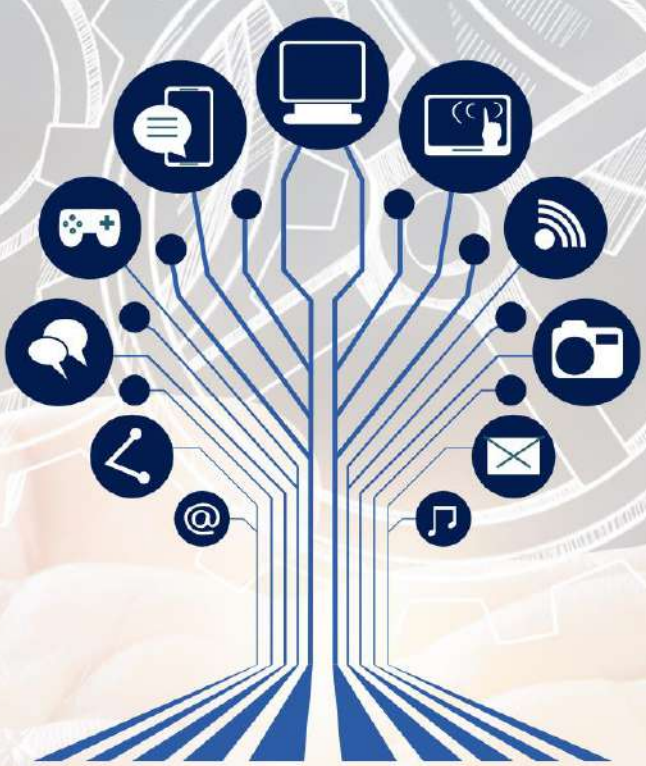

Published by

AD Publications

Contact us +91-7665235235 www.ijoer.com info@ijoer.com